GRAVITY WAVES FROM VORTEX DIPOLES AND JETS

A Dissertation

by

SHUGUANG WANG

Submitted to the Office of Graduate Studies of
Texas A&M University
in partial fulfillment of the requirements for the degree of

DOCTOR OF PHILOSOPHY

August 2008

Major Subject: Atmospheric Sciences

GRAVITY WAVES FROM VORTEX DIPOLES AND JETS

A Dissertation

by

SHUGUANG WANG

Submitted to the Office of Graduate Studies of
Texas A&M University
in partial fulfillment of the requirements for the degree of

DOCTOR OF PHILOSOPHY

Approved by:

Chair of Committee,	Fuqing Zhang
Committee Members,	Chris Snyder
	Craig Epifanio
	Kenneth Bowman
	Jianxin Zhou
Head of Department,	Kenneth Bowman

August 2008

Major Subject: Atmospheric Sciences

ABSTRACT

Gravity Waves from Vortex Dipoles and Jets. (August 2008)

Shuguang Wang, B.S., Nanjing University;

M.S., Nanjing University; M.S., Texas A&M University

Chair of Advisory Committee: Dr. Fuqing Zhang

The dissertation first investigates gravity wave generation and propagation from jets within idealized vortex dipoles using a nonhydrostatic mesoscale model. Several initially balanced and localized jets induced by vortex dipoles are examined here. Within these dipoles, inertia-gravity waves with intrinsic frequencies 1-2 times the Coriolis parameter are simulated in the jet exit region. The ray tracing analysis reveals strong variation of wave characteristics along ray paths. The dependence of wave amplitude on the Rossby number is examined through experiments in which the two vortices are initially separated by a large distance but subsequently approach each other and form a vortex dipole with an associated amplifying localized jet. The amplitude of stationary gravity waves in the simulations with a 90-km grid spacing increases nearly linearly with the square of the Rossby number but significantly more rapidly when smaller grid spacing is used.

To further address the source mechanism of the gravity waves within the vortex dipole, a linear numerical framework is developed based on the framework proposed by Plougonven and Zhang (2007). Using the nonlinearly balanced fields as the basic state

and driven by three types of large scale forcing, the vorticity, divergence and thermodynamic forcing, this linear model is utilized to obtain linear wave responses. The wave packets in the linear responses compare reasonably well with the MM5 simulated gravity waves. It is suggested that the vorticity forcing is the leading contribution to both gravity waves in the jet exit region and the ascent/descent feature in the jet core.

This linear model is also adopted to study inertia-gravity waves in the vicinity of a baroclinic jet during the life cycle of an idealized baroclinic wave. It is found that the thermodynamic forcing and the vorticity forcing are equally important to the gravity waves in the low stratosphere, but the divergence forcing is again playing a lesser role. Two groups of wave packets are present in the linear responses; their sources appear to locate either near the surface front or near the middle/upper tropospheric jet.

DEDICATION

To my beloved wife Liang

and

to my newborn baby Rachel

ACKNOWLEDGEMENTS

First, I would like to thank my advisor, Dr. Fuqing Zhang, whose guidance helped me through this long PhD journey. His passion and perceptive insight tremendously benefited this doctoral research. Without his patience, encouragement and trust in me over these years, this dissertation would not exist, certainly not in its present form.

Next, I am grateful to my other committee members, Dr. Craig C. Epifanio, Dr. Chris Snyder, Dr. Kenneth Bowman and Dr. Jianxin Zhou, for their inspiring discussions and valuable suggestions. In particular, I deeply appreciate the discussions with Dr. Craig C. Epifanio and Dr. Chris Snyder. They were always willing to share their wisdom and expertise on this research subject. Special thanks also go to Dr. Riwal Plouvegon and Dr. Todd Lane for their comments on my research work. I thank Dr. Juan Fang for her helpful comments. I am also very grateful to the NOAA Earth System Research Laboratory for providing me a visitorship in July 2007, during which I had many helpful discussions with Dr. Steve Koch and Dr. Chungu Lu on my research projects.

I also want to thank our current and past group members, Yonghui Wen, Jason Sippel, Ellie Meng, Meng Zhang, Tingting Qian, Matthew Rigney, Naifang Bei, Altug Aksoy and Yonghui Lin, for creating such an enjoyable working environment. Thanks to Matthew Rigney and Jason Sippel for correcting grammar mistakes. I enjoyed interactions with the other students and postsdocs, Gang Hong, Zhibo Zhang, Caihong

Wen, Guohui Li, Salil Mahajan, and others. I am thankful for the help from the office staff in the Department of Atmospheric Sciences.

Finally and foremost, I am greatly indebted to my family for their understanding, patience and continuous support during this years.

This research was sponsored by the NSF grant ATM-0203238 and ATM-0618662.

TABLE OF CONTENTS

Page

LIST OF FIGURES

Page

Page

Page

Page

Page

Page

Page

LIST OF TABLES

Page

1. INTRODUCTION

Freely propagating gravity waves in the atmosphere began to receive attention since 1960 when Hines first interpreted irregular motions in middle atmosphere as gravity waves. Since then, atmospheric gravity wave signatures have been documented in numerous studies that are based on different types of observations such as barometers, rawinsondings, meteorological radars and space-based monitoring equipments. The dynamical significance of gravity waves is gradually appreciated. In short, gravity waves are able to interact with a wide range of phenomena at different scales, partly because they are ubiquitous in both space and time. For example, at turbulence scales (less than 1 km), gravity waves can promote mixing and clear air turbulence. At the convection scales, they play important roles in initiating and modulating convections. They can also carry significant energy into low stratosphere and middle atmosphere, thus influence climate at a large spatial and temporal scale.

Gravity waves can be generated by a variety of different sources in the real atmosphere. Known sources of gravity waves at low troposphere include topography, convection, front, wind shear, upper tropospheric jet, geostrophic adjustment and spontaneous generation (Fritts and Alexander 2003; Kim et al. 2003). Among this list, topography and convection have been the research subjects of numerous studies. On the other hand, upper tropospheric jets as gravity wave sources receive less attention and are less understood. Our current understanding of source mechanism of gravity waves from

---

This dissertation follows the style of *the Journal of the Atmospheric Sciences*.

atmospheric jets is rather limited.

Upper tropospheric jets often have very complicated structures and are mixed with many other processes in real atmosphere. For this reason, idealized models are generally preferred to be used as a basic tool to understand their temporal and spatial structures, as well as gravity waves from jets. This study follows this line and attempts to understand wave generation from idealized jets. Gravity waves in two types of idealized jets will be considered in this work: waves from a localized jet and a more realistic baroclinic jet. The first objective of this study is to obtain the physically reasonable wave solution from a localized jet within vortex dipoles, identify characteristics of inertia-gravity waves in the exit region of jet from the simulations, and study wave propagation in sheared environment of the localized jet. The second objective is to understand the wave source mechanism from a localized jet and a baroclinic jet by using a linear numerical model. It is suggested that this study will contribute to our understanding of the basic source mechanism and propagation effects of gravity waves near the tropospheric jet.

1.1 Linear theory of gravity waves, sources and impact

Gravity waves are special phenomena in stratified fluids under gravitational forces. According to "Glossary of Meteorology" published by American Meteorology Society, gravity wave is "a wave disturbance in which buoyancy (or reduced gravity) acts as the restoring force on parcels displaced from hydrostatic equilibrium". This definition neglects the rotational effects. As a matter of fact, atmospheric gravity waves can have a horizontal scale ranging from a few kilometers up to thousands of kilometers.

For long waves, the Coriolis force because of Earth's rotation can significantly alter wave characteristics; this type of gravity waves is "inertia-gravity waves". Atmospheric gravity waves have wave frequencies bounded by buoyancy frequency N ($\sim 10^{-2}\ s^{-1}$) and the Coriolis parameter f ($\sim 10^{-4}\ s^{-1}$). This gives a ratio $N/f \sim 100$. Because gravity wave frequencies can not be lower than the inertial frequency, gravity wave family is considered as high frequency modes. They are faster than low frequency synoptic eddies, which are dominate features of synoptic and large scale flow.

Because of the broad range of the ratio N/f, gravity waves can be divided into three ranges. In each range, some useful approximations can be made. At the high frequency limit where the intrinsic wave frequency is much larger than Coriolis parameter ($\omega_i >> f$), rotation can be neglected and compressible and nonhydrostatic effects have to be considered. Nonhydrostatic gravity waves are usually short living with a relatively a small wavelength. In some special situations, wave trapping, reflection, ducting may become important during the life span of these gravity waves. At the immediate range ($f << \omega_i << N$), hydrostatic approximation is valid since gravity waves have a large aspect ratio (its vertical wavelength divided by the horizontal wavelength). For gravity waves having frequencies close the low limit ($\omega_i >= f$), they generally can have longer horizontal wavelengths, travel long horizontal distance. Often they are observed near upper tropospheric jets and in the low stratosphere.

Like many other disciplines, the most established achievement in the gravity wave research is the linear theory of small amplitude waves. To date, several classic textbooks have discussed various aspects of this subject, e.g., Gossard (1976), Leblond

and Mysak (1978), Gill (1982), Andrews et al. (1987), Nappo (2002) and Holton (2004). The linear theory has been employed to explain many observational features by numerous investigators. As an example, polarization relation relating amplitude of different perturbations is used extensively to extract gravity wave signals from rawinsondings observations. On the other hand, departure from the linear theory has strong implications for general circulations. Probably the most important nonlinear process of gravity waves is wave dissipation and breaking occurring far away from wave sources (Lindzen 1981; Fritts 1984). The effects of wave breaking and dissipation are non-local. These processes can deposit wave momentum and energy into the mean flow at a far distance from their sources, and impact the momentum and energy of the large scale mean flow in the low stratosphere and middle atmosphere. Also, nonlinear dynamics such as wave dissipation may lead to energy injection to small scale and cause mixing. Wave breaking at low stratosphere may promote clear air turbulence, which is always a big concern to aviators. Nevertheless, there is still a lacking of physical understanding of the wave dissipation, gravity wave drag, and the source mechanisms. These are also current active research topics.

Although gravity waves are ubiquitous, it is generally believed that they are only occasionally weather significant, because synoptic flow is dominated by low frequency synoptic eddies, not by high frequency gravity waves. Nevertheless, gravity waves are important for NWP models that are used for weather forecast practice. Failure to realize the role of gravity waves may cause trouble to NWP models. This is one of main reasons that first NWP experiment in history (Richardson 1922; Lynch 2008) produce outlandish

results. On the contrary, the first promising NWP practice is based on the proper treatment of gravity waves (by filtering out high frequency waves). Although early NWP models tend to minimize gravity wave effects, it is now widely believed that gravity waves must be accurately represented in the current cloud-resolving NWP models. One reason is that many sources can generate gravity waves in the low atmosphere and these waves interact with other processes. Also, improper model numerics can generate spurious gravity waves. Despite being prone to produce gravity waves, NWP models are used extensively as a basic tool to study gravity waves and their sources in real atmosphere.

A variety of sources can generate gravity waves in the troposphere, e.g., air flow passing over topography, convection, jets, fronts (or more appropriately, frontogenesis), wind shear, geostrophic adjustment, nonlinear wave-wave interactions and spontaneous emission. Among these sources, topography is probably most extensively studied (e.g., Smith 2004) due to its apparent source mechanism and limited spatial extension. Convectively generated gravity waves also receive a great deal of attention, especially waves from deep tropical convections (Holton et al. 1995). Three source mechanisms for convectively generated gravity waves have been proposed: pure thermal forcing (Alexander et al. 1995), the mechanical oscillator (Fovell et al. 1992), and moving obstacle effects (Pfister et al. 1993). Another widely mentioned gravity wave source mechanism is geostrophic adjustment (Rossby 1937; Cahn 1945; Blumen 1972), which is a classic concept from the beginning of modern meteorology. Analytical models were used by some authors (Fritts and Luo 1992; Luo and Fritts 1993) to demonstrate wave

generation from geostrophic adjustment. Applications of this concept to wave generation in real atmosphere are arguably successful due to the fast-evolving nature of adjustment itself (e.g., O'Sullivan and Dunkerton 1995). Gravity waves from jets are related to adjustment processes but remain to be an unresolved issue (to be discussed later). Fronts, or frontogenesis processes, can also generate significant amount of gravity waves (Snyder 1993, Reeder and Griffins 1996; Griffins and Reeder 1996). Other gravity wave sources in the lower atmosphere include shear generation (Bühler et al. 1999), nonlinear wave-wave interactions (Vanneste 1995). More recently, people realized that gravity waves can arise spontaneously as a response to nonlinear forcing, in analogy to acoustic wave generation (Lighthill 1977). This mechanism is more relevant to fundamental concept of flow balance and of more interest to theoreticians (e.g. Ford 1994; Ford et al. 2000).

This doctoral research will focus on the understanding gravity waves from upper tropospheric jets, as will be discussed next.

1.2 Gravity waves and upper tropospheric jets

Mid-latitude baroclinic jets at the level of the tropopause are among the list of the most important synoptic features in synoptic meteorology. They are considered as a major component of mid-latitudes weather system. Their variations and impact on climate are also active research topics. Many studies based on either observations (e.g., Uccellini and Koch 1987; Koch and Dorian 1988; Schneider 1990; Ramamurthy et al. 1993; Sato 1994; Bossart et al. 1998; Koch and O'Handley 1998; Koppel et al. 2000; Plougonven and Teitelbaum 2003; Wu and Zhang 2004; Koch et al. 2005) or numerical

simulations (e.g., O'Sullivan and Dunkerton 1995) found that upper tropospheric baroclinic jets and jet-front systems favor gravity wave generation. These waves typically have a characteristic horizontal wavelength hundreds of kilometers and wave frequency near the inertial frequency. However, our understanding of the source mechanism of gravity waves from jets as well as their impact on general circulations is rather limited. They are less understood compared to some other wave source mechanisms such as topography and convections.

Several hypotheses appearing in the literature are possibly applicable to gravity waves from atmospheric jets. Uccellini and Koch (1987) ruled out possible wave source mechanism of shear instabilities and suggested that geostrophic adjustment is most likely responsible for wave generation near jets. Geostrophic adjustment was once believed to be the most relevant wave generation mechanisms (Kaplan and Paine 1977; Van Tuyl and Young 1982; Zhang et al. 2001). The basic idea is that imbalance between wind and mass fields radiates gravity waves (Rossby 1945; Cahn 1945; Fritts and Luo 1993). The existence of a balanced state is of central importance to this idea. Imbalance is defined as a departure from the balanced state. Nevertheless, flow balance is not uniquely defined in general, and different definition has been adopted in different studies. Because flow balance is essentially a vague concept, various diagnostic tools of flow imbalance have been proposed (Zhang et al. 2000). Among these tools, the residual of the nonlinear balance equation is frequently used to examine flow imbalance near upper level jets where nonlinear advection is significant. Zhang (2004) illustrated that ΔNBE can be used as precursor to gravity wave generation in the jet exit region, and suggested that

generalized balance adjustment, as a generalization of geostrophic adjustment, is best suited to explain the wave generation; this hypothesis was further generalized by Plougonven and Zhang (2007) through scale analysis of primitive equations. Different from these balance adjustment ideas, several other studies (Snyder et al. 1993; Griffiths and Reeder 1996; Snyder et al. 2007) indicated that gravity waves are spontaneous response to large scale balanced flow. Another related source mechanism is spontaneous adjustment emission proposed by Ford (Ford 1994 and Ford et al. 2000) in the rotating shallow water system.

To this end, it is helpful to clarify the above concepts related to wave generation hypothesis: geostrophic adjustment, generalized balance adjustment, spontaneous response and spontaneous adjustment emission. Classical Rossby type geostrophic adjustment (Rossby 1937, Blumen 1972) is an initial value problem and depends on initial conditions due to initial flow imbalance. Geostrophic adjustment usually occurs on a time scale of a few inertial periods. Generalized balance adjustment (Zhang 2004) suggests that continuous flow imbalance is responsible for wave generation. Flow imbalance specifically means the residual of the nonlinear balance equation (ΔNBE). The key of this argument is the existence of flow imbalance preceding gravity wave event. It should be noted that flow imbalance does not necessarily come from initial flow imbalance. Hence balance adjustment does not limit to a time scale of several inertial periods. Plougonven and Zhang (2007) generalized the argument of wave forcing by the NBE residual and suggested that residual terms, not only from the divergence equation, but also from the vorticity and potential temperature equations, may all be important.

Thus they provide a complete picture about wave generation from large scale flow. Their results are used a guide line for this study.

The phrase of 'spontaneous emission' is used in literature to emphasize that it sharply differs from geostrophic adjustment in that wave emission is not due to imbalance in the initial condition, as in the geostrophic adjustment problem. Spontaneous response in Snyder et al. (1993, 2007) suggests that the residual tendency is responsible for wave generation, if the tendency forcing can effectively projects to scales on which inertia-gravity waves may be generated. The residual tendency refers to 'the difference between the tendencies predicted by the balanced solution and those obtained upon substitution of the balanced fields into the full primitive equations' (Snyder et al. 2007). Both 'generalized balance adjustment' and 'spontaneous response' are based on definition of flow balance. Nevertheless, the problem of flow separation is left open. Spontaneous adjustment emission in Ford (1994) and Ford et al. (2000) concluded that nonlinear advection in shallow water equation can generate gravity waves at scales much large than sources. This theory differs from previous two hypotheses in that it is well established for the shallow water equations, but its generalization to 3D stratified fluid is not fulfilled. Ford et al. (2000) also offered an explicit definition of flow balance (termed 'slow manifold' in Ford et al. 2000) based on the potential vorticity inversion. They suggested that such a slow manifold does not exist and wave emission is asymptotically small; rather, a 'quasi slow manifold' is suggested to be more appropriate. Spontaneous adjustment emission originates from ideas of the Lighthill theory on acoustic wave emission (Lighthill 1952); hence, it is often referred as 'Lighthill emission'. In the

numerical studies of waves from vortical flow (Pallàs-Sanz and Viúdez 2008; Viúdez 2008; Viúdez 2007; Viúdez 2008), Viúdez classified gravity waves within the vortex dipole as a result of spontaneous adjustment emission, following the terminology in Ford et al. (2000).

The linear model formulation of wave forcing in Plougonven and Zhang (2007, hereinafter PZ07) in a stratified flow is a direct analog to the spontaneous adjustment emission in the rotating shallow water (Ford 1994 and Ford et al. 2000). Ford (1994) recast the governing equations into a single equation with the left hand side consisting of a linear wave operator, and right hand side consisting derived tendency terms (in the form of second order spatial derivatives of quadratic product). Except in simple background wind, the wave operator of PZ07 can hardly be written in a single equation of one prognostic variable on which a rigorous mathematical analysis can be carried out as for the wave operator in Ford (1994).

Despite all hypotheses discussed above, direct and convincing evidence of gravity wave generation from jets is still limited in the literature. First, studies based on observations can not distinguish waves from jet and other sources such as convections. Second, numerical studies also have such limitation. Only a few modeling studies connect wave generation to the baroclinic jet-front system (O'Sullivan and Dunkerton 1995; Zhang 2004; Wang and Zhang 2007; Plougonven and Snyder 2007). The major difficulties come from the complex background flow of fast evolving baroclinic jets, which are coupled with other synoptic features such as surface fronts. In many cases (e.g. Wu and Zhang 2004), identification of the exact wave source is highly uncertain

since other potential sources of wave forcing such as surface fronts and convections are also present in the real atmosphere and even idealized flow. In order to focus on essential dynamics of jet-related wave generation, different idealized settings of jet has been adopted. As a further simplification of baroclinic jets, Snyder et al. (2007) and Viúdez (2008) both created localized jets that is arising naturally from vortex dipoles. They identify unambiguously long-lived inertia-gravity waves emitted from vortex dipoles. By analyzing the generalized omega equation, Viúdez (2007) proposed that these waves originate from the differential vertical vorticity. Nevertheless, a complete wave generation scenario is still lacking. This study continues to investigate these two settings of idealized jets: localized jets within the vortex dipole and baroclinic jets during the life cycle of baroclinic waves. A new numerical framework based on the argument proposed by Plougonven and Zhang (2007) is developed in this dissertation to study wave generation.

In addition to wave source mechanisms, propagation effects are also important. Although this is not a new issue, it is recently suggested that wave propagation can strongly modify wave characteristics. Plougonven and Snyder (2005) argued that some important wave parameters such as wavelengths can be determined by wind environment due to wave refraction. Lin and Zhang (2008) also demonstrated variations of wave parameters in a baroclinic jet. It is thus necessary to include both effects in the study of gravity waves. This propagation effects will also be discussed in this study as a complementary to earlier studies.

1.3 Methodology

Mesoscale NWP models are usually adopted as a basic tool to understand gravity waves generated by topography (e.g., Smith 2004; Doyle et al. 2005), convection (e.g., Lane and Clark 2002; Song et al. 2003; Pandya and Alexander 1999), and in very complex flow configuration (Power and Reader 1993; Kaplan et al. 1997; Zhang and Koch 2000; Koch et al. 2001; Zhang et al. 2000, 2001, 2003 and 2004; Wu and Zhang 2004; Guest et al. 2000; Zülicke and Peters 2006; Koch et al. 2005). The main body of this work is to numerically solve the relevant problems using a mesoscale model and a linear numerical model combined with other numerical techniques.

a. A mesoscale numerical model and its balance initialization

The main tool to obtain gravity wave solutions in three dimensional stratified flow is a mesoscale NWP model, the NCAR/PSU non-hydrostatic MM5 version 3 (Dudhia, 1993). The model is initialized through the Ertel potential vorticity (EPV) inversion procedure (Davis and Emanuel, 1991).

b. A four dimensional ray tracing model

To examine the propagation of jet-exit region gravity waves from the dipole flow, the numerical ray tracing model GRGRAT (Marks and Eckermann 1995; Eckermann and Marks 1997) will be applied to the simulations of gravity waves within the vortex dipole. Our current ray tracing will not include wave amplitude/energy calculations, since the ray tube method has not been implemented.

c. A linear model

Gravity waves simulated by the mesoscale model obey linear dynamics. A nonhydrostatic and compressible linear model is thus developed to study wave responses to relevant forcing following an initial value approach. The numerical technique for stratified 3D flow is well established (see Durran 1999).

1.4 Objectives

This doctoral research seeks to explore wave generation mechanisms in two types of idealized flow. One type flow is highly simplified localized jet within vortex dipoles. Tasks include: (1) to obtain gravity wave solution in a mesoscale numerical model and (2) to understand the wave source mechanism using a linear model. The other type flow is the baroclinic jet during life cycle of a baroclinic wave. The baroclinic jet is more realistic in terms of its spatial and temporal structure. Because the MM5 solutions have been well established and published, the task here is to perform wave forcing diagnosis and study wave response to the diagnosed forcing. Specific goals include:

(1) Set up initially balanced vortex dipoles, including initially balanced surface vortex dipole, a dipole maximizing in the mid-level of the atmosphere. Configure the MM5 model, perform long term (up to 40 days) simulations of these vortex dipoles and obtain physically reasonable gravity wave solutions. Analyze characteristics of simulated gravity waves within vortex dipoles. Perform wave tracing analysis to investigate wave refraction effects. Study wave amplitude dependence on the strength of the localized jet.

(2) Build up a linear model that can be used to investigate the wave response to specified forcing. Verify this linear model. Study wave response to specified forcing in a vortex dipole flow. Perform sensitivity analysis of wave response to prescribed forcing. Perform wave source diagnosis and obtain steady state solution of the linear model that is driven by the diagnosed wave sources.

(3) Investigate the source mechanism of gravity waves in the exit region of a baroclinic jet (Zhang 2004). Perform wave source diagnosis and obtain responses from a linear model.

Overall, this work attempts to develop a general approach in order to investigate gravity wave source mechanism. The effectiveness of this approach will demonstrated for waves in two types of highly idealized flow. The organization naturally follows these goals listed above.

Following the introduction, Section 2 discusses numerical simulations of gravity waves in the vicinity of both quasi-stationary and slowly strengthening localized jets within vortex dipoles. Ray tracing analysis is also performed. Section 3 documents a linear model and its verification. Steady state solutions to prescribed forcing are obtained using the linear model. Section 4 presents results of wave source diagnosis and linear model solutions. Section 5 discusses results for gravity waves in the vicinity of a baroclinic jet. Section 6 concludes this study.

2. GENERATION AND PROPAGATION OF INERTIA-GRAVITY WAVES FROM VORTEX DIPOLES AND JETS

2.1 Introduction

Gravity waves propagating vertically from the lower atmosphere are widely recognized to play important roles in a variety of atmospheric phenomena. Known sources of these gravity waves include mountains, moist convection, fronts, upper level jets, geostrophic adjustment and spontaneous generation (Fritts and Alexander 2003 and refs. therein). Among these, jets are often responsible for generating low frequency inertia-gravity waves with characteristic horizontal wavelengths of several hundred kilometers as suggested by many observational studies (e.g., Uccellini and Koch 1987; Sato 1994; Wu and Zhang 2004). Numerous mechanisms for gravity-wave generation by jets have been proposed (e.g., Zhang 2004), but such generation remains poorly understood compared to other wave sources such as topography and moist convection. Diagnosing jet-related generation of inertia-gravity waves in observed cases is also often difficult, as the jet typically co-exists with other potential sources such as surface fronts and moist convection (e.g., Zhang et al. 2001; Plougonven and Teitelbaum 2003).

In order to focus on essential dynamics of jet-related wave generation, different idealized settings of jets have been proposed in several studies. One approach to simplify the wave generation scenario is to simulate a jet in the context of developing baroclinic waves (O'Sullivan and Dunkerton 1995; Zhang 2004; Wang and Zhang 2007; Plougonven and Snyder 2007). In this approach, the spontaneous generation of gravity

waves associated with the jet within the idealized baroclinic waves occurs in a complex, time dependent flow, while the synoptic scale background evolves relatively quickly. Snyder et al. (2007, hereinafter SMPZ07) took another approach by creating a localized jet that arises naturally within surface-trapped vortex dipoles. They unambiguously identified long-lived inertia-gravity waves emitted by the dipole. The dipole flow supporting the wave generation evolves very slowly in time (up to many inertial periods), and is nearly steady in an appropriate frame of reference. Viúdez (2008) also simulated inertia-gravity waves from vortex dipoles, with findings very similar to SMPZ07. He considered vortex dipoles associated with potential vorticity anomalies in the interior the flow rather than confined to a horizontal boundary. Despite its simplified setting, the continuous generation of inertia-gravity waves from vortex dipoles is qualitatively similar to those in baroclinic waves in the sense that they appear in the jet exit region and propagate in phase with the jet. These slowly evolving vortex dipoles provide a good laboratory to better understand fundamental mechanisms of gravity wave generation by jets.

As an extension of SMPZ07 and Viúdez (2008), this section further explores gravity wave generation in different localized jets settings, including a surface vortex dipole and a dipole maximizing in the mid-level of the atmosphere. Broadly speaking, the simulated waves from the surface vortex dipole are similar to those simulated in SMPZ07 and the waves in mid-level dipole are similar to those simulated in Viúdez (2008). But the current study will have the advantage of directly comparing waves from the surface and mid-level dipoles in a nonhydrostatic mesoscale model. The dependence

of the wave amplitude on jet strength is further estimated using slowly amplifying jets that are simulated in distant-dipole experiments, in which a cyclone and an anticyclone are initially separated by a large distance but subsequently approach slowly towards each other and form a vortex dipole. We will stress both similarities and differences of gravity waves in these different types of dipoles and further discuss implications for wave source mechanisms.

This section will also investigate the propagation of gravity waves in the sheared flow in the exit region of localized jets. Past studies show that wave characteristics may change significantly along the propagation path in an inhomogeneous media (Staquet and Sommeria 2002, Plougonven and Snyder 2005, Lin and Zhang 2008). In a simulation of a developing baroclinic wave, Plougonven and Snyder (2005) demonstrated that wave refraction from strong horizontal deformation and vertical wind shear in the jet exit region could determine the wave characteristics through the wave-capture mechanism (Bühler and McIntyre 2005). SMPZ07, however, argued that packets of emitted waves in their simulations propagated too quickly through the jet-exit region for wave capture to occur. Our study will further examine the possibility of wave capture by using a four-dimensional (4-D) ray-tracing model that incorporates spatial and temporal variations of the background flow.

The rest of this section is organized into 5 parts. We first describe experimental design. Wave generation from different types of dipoles is discussed next. Wave propagation is examined by using ray tracing analysis in the next step. Dependence of

wave amplitude on the Rossby number is further explored through the distant-dipole experiments.

2.2 Experimental design

This study employs a nonhyhrostatic, compressive mesoscale model (MM5 version 3; Dudhia 1993) to perform all numerical experiments. Ertel potential vorticity (EPV) inversion (Davis and Emanuel 1991) is adopted to create initial conditions for the primitive equation model because it can minimize the adjustment processes due to flow imbalance. The nonlinear balance equation (Charney 1952) is used as the balance constraint for EPV inversion and it is believed to be accurate even in a flow regime of a moderate Rossby number (Raymond 1992). This EPV inversion procedure is similar to the first order direct potential vorticity inversion in rotating shallow water system discussed by McIntyre and Norton (2000). The EPV inversion solves stream function Ψ and geopotential Φ simultaneously for a given EPV distribution Q. Here, the total wind is approximated by $V = -\vec{k} \times \nabla\Psi + \nabla\Phi$. The governing equations for the three dimensional Ertel PV inversion are the nonlinear balanced equation and the definition of EPV,

$$\begin{aligned} \nabla^2\Phi &= \nabla(f\nabla\Psi) + 2(\Psi_{xx}\Psi_{yy} - \Psi_{xy}^2) \\ Q &= (f + \nabla^2\Psi)\Phi_{\pi\pi} - \Psi_{x\pi}\Phi_{x\pi} - \Psi_{y\pi}\Phi_{y\pi} \end{aligned}, \qquad (2.1)$$

where Exner function π is taken as the vertical coordinate. Solutions to the EPV inversion are guaranteed if the elliptical condition is satisfied. This condition is equivalent to requiring EPV positive definite everywhere. The boundary conditions for the EPV equations are Neumann type since usually potential temperature at boundary is

given. Flow at lateral boundaries is required to have zero normal velocities. Since this EPV inversion is solved on the pressure surface, in practice, the balanced fields are linear interpolated to the height-based MM5 coordinate. Configurations of the initial EPV anomalies along with other important numerical aspects are given below.

a. Vortex dipole initialization

For all experiments, we first specify the reference state with constant static stability $N^2 = 2 \times 10^{-4} s^{-2}$ (detailed in the appendix I). All thermodynamic variables, including the reference state EPV in a reduced form $Q(z) = -gf\frac{\partial \theta}{\partial p} = -\frac{fN^2}{g} \cdot \frac{\theta}{\rho}$, are thus determined using the reference static stability, where g, f, θ, ρ, and p are gravity, the Coriolis parameter, potential temperature, density, and pressure, respectively. The reference θ increases exponentially with height: $\theta = \theta_o \exp(N^2 z/g)$.

To produce a surface vortex dipole (SFJET) similar to SMPZ07, we prescribe a pair of oppositely signed surface temperature anomalies of the same magnitude using a truncated cosine function. The θ anomalies smoothly drop to zero at a circle of 1800 km. The positive (negative) boundary temperature anomalies in Fig. 2.1a are equivalent to interior positive (negative) PV anomalies that are associated with cyclonic (anticyclonic) circulations (Hoskins et al. 1985). An initially balanced and localized jet is subsequently obtained through EPV inversion of these dipolar surface temperature anomalies. Figure 2.1a shows that this localized jet has a maximum wind of 25 m/s. The surface relative vorticity is also nearly symmetric with a maximum 0.55 f (-0.6 f) in the cyclone (anticyclone) center. A vertical cross section reveals further asymmetry; the

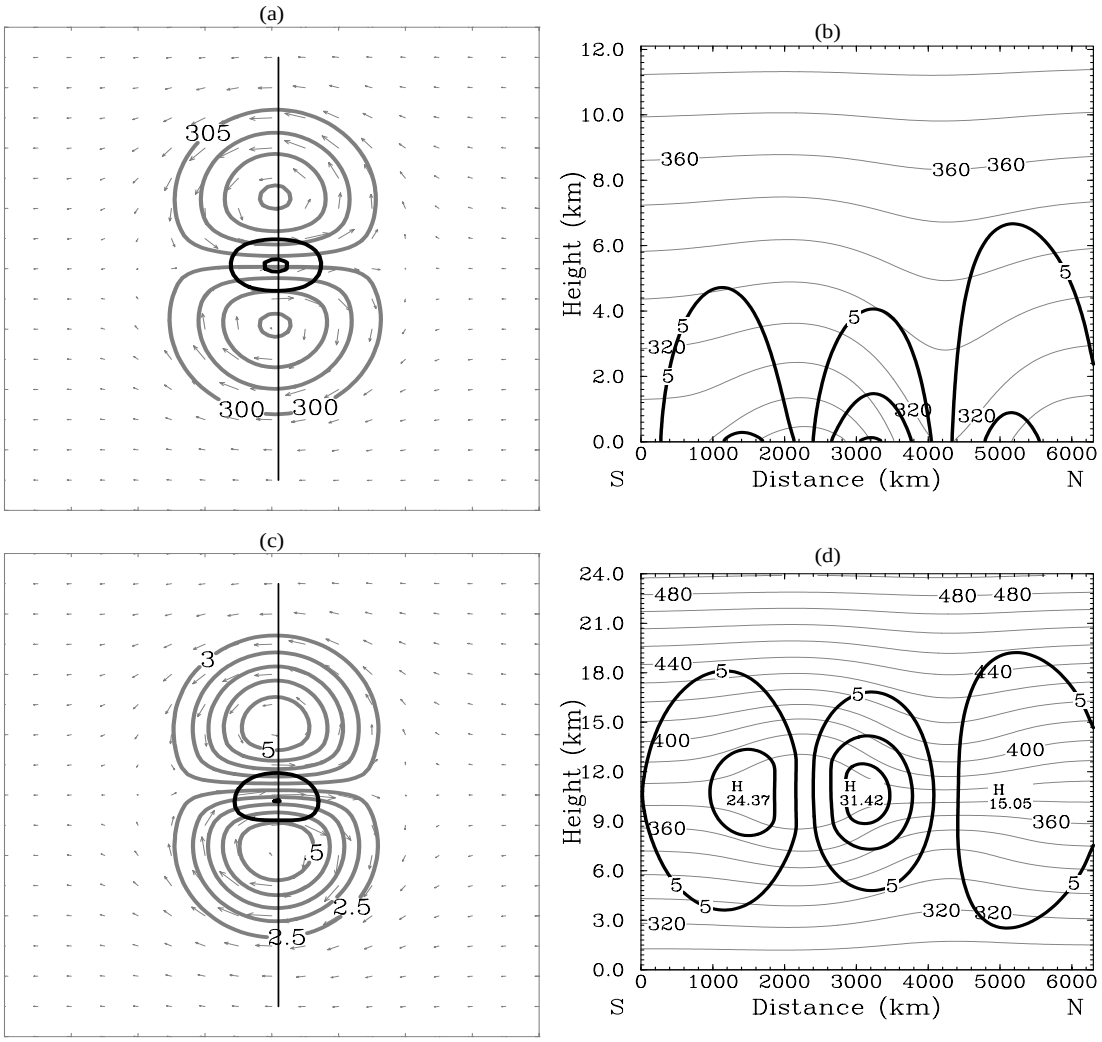

Figure 2.1. Initial conditions for MDJET and SFJET. Panels (a) and (c) are horizontal views of wind vectors and wind speed (contour interval (ci) is 5 m/s with values less than 20 m/s omitted), together with either potential vorticity (ci =0.5 PVU) at 12 km in (a) or potential temperature (ci = 5 K) in (c). Panels (b) and (d) are wind speed (ci=5 m/s), potential temperature (ci = 10 K) plotted along the vertical cross sections indicated by black lines in the corresponding left panels. The distance between ticks in top panels are 900 km. Note only a small subset of the MM5 90-km domain is shown on the horizontal planes.

horizontal winds in the surface cyclone extend to higher levels than those in the anticyclone (Fig. 2.1b). This asymmetry is due in part to the larger penetration depth, *H,* of EPV anomalies in the cyclone where static stability (*N*) is reduced, since *H* and *N* are related by $H = fL/N$, where *L* is the horizontal scale.

Experiment "MDJET" initializes a mid-level vortex dipole with a pair of oppositely signed EPV perturbations of the same magnitude in the mid-troposphere (details in Appendix II). Figures 2.1 c and d show the initial horizontal and vertical structures of MDJET. The wind speed in the anticyclonic (cyclonic) flank is 24.4 (15.1) m/s (Fig. 2.1c). For reasons discussed later, the jet core shifts toward the anticyclone. The maximum wind speed in the jet core reaches 31.5 m/s, rendering an Eulerian Rossby number ($Ro = U/fL$) of ~ 0.18 given the horizontal scale *L* of 1800 km (distance between the two vortex cores). The Froude number ($Fr = U/NH$) is ~ 0.21 given the vertical scale $L \sim 10$ km. In the surface dipole, the inverted horizontal winds above (and below) the EPV anomalies penetrate higher in the cyclone than the anticyclone. The maximum vorticity reaches $0.45 f$ ($-0.75 f$) in the center of the cyclone (anticyclone).

The distant-dipole experiments "DISTJET" are initialized with the same cyclonic and anticyclonic vortices as in MDJET but separated by an initial distance of 3600 km between the vortex cores, twice of that in MDJET. Because of this large distance, the initial conditions of DISTJET contain no jet (not shown). Nevertheless, a localized jet develops at a later time (Section 5) as the vortices slowly approach each other.

b. Model configurations

All simulations, unless otherwise specified, are configured with two domains through two-way nesting. The 90-km coarse domain has dimensions of 150, 160 and 120 in the *x*, *y* and *z* directions, respectively. The vertical spacing is 200 m for the experiment MDJET but is stretched for SFJET with more vertical levels near the surface. The 30-km fine domain focuses on the dipoles with 241 grid points in both *x* and *y* directions. The model top pressure is 10 hPa, or 24 km. To minimize the reflection of gravity waves from boundaries, a Rayleigh-type sponge layer is included near the model top, in addition to the MM5 built-in radiative boundary conditions (Grell et al. 1995). A sponge layer is also included near the bottom boundary for MDJET. MM5 is configured to have zero tendencies at lateral boundaries. The MM5 built-in diffusion scheme, i.e., the deformation dependent 4th order form, is applied at interior points for all simulations. The horizontal diffusion coefficient K_H used in MM5 is

$$K_H = K_{Ho} + 0.25\kappa^2 \Delta x \cdot D, \qquad (2.2)$$

$K_{H0}=3\text{x}10^{-3}(\Delta\text{x})^2/\text{Dt}$ is a background value. κ is the Karman constant. D is the horizontal deformation $D = \left((u_x - v_y)^2 + (v_x + u_y)^2\right)^{1/2}$ (Smagorinski et al. 1960). K_H is bounded by an upper limit $(\Delta\text{x})^2/\text{Dt}/64$ to ensure numerical stability.

2.3 Simulated gravity waves from jet-dipoles

This section discusses differences in gravity waves between MDJET and SFJET. It is suggested that wave generation is closely related to localized jets. The shift of the localized jet toward the anticyclone in MDJET is discussed. Finally, the relevance of flow imbalance is discussed.

a. Gravity waves from the two types of vortex dipoles (MDJET, SFJET)

The vortex dipoles in MDJET and SFJET drift eastward very slowly with a translation speed of ~1.2 m/s and ~ 1.1 m/s, respectively. This slow drift arises from the mutual advection of the vortices, as discussed in SMPZ07. In MDJET, for reasons not completely apparent at this time, the dipole jet system as a whole also rotates gradually anticlockwise with the primary jet axis turning gradually to the left, e.g., from due east at 0 h in Fig. 2.1a to east-northeast at 210 h in Figs.2.2a. Owing to nonlinear interaction among vortices, both vortices undergo a slow deformation. This is more apparent for the cyclonic vortex, which becomes more elongated along the primary jet axis. In the meantime, the two vortex centers also draw closer to each other, corresponding to a slight increase in the maximum jet speed and thus slight increase in the Rossby number. Figure 2.3a-b shows the time evolution of the horizontal wind speed along a straight line that always connects the two vortex centers in MDJET and SFJET, respectively.

Low-frequency inertia-gravity waves appear in both MDJET and SFJET in the exit regions of the localized jets (Fig.2.2). More specifically, for MDJET, there are two distinct groups of gravity waves simulated. The gravity waves of primary interest are nearly phase locked with the jet, propagate nearly symmetrically both upward and downward, and are confined to an area 6-16 km above ground level (AGL). A different, transient group of gravity waves also appears in the jet exit region above 16 km and below 6 km (Fig. 2.2b). These waves weaken gradually and eventually disappear after long integrations (e.g. Fig. 2.4 d) and were thus attributed to initial adjustment by

Viúdez (2008). The jet-exit region gravity waves from the SFJET are similar to the upward propagating waves at and above the jet-core level in MDJET (Fig.2.2). Waves

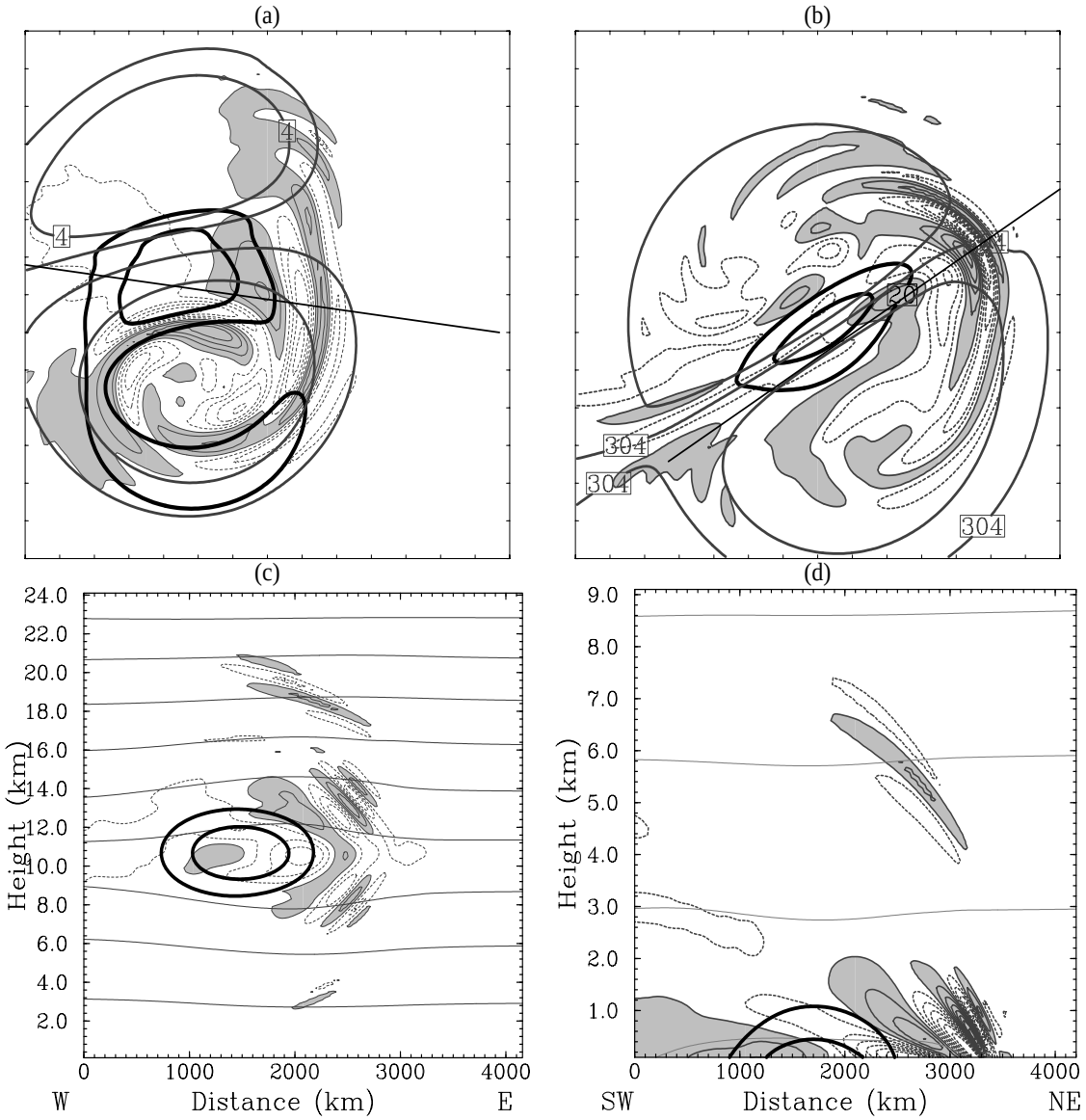

Figure 2.2 The upper panels are the horizontal views of the vortex dipoles with divergence (ci = $0.01\times10^{-4}s^{-1}$; positive, shaded; negative, dashed), potential temperature (gray, ci = 20 K) and wind speed (black lines, ci = 5 m/s, values < 20 m/s omitted) on the 30 km domains for (a) MDJET at 12.5 km valid at 210 h and (b) SFJET at 0.5 km at 210 h. The bottom panels show divergence for (c) MDJET and (d) SFJET at the vertical cross sections indicated by black lines in the corresponding upper panels. The distance between ticks in upper panels is 900 km.

appearing in the immediate exit region of the jet core in both simulations have phase lines that are nearly stationary with respect to the jet.

Nevertheless, the gravity waves in the jet-exit-region of SFJET and MDJET differs noticeably. The wave pattern is more asymmetric about the dipole axis in MDJET with a significant portion extending to the anticyclone. The preferred occurrence of waves in the anticyclonic side persists over the entire simulation of MDJET. However, this is not surprising if we consider that the localized jet shifts to the anticyclone in the mid-level dipole from beginning and also persists (Fig.2.3 a and c). The shift of the initial jet toward the anticyclone in MDJET results from the prescribed EPV distribution and induced asymmetry between anticyclones and cyclones. The EPV may be written as

$$\begin{aligned} Q &= \frac{g}{\rho\theta_0}[(\zeta_z + f)\cdot\left(N^2 + \frac{\partial b}{\partial z}\right) + \zeta_x \cdot \frac{\partial b}{\partial x} + \zeta_y \cdot \frac{\partial b}{\partial y}] \\ &= \frac{g}{\rho\theta_0}\left(f \cdot N^2 + \zeta_z \cdot N^2 + f \cdot \frac{\partial b}{\partial z} + \zeta_z \cdot \frac{\partial b}{\partial z} + \zeta_x \cdot \frac{\partial b}{\partial x} + \zeta_y \cdot \frac{\partial b}{\partial y}\right) \end{aligned}, \qquad (2.3)$$

where b is buoyancy, and (ζ_x, ζ_y, ζ_z) are the three components of vorticity. The first term (the product of planetary vorticity f and reference static stability) is the reference EPV, and the subsequent terms are PV anomalies from the reference EPV, with the 2nd and 3rd terms being linear and the rest being quadratic. From scale analysis (Rotunno etal. 2000), the linear terms are one order smaller than reference EPV [~O(Ro)] and the quadratic terms are O(Ro^2) (details in Appendix III). Because the wind profile near the vortex center is near zero, however the horizontal terms are very small and thus will not be considered here. The sign of linear terms depends on vorticity and are negative in

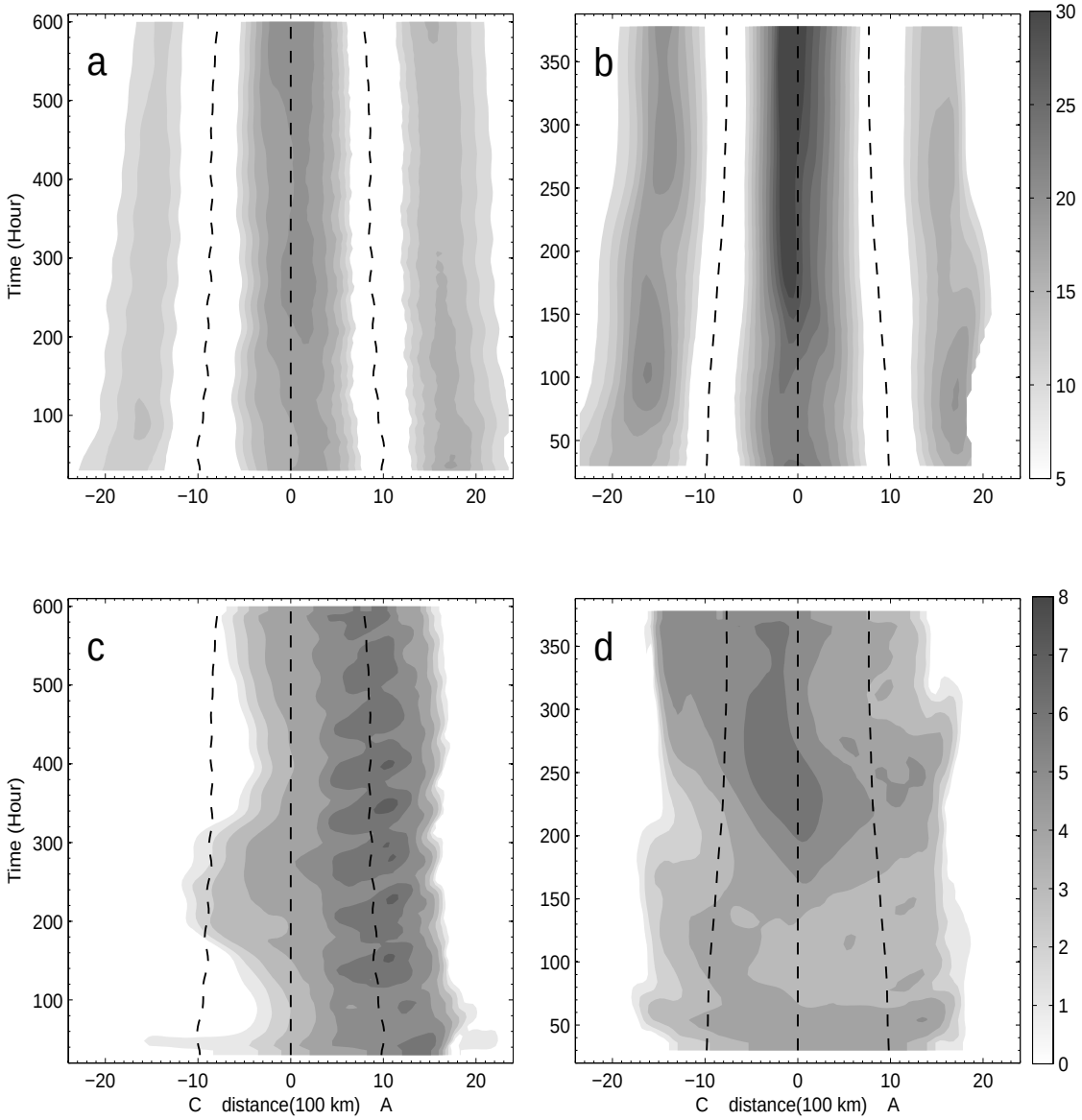

Figure 2.3 Hovmoller diagrams of wind speed along the centers of the cyclone and anticyclone. The centers of vortex dipoles (indicated by black dash lines) are defined by the perturbation potential temperature contours of -5 k and 4 k at 11.6 km for (a) MDJET and contours of +/-10 k at 0.5 km for (b) SFJET. Contours of wind speed less than 5 m/s are omitted. Note that the vortex centers are symmetric about the line of 1500 km. Wave variances are plotted in (c) for MDJET and (d) for SFJET. See text for details.

anticyclones and positive in cyclones. In contrast, the quadratic term $\zeta_z \cdot \frac{\partial b}{\partial z}$ is always positive in both cyclones and anticyclones. As a result, the relative vorticity and static stability are stronger in the anticyclone than in the cyclone, regardless of the equal magnitude of the prescribed EPV anomalies. According to Kelvin's circulation theorem, stronger vertical vorticity in the anticyclone is associated with strong wind speed (Fig. 2.1c), which induces shift of the localized jet (or wind contours) toward the anticyclone.

Time evolution of the localized jet and wave variance are compared in the mid-level dipole and the surface dipole. Figure 2.3 shows the Hovmoller diagram of wind speed and wave activities (defined below) along the line connecting the vortex cores. This line and one of its perpendiculars (i.e., the dipole axis) are chosen as x and y-axis, and define a frame with the origin located at the midway of vortex cores. In general, the vortex dipole and the localized jet remain relatively stationary throughout the integration time period. To quantify how much wave activities varies along the direction perpendicular to the dipole (y) axis, we define wave variance as the variance of filtered divergence along the dipole axis. The filtered divergence is obtained by applying a two-dimensional (2D) high pass filter with 240 km cut-off wavelength to the horizontal divergence at 12.5 km. This digital filtering technique is a 2D convolution operation between the data and a chosen window. It is the same as in Wang and Zhang (2007) except that a Chebyshev window (41x41 grid points) is adopted here. Figures 2.3 c and d show the time evolution of the calculated wave variance. For MDJET, most wave variance is found near the anticyclones where the curved jet is shifted. In the surface

dipole they are found close to the cyclones where slighter stronger wind is also found. The phase locking between the jet and the gravity waves in the exit region in MDJET and SFJET suggests the generation of these gravity waves is related to the localized jets. Close inspection of wave variance in Fig. 2.3 shows that wave variance increases as the jet between the dipoles slowly evolves.

b. Gravity waves and flow imbalance from the mid-level dipole

The stationary gravity waves propagate upward (downward) downstream of an area of divergent (convergent) flow above (below) the jet level (Fig. 2.2a). The phase of these upward and downward propagating waves differs due to the changing sign of vertical wave number, while the amplitude probably differs due to decreasing density with increasing height. The most conspicuous wave bands (Fig. 2.2 a) have weak amplitude with maximum divergence reaching $0.03\times10^{-4}s^{-1}$ and a horizontal (vertical) wavelength ~300 km (2 km). Using the dispersion relation for inertia-gravity waves and a background static stability $N^2=2\times10^{-4}s^{-2}$, the roughly estimated wave frequency is 1.4 *f*, close to the inertial frequency. The horizontal and vertical wavelengths and the intrinsic frequency of these waves are larger than those of the waves simulated in the surface dipole of SMPZ07 (70 km, 520 m and 1.1 *f*). The transient wave packets further away from jet-core level (above 16 km or below 6 km) have non-stationary phase lines that can barely be separated from the phase-locked waves near the jet core at 90 h (Fig. 2.4b). The intrinsic frequency of these transient waves tends to approach to the inertial limit at later times and they eventually disappear in the divergence fields after ~ 540 h (Fig. 2.4). Figure 2.4 also shows a slight strengthening of the localized jet and a slight

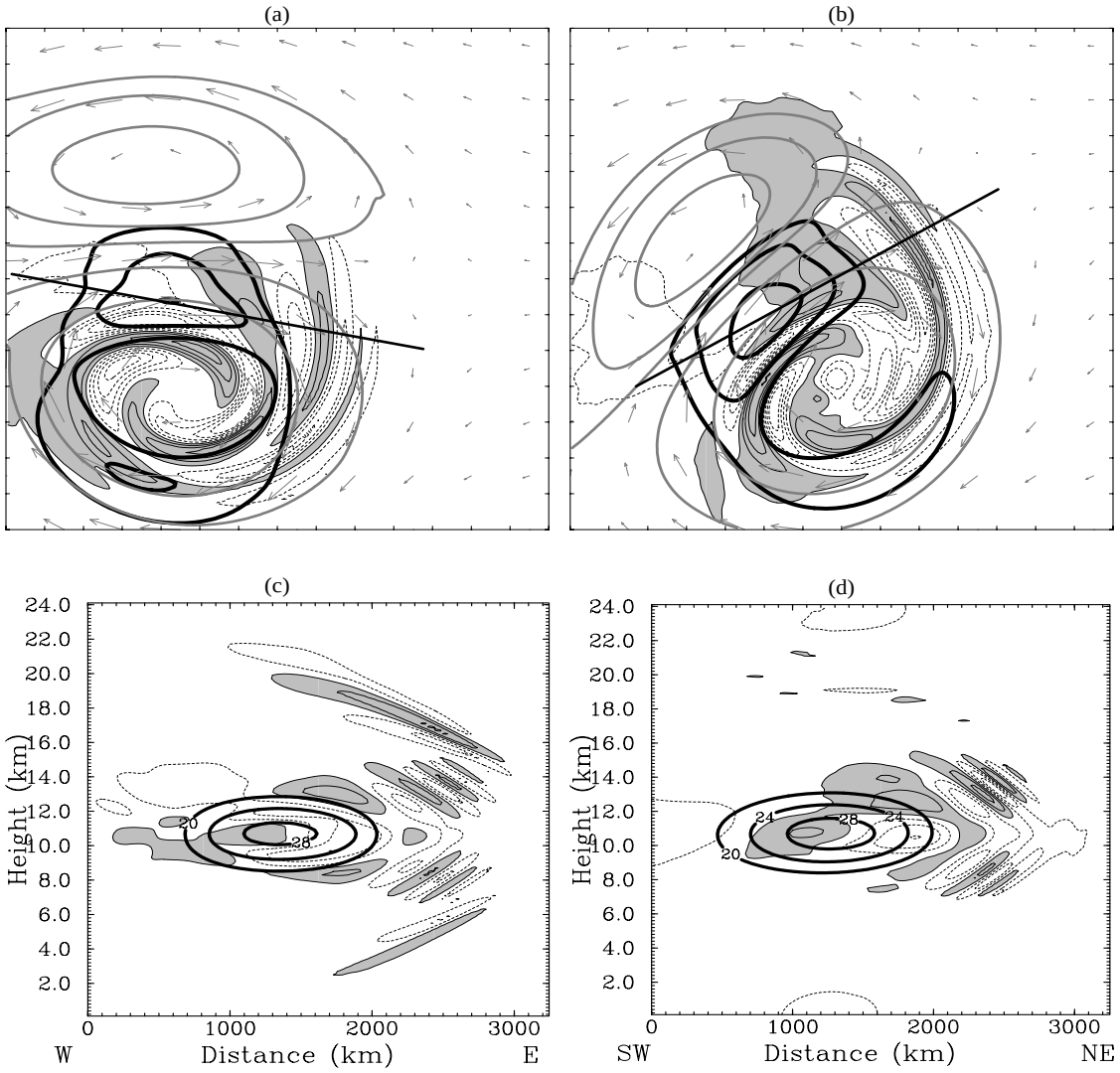

Figure 2.4 Horizontal divergence (ci = $0.1\times10^{-5}s^{-1}$), wind speed (black, ci = 5 m/s, starting from 20 m/s) and PV (gray, ci = 1 PVU) at 12.5 km from middle level dipole valid at (a) 90 h and (b) 540 h, and along the cross sections at (c) 90 h and (d) 540 with their location indicated by black lines in the corresponding upper panels. The distance between adjacent ticks in (a) and (b) is 300 km.

increase in wave amplitude from 90 h to 540 h, in line with Hovmoller diagram in Fig. 2.3. We will attempt to quantify the dependence of wave amplitude on jet strength in the latter Section 2.5.

The weak wave emission from vortex dipoles discussed above is different from jet-front systems studied by Zhang (2004) in that baroclinic waves evolve much faster (a few inertial periods), and continuous strengthening flow imbalance is generated. Flow balance refers to a physically realizable flow state in the absence of any hydrodynamic instabilities or gravity waves, and flow imbalance is any departure from the balance in consideration (Hoskins et al., 1985). We use ΔNBE as a measure of flow imbalance (Zhang et al. 2000),

$$\Delta NBE = 2J(\psi_y, -\psi_x) + f\zeta - \alpha\nabla^2 P, \tag{2.4}$$

where ψ , ζ and α are stream function, relative vorticity and specific volume, respectively.

Figure 2.5 shows a snapshot of the flow imbalance (ΔNBE) at 210 h, when ΔNBE reaches $2\times10^{-10}s^{-2}$ in the jet exit region downstream of an area of negative ΔNBE. Waves with upward and downward group velocity appear above and below this area of negative ΔNBE (Fig. 2.5b). Compared with gravity waves from the idealized baroclinic wave simulations (Zhang 2004), both the magnitude of ΔNBE and the gravity waves are much weaker, which is possibly due to the absence of baroclinic instabilities in the dipole simulations. However, it is not clear from these diagnostics how the waves are related to flow imbalance (Zhang 2004, Plougonven and Zhang 2007).

Figure 2.6 shows the unbalanced potential temperature and relative vorticity at 210 h. The unbalanced flow is recovered by subtracting the balanced flow from the total flow, while the balanced flow is obtained following the same procedures of EPV inversion as Davis and Emanuel (1991). Consistent with the flow imbalance diagnosis in Fig. 2.5, the unbalanced flow is very weak compared with the total flow and the balanced flow. Besides the wave signals in the jet exit regions, unbalanced flow seems to be stronger in the anticyclones than in the cyclones, which could be due to wave trapping as discussed in the ray tracing analysis (see below).

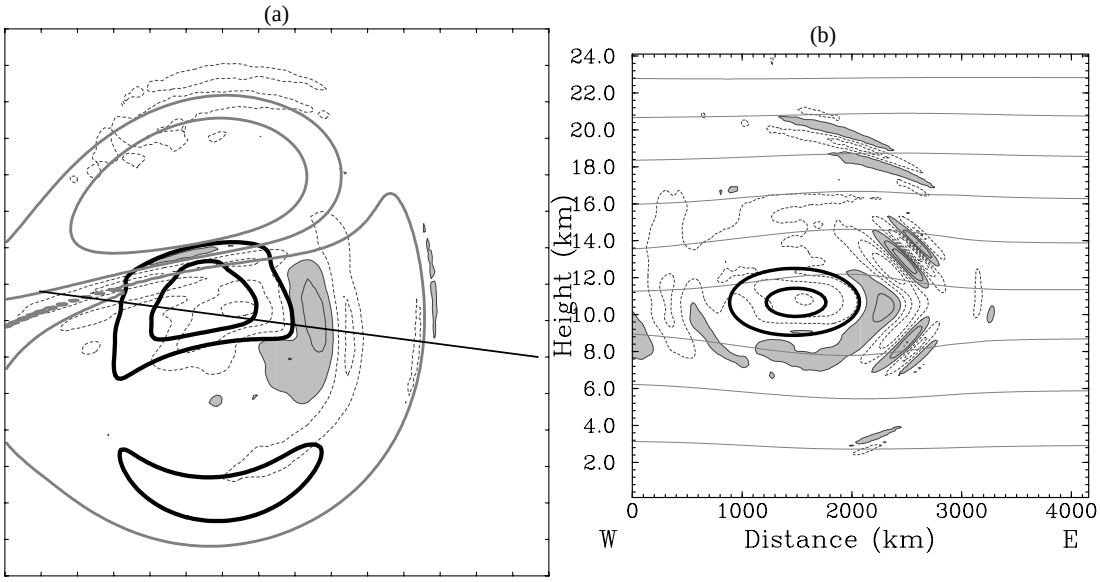

Figure 2.5 ΔNBE (ci = $0.01\times10^{-8}s^{-2}$, positive values, shaded, negative values, dashed lines) at 210 h from MDJET is plotted at 10.5 km (a) and along the cross section indicated by the straight line in (a).

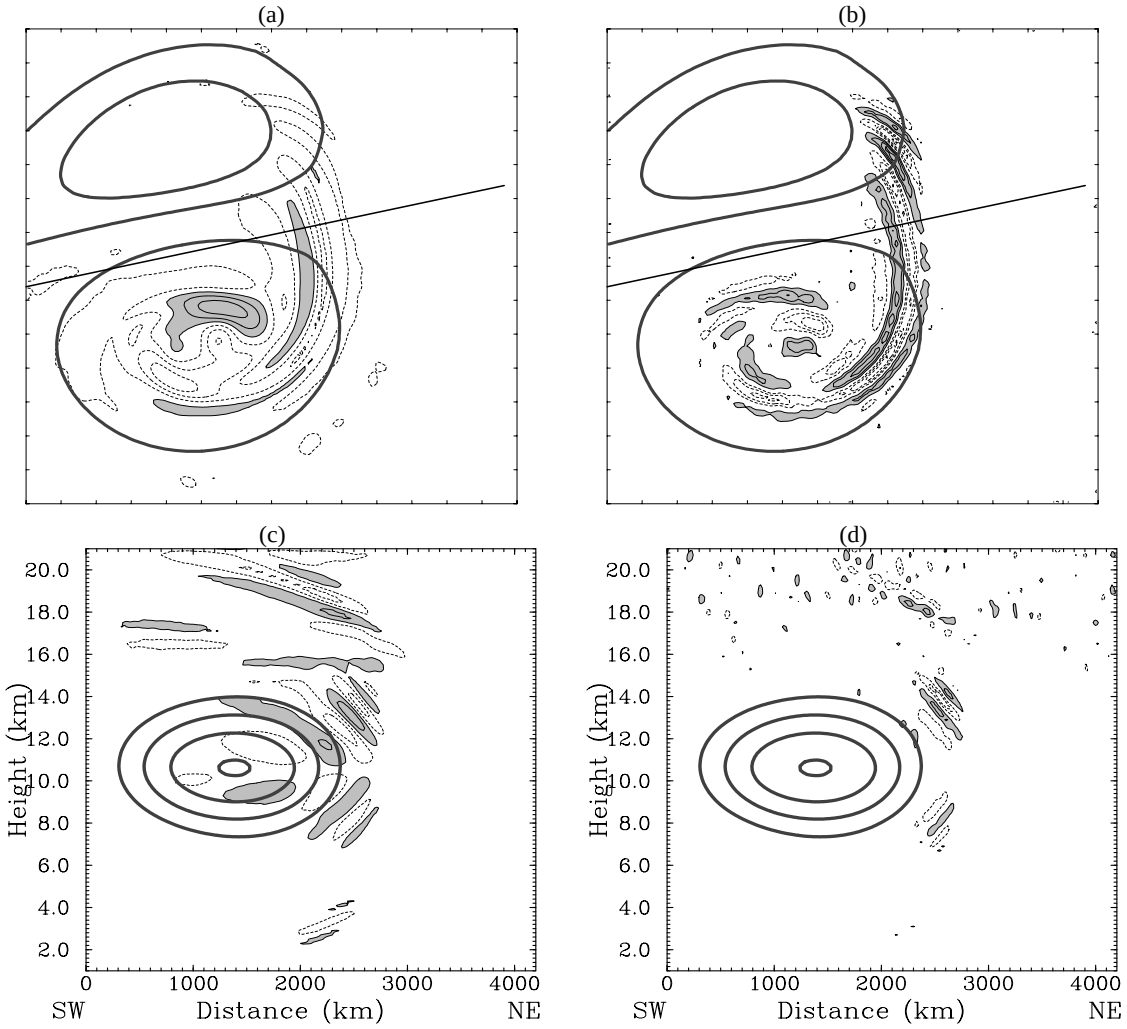

Figure 2.6 Upper panels show unbalanced potential temperature (a) with ci = 0.05 K, and unbalanced relative vorticity (b) with ci= $0.008 \times 10^{-5} s^{-1}$ at 13.5 km, overlapped on wind speed and potential vorticity (ci = 1.5 PVU) at 11.5 km. Bottom two panels show along the vertical cross sections unbalanced potential temperature (c) (ci = 0.05K), and unbalanced relative vorticity (d) (ci= $0.008 \times 10^{-5} s^{-1}$), and wind speed (ci = 5 m/s, values less than 15 m/s depressed). The vertical cross sections are indicated by thick lines in top panels.

2.4 Ray tracing for the gravity wave propagation

Ray tracing of wave packets (Jones 1967; Lighthill 1978) can be used to study wave refraction due to variations of background flow. Some authors have applied ray tracing to investigate gravity wave propagation in three-dimensional flows (e.g. Dunkerton and Butchart 1984; Marks and Eckermann 1995; Ollers et al. 2003). Lin and Zhang (2008) studied the wave characteristics along rays of gravity waves in the baroclinic jet-front systems simulated in Zhang (2004). Next we will use the numerical ray-tracing model GROGRAT (Marks and Eckermann 1995; Eckermann and Marks 1997) to examine the propagation properties of jet-exit region gravity waves from the dipole flow. The ray tracing in GROGRAT is based on the dispersion for plane waves:

$$\omega_i^2 = (\omega - Uk - Vl - Wm)^2 = \frac{N^2(k^2 + l^2) + f^2(m^2 + \alpha^2)}{k^2 + l^2 + m^2 + \alpha^2}, \qquad (2.5)$$

where ω_i and ω are intrinsic frequency and absolute frequency, (*k, l, m*) are three components of wavenumbers, and u, v, w are the components of the spatially and temporally varying background flow.

The ray-tracing model requires the initial wave parameters in the augmented parameter space (k, l, m, x, y, z). In this study, rays are mainly released from the possible source area (the jet exit region) with horizontal wavelengths of several hundred kilometers. Hundreds of hypothetical rays are released at 11 km in the jet exit region, having horizontal wavelengths ranging from 150 km to 750 km, intrinsic group speeds less than 9 m/s, intrinsic frequencies of 1-3 f, and Doppler-shifted phase speeds between -2~2 m/s. These values are chosen to account for the uncertainties for the estimated

initial wave parameters. Ray calculation cannot reach infinite time in GROGRAT. In the current calculation, ray integration stops based on two conditions: (1) their vertical group velocity reaches some a small value, 10^{-3} m/s, (2) integration reaches the time limit such that background wind is not available anymore. In most cases it takes at most a few inertial periods for rays to travel out of jet region that is characterized by strong flow diffluence.

Figure 2.7 shows the paths of four rays and the changes of wave parameters with respect to height. Two rays, S1 and S2, are released from the same location almost exactly in the jet exit region, while another two rays N1 and N2 start from the locations displaced to the north of S1 and S2 by 150 km. The rays N1 and N2 have horizontal wave vectors parallel to x axis (and also nearly parallel to the jet axis), while S1 and S2 have wave vectors making an angle of 45^{o} with the x-axis. These rays can travel 1000 km horizontally and as high as 16 km vertically (Fig. 2.7a). During their propagation, the initial horizontal wavelength of 750 km decreases to below 400 km at the height of 14 km and to below 200 km at 15 km (Fig. 2.7c). The vertical wavelength also decreases below less than 2 km (Fig. 2.7d). The intrinsic frequency approaches the inertial limit of gravity waves with the value less than 1.5 f (Fig. 2.7b). The decease of intrinsic frequency indicates the wave frequency is higher than that seen in the far exit region of the jet.

The phase speed relative to the mean wind (Ci) decreases to near zero (Fig. 2.7e), indicating the possible horizontal critical levels where the ground based phase speed matches the mean wind. The decreasing vertical group velocity also suggests the critical

levels (Fig. 2.7f). The inertial critical levels are not unexpected when upward/downward waves propagate far away from the jet core to the levels of reduced winds that satisfy $|u-c| = f/k$, where u and c are the wind speed and the phase speed.

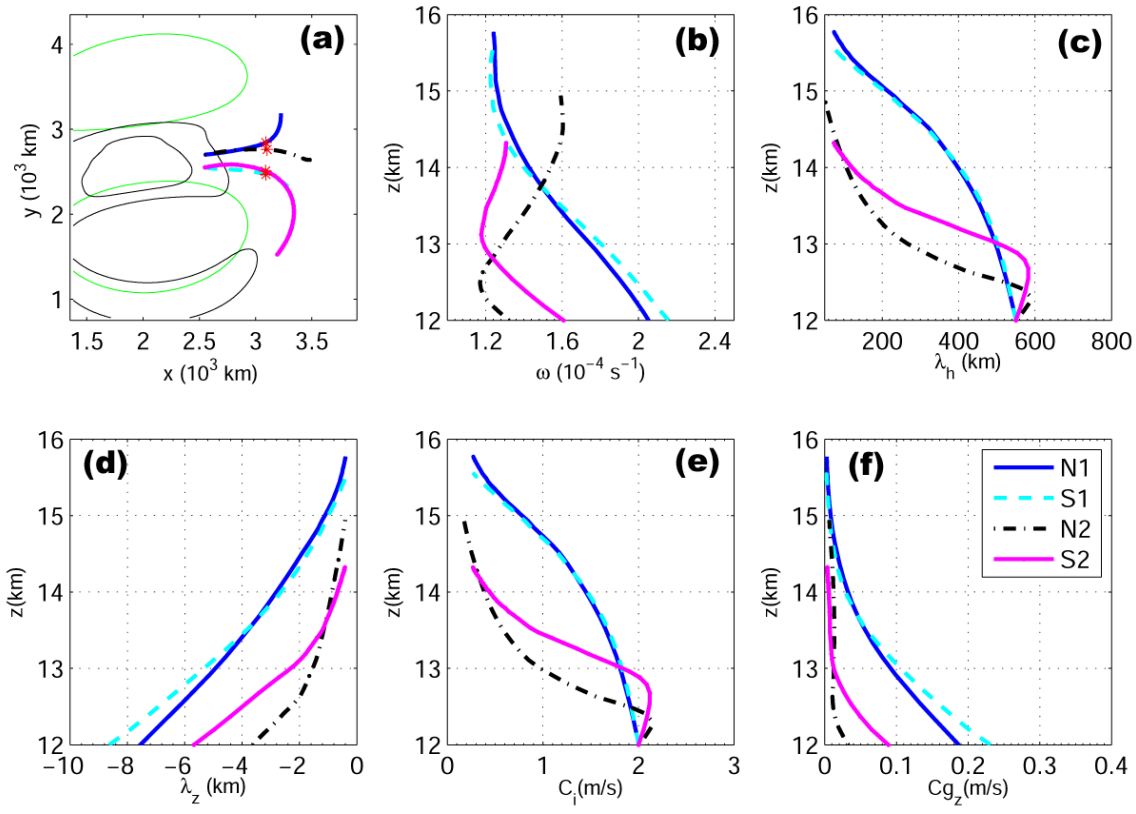

Figure 2.7 Ray paths in the horizontal views (a) overlapped on wind speed contours (25 m/s and 30 m/s) and perturbation potential temperature (+/- 4K) on 11.6 km; intrinsic frequency (b), horizontal wavelength (c), vertical wavelength (d), intrinsic horizontal phase velocity (e), vertical intrinsic group velocity (f). See text for details.

The shrinkage of wavelengths indicates possible wave scale selection mechanisms. Plougonven and Snyder (2005) have discussed one such mechanism. They show that a specific wind structure that has constant horizontal deformation and constant vertical wind shear can effectively select the horizontal and vertical wavelengths. Specifically the horizontal wave vectors tend to align with the contraction axis of the local wind, while the tilt of wave vectors tend to converge to a value given by the ratio of vertical shear and deformation. This is also the the wave capture mechanism discussed by Bühler and McIntyre (2005). Strong deformation and wind shear is indeed present in the jet exit region of the three-dimensional dipole flows. However, usually the derivatives of winds are not constant. As discussed in SMPZ07, the wave capture is a long-term asymptotic result. Wave packets propagate through varying winds in a limited time, such that wave capture may not occur.

One can assess the capture mechanism using the four-dimensional ray-tracing model. Wave capture mechanism predicts that the vertical tilt and horizontal azimuth of wave vectors is determined by the local contraction axis at large times. The angle of local contraction axis α is determined by

$$\tan(2\alpha) = (v_x + u_y)/(u_x + v_y)\,, \tag{2.6}$$

and vertical tilting γ of the wave vector is

$$\tan(\gamma) = \sqrt{(v_x + u_y)^2 + (u_x - v_y)^2}\,\Big/\,2\left|\vec{V_z}\right|, \tag{2.7}$$

where u_x, u_y, v_x, v_y are local wind gradients, and $\vec{V_z}$ are wind shear in the direction of contraction axis α. On the other hand, the horizontal azimuth angle and the tilt of wave

vectors can be calculated directly from the ray tracing results. Therefore the calculated values can be compared to the predicted ones. The comparison is performed in the region of strong deformation (the dots in Fig. 2.7a). N1 (S1) has a predicted tilt and azimuth angle 0.276^0 (0.261^0) and 12.7^0(-2.3^0), generally in agreement with calculated tilt 0.29^0 (0.770^0) and azimuth angle 16.4^0 (-9.2^0). Nevertheless, N2 (S2) has a predicted vertical tilt 0.544^0 (0.344^0) but much smaller calculated vertical tilt 0.297^0 (0.259^0). The numbers are summarized in Table 2.1 and plotted in Fig. 2.7. In general, good agreement with the wave capture mechanism is found for rays having wave vectors pointing nearly parallel to jet axis, while the predicted vertical tilt shows large differences from the calculated values. Two scatter plots (Fig. 2.8, the square and star points denote results from N1 and S1, and the plus and diamond from N2 and S2.) show the disparity between the predicted values of vertical tilt and the calculated values. Additionally, hundreds of rays are released from the two locations with different initial wavelengths and phase speeds and are processed in the similar way to the four rays. They can be divided into 2 groups: the first group (G1) has wave vectors nearly parallel to x-axis (dark black dots in Fig. 2.8) and the second group (G2) have wave vectors making a 45^0 angle with the x-axis (light red dots in Fig. 2.8). In general, G1 shows good agreement between calculations and predictions from the wave capture mechanism, while G2 show large discrepancies, especially for the vertical tilt.

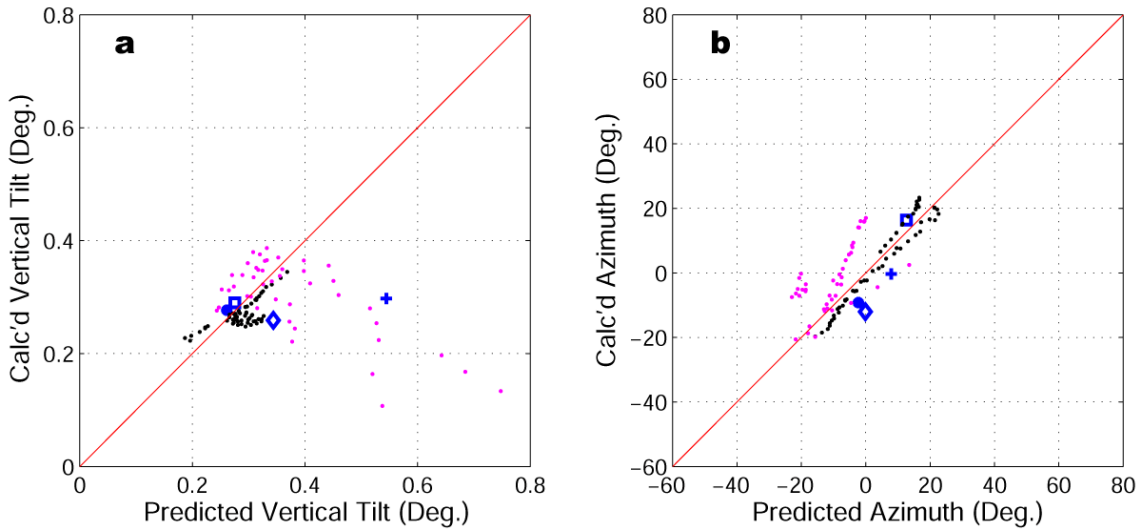

Figure 2.8 Scatter plots of calculated and predicated vertical tilt of wave vectors in the left panel (a), calculated and predicated azimuth angles of wave vectors in the right panel (b). The square and star points are results from rays N1 and S1. The plus and diamond points are from N2 and S2. The black dots are results for rays initialized from the rays having wave vectors nearly parallel to x axis. The red dots are results for rays initialized from the rays having wave vectors making 45^0 with x axis.

Table 2.1. The predicted vertical tilt, the calculated vertical tilt, the predicted azimuth and the calculated azimuth for four rays N1, S1, N2 and S2 indicated by the stars in Fig. 2.7 a.

	Pre'd Tilt	Calc'd Tilt	Pre'd Azri.	Calc'd Azri.
N1	0.276	0.290	12.7	16.4
S1	0.261	0.277	-2.3	-9.2
N2	0.544	0.297	7.9	-0.3
S2	0.344	0.259	-0.0930	-12.0

The dispersion relation based on the constant wind assumptions in GROGRAT could potentially cause some inaccuracy in regions of strong vorticity. Kunze (1985) considered a different dispersion relation that is based on geostrophic winds assumption and found that the lower limit of inertia-gravity waves, in the region of strong vortical motion, should be replaced by the effective Coriolis parameter $\sqrt{f\left(f+\zeta\right)}$ or $\left(f+\zeta/2\right)$, where ζ is the relative vertical vorticity. Figure 2.9a shows that the effective Coriolis parameter in the vortex dipole increases in the cyclone but decreases in the anticyclone. Some very low frequency waves (less than *f*) can be effectively trapped in the anticyclonic regions where the effective Coriolis parameter reduces to ~0.8*f* (Fig. 2.9b). In the cyclonic regions, near inertial waves can encounter the horizontal critical level where the intrinsic frequency approaches the increased effective Coriolis parameter, which can potentially prevent waves from propagating into the cyclone and is partially responsible for the pronounced wave activities in the anticyclones. Nevertheless, the inclusion of the effective Coriolis parameter and more elaborate dispersion relation should not change the conclusions from the ray-tracing analysis in this study, since the ray tracing is performed mostly in the jet-exit region with small relative vorticity.

The above analysis demonstrates through the ray-tracing analysis that strong wave refraction due to the background wind. Specifically, the horizontal wavelength and vertical wavelength both decrease; the intrinsic frequency approaches the inertial frequency and intrinsic phase speed and vertical group speed decrease to zero. The vertical tilt and horizontal azimuth angle of wave vectors from ray-tracing results are

compared with the wave capture mechanism. Although good agreement is found in some rays, large discrepancies are also found, suggesting that the wave capture mechanism may be overly simple. However, other factors, such as three-dimensional critical levels and the effective Coriolis parameter need to be investigated in the future.

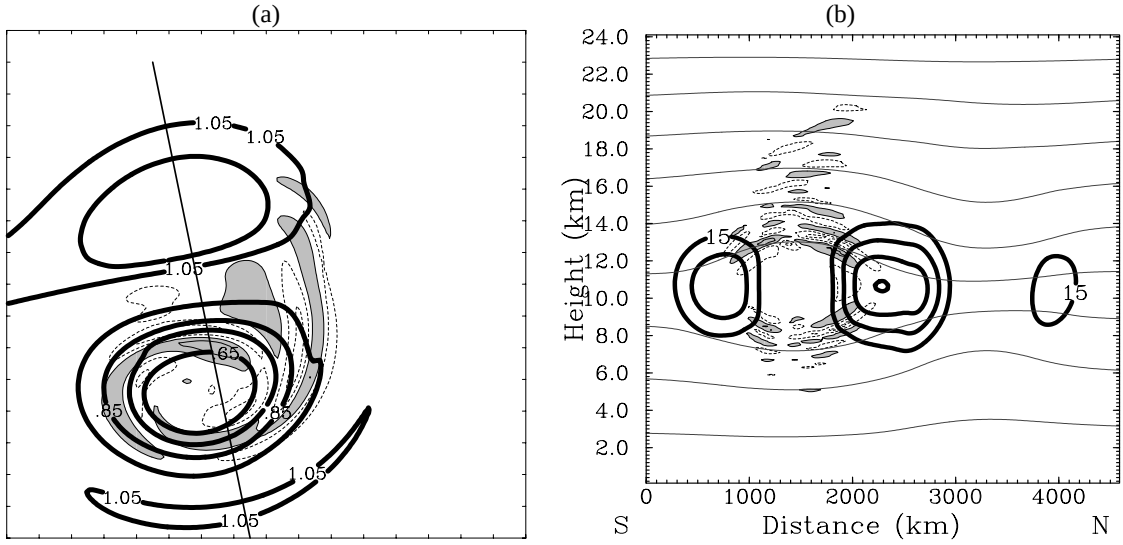

Figure 2.9 Panel (a) shows the effective Coriolis parameters (ci = 0.05 f), divergence (ci = $0.02 \times 10^{-4} s^{-1}$; positive, shaded; negative, dashed) and wind vectors from MDJET valid at 210h at 12.5 km. Panel (b) shows divergence, wind speed (ci = 5 m/s) and potential temperature (ci = 6K) in the vertical cross section indicated by thin line in (a).

2.5 Dependence of wave amplitude on Rossby number

An important issue of spontaneously generated gravity waves is how the amplitude depends on the Rossby number. From analytical models, Vanneste and Yavneh (2004) demonstrated in a simple, analytically tractable flow that spontaneously emitted gravity waves were exponentially small in Rossby number when Ro <<1. Plougonven et al. (2005) showed that instabilities of a baroclinic vertical shear that coupled inertia-gravity waves and balanced surface edge waves had growth rates that also increased exponentially with Rossby number. These models differ from gravity wave emission in a shallow water model studied by Ford (1994) and Ford et al. (2000) in that the wave scales are not necessarily much larger than that of the vortical flow. To assess wave-amplitude dependence in the dipole model, SMPZ07 simulated several vortex dipoles with different initial strengths and suggested that the wave motion has a power-law dependence on the maximum wind speed (essentially Rossby number). Here, we examine gravity waves in slowly amplifying dipole jets, and thus present an alternative way to quantify the dependence of wave amplitude on Rossby number.

The localized jets examined here emerge and amplify due to interactions between cyclones and anticyclones that are initially separated by a large distance, and subsequently approach each other, developing into dipoles (pairs). This process of vortex paring excludes the possibility of baroclinic instability, although the vortex interactions are not yet fully understood. In the next step, we demonstrate that cyclones and anticyclones can develop into a vortex dipole and remain coherent for long times, while the jet strength amplifies with time.

Similar to the mid-level dipole experiment discussed before, the initial balanced flow is created from cosine-squared EPV perturbations except that the initial distance between the cyclone and anticyclone is doubled to 3600 km. Because of the large distance between the vortices, the initially balanced flow contains no localized jet with a Rossby number of ~ 0.06. To further minimize the adjustment, the flow fields of first 36 hours are averaged, similar to SMPZ07, and the averaged flow fields are used to reinitialize the numerical model. Two additional experiments are performed in which the EPV perturbations are either increased or reduced by 20%. These three 'distant dipole' experiments are referred as medium, strong, and weak DISTJET; medium DISTJET will be discussed in detail below. These DISTJET simulations are integrated over 50 days in a domain of 150x160 grid points with 90-km horizontal grid spacing. Another simulation with a large domain of 240x250x120 grid points is also performed as a sensitivity test to medium DISTJET; the results from medium DISJET discussed below will not change in this large domain simulation. This suggests that boundary effects have very limited influence on the formation of the dipole vortex, as discussed below, although the exact mechanism is not clear at this time.

Figure 2.10 shows snapshots of the vortex dipoles at different times. The vortices approach each other with the distance between the vortex cores decreasing to ~ 3000 km at 240 h. Meanwhile, a slightly curved, localized jet with maximum wind speed > 20 m/s to the anticyclonic side of the dipole appears after ~240 hours. Some wave bands located at the edge of the anticyclone gradually gain strength in the immediate exit region of the jet. Beginning at 360 h (Fig. 2.10 c), a large-scale, four-cell pattern of divergence also

gradually appears around the localized jet and strengthens with time. At 720 h (Fig. 2.10. g), the maximum wind speed of the localized jet reaches the maximum wind speed of ~ 30 m/s, while the four cell divergence pattern and the embedded wave region expands with increasing wave amplitude. The increase of wind speed and decrease of distance renders a larger Rossby number (0.12) at this time, which is more than double that at the initial time.

Figure 2.11 further illustrates the embedded wave signals at 12.5 km by filtering out the large-scale divergence. A two-dimensional, high-pass digital filter is applied to the horizontal divergence with a cut-off wavelength of 720 km. In general, more and stronger wave variance is found in the slowly amplifying jet from DISTJET.

Figure 2.12 shows Hovmoller diagrams of wind speed along the vortex cores at 11.5 km in the frame moving with the dipoles. The moving frame is defined similarly as in MDJET (Fig. 2.3), with the origin located in midway between the vortex cores (which are indicated by dots in Fig. 2.10), and the x axis connecting the vortex cores. The localized jet between the vortices amplifies with time in all three experiments (Fig. 2.12 a-c).

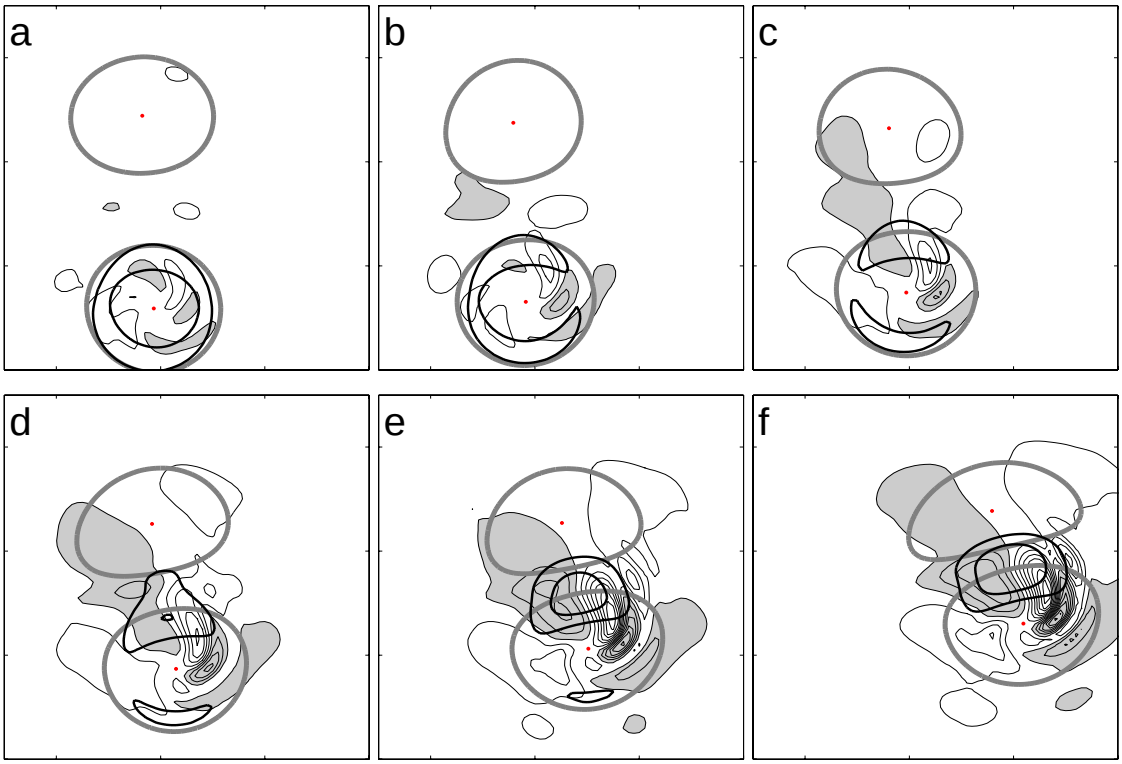

Figure 2.10 Horizontal divergence (ci = $0.02 \times 10^{-4} s^{-1}$; positive, shaded; negative, dashed) is over plotted on perturbation EPV (ci = +/- 1 PVU) and wind speed (blue lines, ci = 5 m/s, values < 20 m/s omitted) on 90 km domains valid at (a) 120 h, (b) 240 h, (c) 360 h, (d) 480 h, (e) 600 h, (f) 720 h.

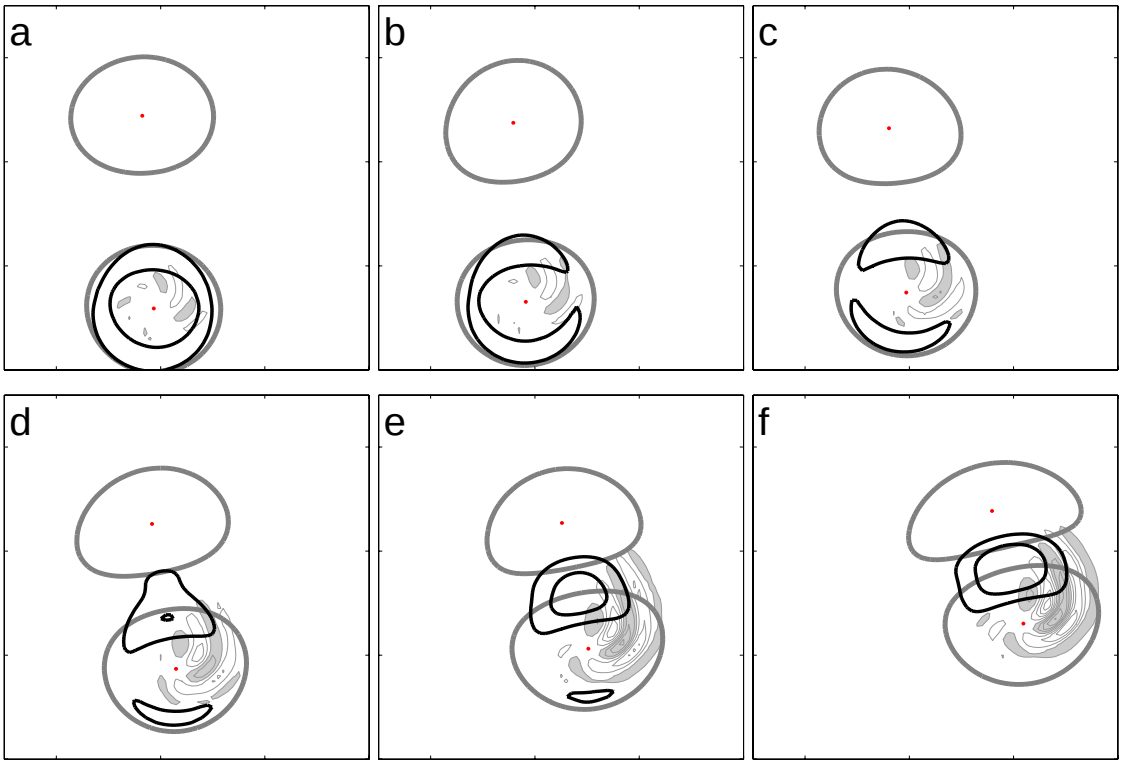

Figure 2.11 The same as Fig. 2.10 except a high-pass filter with a cut-off wavelength 720 km is applied to the horizontal divergence.

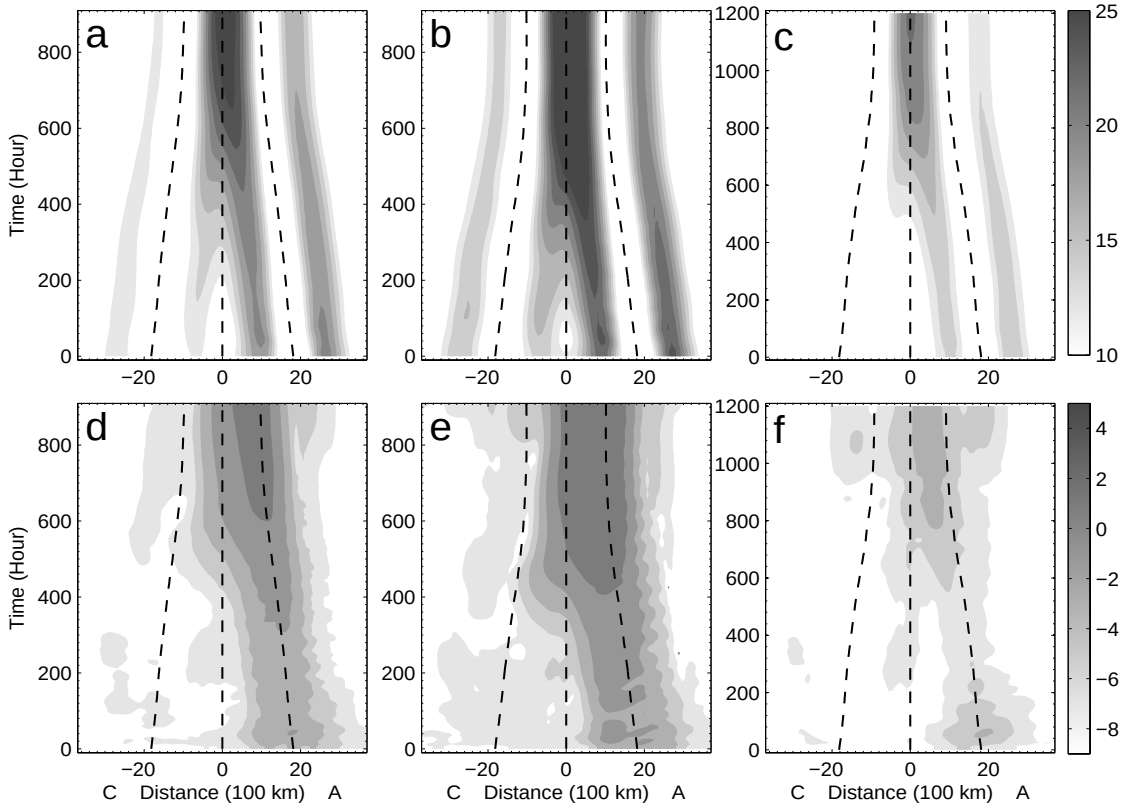

Figure 2.12 Hovmoller diagrams of wind speed (ci = 1 m/s) along the centers of the cyclone and anticyclone for the three case (a) the medium dipole, (b) the strong dipole and (c) the weak dipole. Hovmoller diagrams of wave variance are plotted for these cases in (d), (e) and (f). The centers of vortex dipoles are indicated by black dash lines. Wind speed contours less than 10 m/s are omitted. Note that the vortex centers are symmetric about the central line.

These evolving dipoles are used to infer the dependence of wave amplitudes on jet strength and Rossby number, since the vortex dipole flow evolve with different Rossby numbers. The Eulerian Rossby number is defined as $Ro = U/FL$, where U is the maximum wind speed and L is the distance between the vortex cores. However, other definitions of Rossby number can also be used, e.g., the local Rossby number $Ro = \zeta / f$ as the ratio between the relative vorticity and planetary vorticity. The local Rossby number seems to be less applicable here since it maximizes at the vortex core, which is away from the wave signatures in the exit region of the localized jet. On the other hand, the horizontal scale of jet flow along the streamline seems to be more appropriate, but a lack of an appropriate measure leads us to use the distance between the vortex cores as the horizontal scale to estimate the Rossby number.

Figure 2.13 shows the time series of the Rossby number, wave amplitude dependence on the maximum wind speed, and the Rossby number for all the three DISTJET simulations. Rossby numbers start below or around 0.05 and reach 0.15 in these simulations. Figure 2.13 b also shows a linear fit between the natural logarithm of Rossby number and the natural logarithm of maximum value of filtered divergence (with cutoff wavelength 720 km) at 12.5 km, which is used to represent the amplitude of gravity waves. The slopes of the best-fit lines in the medium, strong and weak DISTJET are ~2.2, 1.8 and 2.4. This suggests that the wave amplitude depends on Rossby number according to a scaling law Ro^{β} with β falling between 1.8 and 2.4 and when Ro falls in the range of 0.05- 0.15. This finding seems reasonably consistent with SMPZ07, where their Rossby number is indicated by the maximum wind speed and β is ~4. For

comparison, the wave amplitude dependence on the maximum winds is also calculated (Fig. 2.13b) with β increasing to 6.0, 4.9 and 6.0 for the three experiments.

To test the resolution dependence of wave amplitude on the Rossby number, the medium-strength DISTJET experiment is performed with 30 km horizontal grid spacing. At this resolution, β increases to 2.76, greater than the values in the 90-km simulations. If the maximum wind speed is taken as a surrogate for the Rossby number, β increases to 7.4, which is also significantly larger than the estimate (6.0) in the 90-km simulations. This increase of β probably arises because smaller scale waves with stronger amplitude appear in the leading edge of the wave front in the simulation with higher resolution.

From these distant-dipole experiments with cyclones and anticyclones initially separated by a large distance, gravity waves are again simulated in the exit region of amplifying jets with increasing amplitude. These simulations further demonstrate that the waves are inherent features of vortex dipoles rather than remnants or adjustment from the initial conditions.

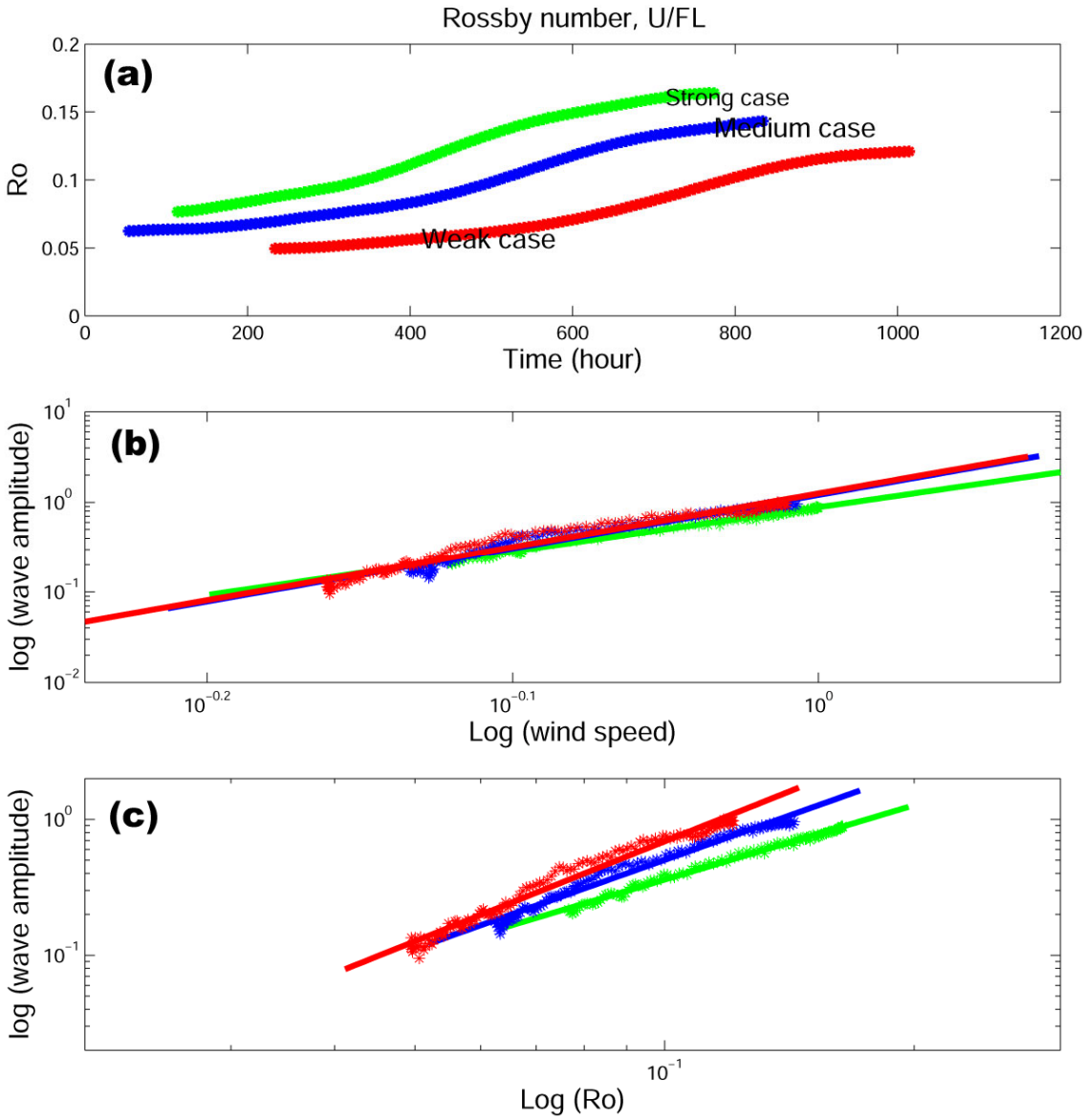

Figure 2.13 (a) Time series of Eulerian Rossby number for the medium (blue), strong (green) and weak (red) distant dipole. (b) The logarithm of the filtered maximum divergence is linearly regressed against the logarithm of Rossby number in each cases, with the slope 2.2, 1.8 and 2.4 for the medium (blue), strong (green) and weak (red) distant dipole, indicating the dependence of wave amplitude on Rossby number. Panel (c) is the same as (b) except the x axis is the logarithm of the maximum wind speed in each case, with the slope 6.0, 4.9 and 6.0.

2.6 Summary and discussion

Owing to their simple structure and slowly evolving nature, vortex dipoles provide an ideal laboratory to explore fundamental mechanisms of spontaneous generation of gravity waves in a rotating, stratified flow. In this study, gravity wave generation and propagation from idealized vortex dipoles and jets are simulated with a nonhydrostatic, compressible mesoscale model. We examine two types of vortex dipoles, which are initialized through potential vorticity inversion and have their maximum strength at either the surface or mid-level in a uniformly stratified atmosphere. In all our dipole simulations, a localized jet arises between the vortex pairs and inertia-gravity waves with intrinsic frequencies 1-2 times the Coriolis parameter appear in the jet exit region when the Rossby number of the flow exceeds 0.15. The gravity waves of interest are nearly stationary with respect to (or phase-locked with) the localized jet. Gravity waves in the surface dipole are quite similar to those simulated in SMPZ07, while waves in the mid-level dipole are more pronounced near the anticyclone. We argue that the preferred appearance of gravity waves in these dipoles is due to the occurrence of the localized jets and their exit region. The phase locking between the jet and gravity waves suggests that the localized jet spontaneously forces these waves.

The propagation of jet-exit region gravity waves in the mid-level dipole is investigated by a ray-tracing model (Mark and Eckermann 1995). The ray-tracing analysis demonstrates that background winds strongly influence the variation of wave characteristics along the ray paths: the horizontal and vertical wavelengths both decrease, the intrinsic frequency approaches the inertial frequency, and the intrinsic

phase speed and vertical group velocity decrease toward zero. While these changes are consistent with those that would precede wave capture (Bühler and McIntyre 2005), the ray-tracing analysis indicates that wave capture does not occur here because, as suggested in SMPZ07 wave packets move through the strong deformation of the jet-exit region sufficiently quickly that long time asymptotic behavior (wave capture) is not achieved.

The dependence of wave amplitude on the jet strength, and thus the Rossby number, is also examined through distant-dipole experiments. Here, the localized jets emerge and amplify due to interactions between cyclones and anticyclones that are initially separated by a large distance, and subsequently approach each other forming a jet in between. The amplitude of stationary gravity waves from these simulations increases approximately with the square of the Rossby number when a 90-km grid spacing is used, but the rate of increase with Rossby number is noticeably larger when a smaller grid spacing is used. The resolution sensitivity is likely because smaller scale waves with stronger amplitude appear in the leading edge of the wave front in the higher resolution simulation.

Our study, as an extension of Snyder et al. (2007), documents inertia-gravity waves appearing in the exit region of localized jet within vortex dipoles. We emphasize the role of jets on wave generation, propagation, and wave characteristics. However, a few important questions still remain: (1) What precisely is source mechanism of the gravity waves from the jets? (2) What determines the flow features beyond QG dynamics (such as the vertical motion couplet discussed in SMPZ07) other than the gravity waves? (3) How does flow imbalance influence wave generation? (4) What is the effect of the gravity waves on the balanced flow? These are questions remain to be addressed.

3. A LINEAR MODEL AND LINEAR RESPONSES FROM PRESCRIBED FORCING IN THE JET-DIPOLES

The localized jet within the vortex dipole is suggested in the previous section to play important roles on both wave generation and propagation. This issue is further investigated using a linear model in this section. This linear model was formulated by Plougonven and Zhang (2007) (refer as PZ07 in this section), as a complement and extension to the hypothesis of generalized balance adjustment. Nevertheless, PZ07 did not consider the numerical implementation of the linear model. In this section, a numerical model based on PZ07 is developed and tested against some known gravity wave solutions. The basic formulation of the linear model is discussed first, following the argument in PZ07. Instead of solving the stationary wave solution, an initial value approach is employed to find forced steady state wave responses. Using this linear model as a basic tool, wave response to some prescribed Gaussian shape forcing in the dipole winds is discussed.

3.1 Basic formulation of the linear model

The primitive equation set in the inviscid, adiabatic and incompressible fluid on the *f* plane is:

$$\begin{aligned} &\partial_t u + \vec{U}\nabla u + w u_z = f \cdot v - \partial_x \Phi \\ &\partial_t v + \vec{U}\nabla v + w v_z = -f \cdot u - \partial_y \Phi \\ &\partial_t \theta + \vec{U}\nabla \theta + w\theta_z + w\partial_z \overline{\Theta} = 0 \\ &\Phi_z = \frac{g}{\overline{\Theta}}\theta, \partial_x u + \partial_y v + \partial_z w = 0 \end{aligned} \quad . \tag{3.1}$$

Here, $\overrightarrow{U}$ =(u, v) are horizontal winds, w is the vertical velocity, Φ is geopotential height, θ is potential temperature, $\overline{\Theta}$ is the reference potential temperature, g is the gravity constant, and ∂ denote partial derivatives with respect to time t or space (x, y, z). Suppose all these fields can be decomposed into background wind and small amplitude perturbation fields, $u = u_B + u'$, $v = v_B + v'$, $w = w_B + w'$, $\theta = \theta_B + \theta'$, and $\Phi = \Phi_B + \Phi'$. It is also assumed that the background fields are one magnitude larger than the disturbance fields. The linearized equation can be written as,

$$
\begin{aligned}
&\partial_t u' + (\overrightarrow{U_B} + \overrightarrow{U'})\nabla u' + \overrightarrow{U'}\nabla u_B - (w_B + w')\partial_z u' + w'\partial_z u_B - f \cdot v' + \partial_x \Phi' = F_u \\
&\partial_t v' + (\overrightarrow{U_B} + \overrightarrow{U'})\nabla v' + \overrightarrow{U'}\nabla v_B - (w_B + w')\partial_z v' + w'\partial_z v_B + f \cdot u' + \partial_y \Phi' = F_v \\
&\partial_z \Phi' = \frac{g}{\overline{\Theta}}\theta' \\
&\partial_x u' + \partial_y v' + \partial_z w' = 0 \\
&\partial_t \theta' + (\overrightarrow{U_B} + \overrightarrow{U'})\nabla \theta' + \overrightarrow{U'}\nabla \theta_B + w'\frac{\partial \overline{\Theta}}{\partial z} = F_\theta
\end{aligned}
\quad , \qquad (3.2)
$$

where,

$$
\begin{aligned}
F_u &= -(\partial_t + \overrightarrow{U_B}\nabla + w_B\partial_z)u_B + f \cdot v_B - \partial_x \Phi_B \\
F_v &= -(\partial_t + \overrightarrow{U_B}\nabla + w_B\partial_z)v_B - f \cdot u_B - \partial_y \Phi_B \\
F_\theta &= -(\partial_t + \overrightarrow{U_B}\nabla + w_B\partial_z)\theta_B - w_B\partial_z \overline{\Theta}
\end{aligned}
\quad , \qquad (3.3)
$$

Taking (∂_x the u momentum equation) + (∂_y the v momentum equation) gives perturbation equation of the horizontal divergence δ'. Similarly, Taking (∂_x the v momentum equation) - (∂_y the u momentum equation) gives perturbation equation of relative vertical vorticity ς'.

$$\partial_t \delta' + \overline{\vec{U}_B}\nabla\delta' + \left[\vec{u}'\nabla\delta_B + \vec{u}'\nabla\delta'\right] + \left[w_x' U_{Bz} + w_y' V_{Bz} + w_{Bx} u_z' + w_{By} v_z' + w_x' u_z' + w_y' v_z'\right]$$
$$\left[-2J(u_B, v') - 2J(u', v_B) - 2J(u', v')\right] + \left[\delta'^2 + 2\delta_B\delta'\right] - f\cdot\zeta' + \Delta\Phi' = F_\delta$$
$$\partial_t \zeta' + \overline{\vec{U}_B}\nabla\zeta' + \left[\vec{u}'\nabla\zeta' + \vec{u}'\nabla\zeta_B + w_x' V_{Bz} - w_y' U_{Bz} + w_{Bx} v_z' - w_{By} u_z' + w_x' v_z' - w_y' u_z' + \zeta'\cdot\delta'\right]$$
$$+ f\cdot\delta' = F_\zeta \quad , \tag{3.4}$$

Here, F_δ and F_ζ are large scale forcing. They are related to F_u and F_v through

$$F_\delta = \partial_x F_u + \partial_y F_v$$
$$F_\zeta = \partial_x F_v - \partial_y F_u \quad , \tag{3.5}$$

The linearization of the full primitive equation set slightly differs from that in Plougonven and Zhang (2007), who performed scale analysis on the derived divergence equation and vorticity equation. They made an assumption that the primary state (u_B, v_B, w_B, θ_B, Φ_B) evolves on the time and spatial scales much larger than those of the disturbance fields. The primary flow is essentially balanced (denoted by a bar) containing at most a minimal amount of fast gravity waves. Note that the basic state, primary flow and large scale flow are exchangeable in this section since they all refer to the background state that is free from gravity waves. A complete set of the disturbance fields are thus governed by (3.2), or (3.2) with the first two equations replaced by (3.4). The latter is the governing equation set of a linear model in the divergence-vorticity form.

The divergence-vorticity form of the primitive equation set has been widely adopted for simulations of global circulations. But this form is rarely seen in mesoscale models because inverting winds from divergence and vorticity adds considerable computational cost if multiple vertical levels are used. In practice, we may neglect all

shear terms in Eqn. (3.4). This is justified if one considers the WKB (Wentzel-Kramers-Brillouin) approximation, on which the commonly used gravity wave dispersion relation Eqn. (2.5) is derived. In that sense, the linear model described is close to a ray tracing model in the physical space (x, y, z).

Based on the scaling argument, PZ07 wrote the forcing terms F_δ and F_ζ as,

$$\begin{aligned} F_\delta &= -(\partial_t + \overrightarrow{U_B}\nabla)\delta_B + f\varsigma_B - \Delta\overline{\Phi} + 2J(u_B, v_B) = -(\partial_t + \overrightarrow{U_B}\nabla)\delta_B + \Delta NBE \\ F_\varsigma &= -(\partial_t + \overrightarrow{U_B}\nabla)\varsigma_B - f\delta_B \end{aligned}, \tag{3.6}$$

where $\Delta NBE = f\varsigma_B - \nabla^2\overline{\Phi}_B + 2J(u_B, v_B)$, and $J(u_B, v_B)$ is the Jacobean of the background horizontal winds.

All the forcing terms should be diagnosed from large scale flow with a minimal amount of gravity wave activities. Nevertheless, the separation of background state from wave motions has not been discussed in PZ07. This issue, along with physical interpretation of F_δ, F_ς and F_θ in the dipole wind will be discussed later.

In principle, a wave operator in terms of a single equation of the vertical velocity can be obtained by eliminating all other variables. Denote an implicit wave operator as $L(w')$; the forcing terms F_δ, F_θ and F_ζ can be combined:

$$L(w') = G_\delta + G_\varsigma + G_\theta\,, \tag{3.7}$$

where,

$$\begin{aligned} G_\delta &= -(\partial_t + \overrightarrow{U_B}\nabla)\frac{\partial F_\delta}{\partial z} \\ G_\varsigma &= -f\frac{\partial F_\varsigma}{\partial z} \\ G_\delta &= \frac{g}{\Theta}\Delta F_\theta \end{aligned}, \tag{3.8}$$

Here, we follow the usual procedure of deriving *w'* equation in a constant flow. That is to say, take the vertical derivative of the disturbance divergence equation and its Lagrangian, the vertical derivative of the vorticity equation and Laplacian of the thermodynamic equation, and sum over all these three. As we discussed later, these G's terms form may provide some physical insight and facilitate comparisons of magnitude of the three forcing terms and their individual contribution on steady state solution. G_δ, G_θ and G_ζ are derived from F_δ, F_ζ and F_θ and will be referred as the *equivalent forcing*. Cancellation among the forcing terms is readily available once these equivalent forcing is calculated. In fact, in a background wind that only varies in the vertical, explicit form of *L(w')* have been discussed by several authors (Yamanaka and Tanaka 1984, Lin 1994, Inverarity and Shutts 2000) in terms of the general vertical structure equation of the vertical velocity. When background winds vary in all direction, many cross derivative terms may appear in the wave operator. This adds on great complexity and makes any further mathematical analysis intractable. Gravity wave modes in the operator *L* are more evident if both the horizontal and vertical shear terms are temporarily neglected (e.g., in a homogeneous wind environment). Plougonven and Zhang (2007) showed that a single equation of the vertical velocity, after eliminating other variables and neglecting cross derivatives (as if in a rest flow), can be written as:

$$\left[(D_\gamma^2 + f^2)\partial_{zz} + N^2\Delta_H\right]w' = -D_\gamma\partial_z\Delta NBE + f\partial_z A_{1,\varsigma} - \frac{g}{\theta}\Delta A_{0,\theta} \ , \tag{3.9}$$

with $A_{1,\varsigma} = \partial_t\overline{\varsigma} + \overline{\vec{u}}\cdot\nabla\overline{\varsigma} + f\overline{\delta}$, $A_{1,\theta} = \partial_t\overline{\theta} + \vec{u}\cdot\nabla\overline{\theta} + \overline{w}\cdot\partial_z\overline{\theta}$, $D_\gamma = \partial_t + \overline{\vec{u}}\cdot\nabla$. ΔNBE, $A_{1,\varsigma}$ and $A_{1,\theta}$ are the first order approximation of the F_δ, F_θ and F_ζ based on the scaling

argument presented in PZ07. The bar terms are also background flow, the same as those denoted by a subscript B. The operator on the left hand side thus reduces to a simple dispersion relation in which gravity wave modes are implied. The forcing on the right hand side of the linear wave equation consists of three parts, i.e., contributions from the Lagrangian derivative of the vertical gradient of ΔNBE, the vertical derivative of the Lagrangian of relative vorticity and the Laplacian of the Lagrangian derivative of potential temperature.

3.2 Numerical model and its verification

In the following, numerical method for the linearized equation set is introduced. This equation set is solved as a nonhydrostatic, compressible, Boussinesq linear model in a divergence-vorticity form. It uses the split-explicit time splitting technique. The 3rd order Runge Kunta scheme is adopted for the large time step; the small time step is the same as that proposed in Skamarock and Klemp (1992). Rigid top and bottom boundary condition and simple outflow lateral boundary condition are applied to a rectangle domain. Two simple test cases are also discussed in the following.

a. Model numerics

Implementation of a hydrostatic linear system is straightforward; however, a simple verification suggests that it underestimates gravity wave amplitude. In practice, hydrostatic and incompressible assumptions may all be relaxed. Instead of integrating hydrostatic system, we chose to integrate the nonhydrostatic, compressible system, in which hydrostatic and incompressible equations are replaced by,

$$(\partial_t + \overrightarrow{U_B}\nabla + w_B\partial_z)w' + \left[\overrightarrow{U'}\nabla(w_B + w') + w'\partial_z(w_B + w')\right]$$
$$+\left[(\partial_t + \overrightarrow{U_B}\nabla + w_B\partial_z)w_B + \Phi_{Bz} - \frac{g}{\Theta}\theta_B\right] = -\Phi'_z + \frac{g}{\Theta}\theta'$$
$$(\partial_t + \overrightarrow{U_B}\nabla + w_B\partial_z)\Phi' + \left[\overrightarrow{U'}\nabla(\Phi_B + \Phi') + w'\partial_z(\Phi_B + \Phi')\right]$$
$$+\left[(\partial_t + \overrightarrow{U_B}\nabla + w_B\partial_z)\Phi_B + C_s^2(\partial_x u_B + \partial_y v_B + \partial_z w_B)\right] = -C_s^2(\partial_x u' + \partial_y v' + \partial_z w') \quad . \quad (3.10)$$

Note that the above equations restore to hydrostatic balance and incompressible flow if the left hand side of the equations are ignored. In practice, many shear terms may be dropped to reduce computational burden and the terms in the bracket can also be dropped since the basic flow (indicated by subscript B) is presumably hydrostatic and incompressible. The resulting nonhydrostatic system contains different modes that span a broad scale. For example, it may include fast acoustic modes, horizontally propagating lamb waves, gravity wave modes, and slow modes such as Rossby waves. In numerical weather prediction (NWP) models, fast acoustic modes are usually considered physically insignificant. However, they lead to strong constraints on the time stepping, which severely limits computational efficiency of NWP models. There are generally two approaches to improve numerical efficiency. One approach is to adopt a time splitting method, while another approach is to use a semi-explicit method. The split-explicit scheme is one type of time splitting scheme that achieves efficiency by separating terms responsible for fast modes and slow modes, and integrating them separately in either small or large steps. The semi-explicit, on the other hand, involves a computationally expensive task of solving 3D elliptic type equations.

Our divergence-vorticity linear model adopts the popular split-explicit integration scheme that was first introduced by Klemp and Wilhelmson (1978), further improved by Skamarock and Klemp (1992), and summarized by Durran (1999). This scheme is highly efficient for nonhydrostatic and compressible fluids. The key of the KW split-explicit scheme is that it is able to control fast acoustic modes when a large time step is used, and thus maintains numerical stability. In the nonhydrostatic and compressible fluid, Klemp and Wilhelmson (1978) identified that pressure gradient forces in the momentum equations and 3D divergence in the pressure equation are responsible for fast propagating acoustic modes. These terms, in their split-explicit method, are integrated in small time steps using the weighted forward and backward scheme, while advection terms are integrated on large time steps.

Three schemes are commonly used for large time step integration in the current NWP models: the leapfrog scheme, the Runge Kunta scheme of the 2nd order (RK2) and the Runge Kunta scheme of the 3rd order (RK3). Many mesoscale models developed before 2000's adopted the leapfrog scheme, for example, MM5, ARPS, COAMPS etc. Both RK2 and RK3 schemes are implemented in the Weather Research & Forecasting model (the WRF model). These two schemes have higher-order accuracy compared to the leap frog scheme, but also have the advantage that no additional storage is needed for intermediate results of multiple step integration. The numerical accuracy of RK2 and RK3 schemes was demonstrated by Wicker and Skamarock (1998, 2002). In this work, the RK3 scheme is adopted. The RK3 scheme for a scalar advection equation $\partial_t \Phi = F$ is written as:

$$\begin{aligned}\Phi^{*} &= \Phi^{t} + \Delta t/3 \cdot F(\Phi^{t}) \\ \Phi^{**} &= \Phi^{t} + \Delta t/2 \cdot F(\Phi^{*}) \\ \Phi^{t+\Delta t} &= \Phi^{t} + \Delta t \cdot F(\Phi^{**})\end{aligned} \quad , \qquad (3.11)$$

While large time steps are treated with the RK3 scheme, small time steps can be integrated using the forward backward semi-implicit scheme documented in Durran (1999, 7.82-7.85). The semi-discretized form of the nonhydrostatic, compressible, Boussinesq linear system, with terms on the right hand side integrated on the small time step and terms on the left hand side integrated on the small time step $\Delta\tau$, is written as,

$$\begin{aligned}
&\frac{\delta^{m+1}-\delta^{m}}{\Delta\tau} + \Delta\Phi^{m} = -\overrightarrow{U_B}\nabla\delta^{n} + f\cdot\varsigma^{n} - \gamma\delta^{n} + \alpha S(\delta^{n}) + R_{\delta} + F_{\delta} \\
&\frac{\varsigma^{m+1}-\varsigma^{m}}{\Delta\tau} = -\overrightarrow{U_B}\nabla\varsigma^{n} - f\cdot\delta^{n} - \gamma\varsigma^{n} + \alpha S(\varsigma^{n}) + R_{\varsigma} + F_{\varsigma} \\
&\frac{\theta^{m+1}-\theta^{m}}{\Delta\tau} + w^{m+1}\frac{\partial\overline{\Theta}}{\partial z} = -\overrightarrow{U_B}\nabla\theta^{n} - \gamma\theta^{n} + \alpha S(\theta^{n}) + R_{\theta} + F_{\theta} \\
&\frac{w^{m+1}-w^{m}}{\Delta\tau} + \frac{\partial}{\partial z}(\overline{\Phi}^{m}) - \frac{g}{\theta_0}\theta^{m+1} = -\overrightarrow{U_B}\nabla w^{n} - \gamma w^{n} + \alpha S(w^{n}) \\
&\frac{\Phi^{m+1}-\Phi^{m}}{\Delta\tau} + C_s^2\delta^{m+1} + C_s^2\frac{\partial}{\partial z}(\overline{w}^{m}) = 0
\end{aligned} \quad , \qquad (3.12)$$

where all primes of the perturbation terms have been dropped off, *m* and *n* represents small and large time steps, C_s is the constant sound speed (300 m/s), and R_δ, R_ς and R_θ denote all other shear terms that depends on perturbation winds. Rayleigh type wave absorption layers and numerical diffusion are also included in large time step. γ is the Rayleigh damping coefficient; *S* is a horizontal/vertical diffusion operator that is 4th order accurate in the inner domain and 2nd order accurate near the boundaries with a constant coefficient α. $\overline{w}^{m}$ and $\overline{p}^{m}$ are time averaging operations:

$$\overline{\Phi}^{m} = \frac{(1+\varepsilon)\Phi^{m+1} + (1-\varepsilon)\Phi^{m}}{2}, \text{ and } \overline{w}^{m} = \frac{(1+\varepsilon)w^{m+1} + (1-\varepsilon)w^{m}}{2}$$

ε is the weight coefficient. When ε=0, the forward backward scheme reduces to the trapezoidal scheme; forward biasing is the result of using a small positive ε. Note that the stratification term of θ equation, $w^{m+1}\frac{\partial\overline{\Theta}}{\partial z}$, and the buoyancy term of w equation, $\frac{g}{\theta_0}\theta^{m+1}$, are also brought into small time steps. This was suggested by Skamarock and Klemp (1992) in order to further stabilize gravity wave mode when time step exceeds buoyancy periods (1/*N*). In this system, time step is limited by the Courant number of horizontal advection and horizontal/vertical diffusion. Nonlinear advection of pressure in the pressure-divergence equation, as discussed in Epifanio and Rotunno (2005), is negligible since they are physically insignificant since Mach number (*U*/*Cs*) is usually very small in geophysical applications.

Since only vertical derivatives are approximated by the forward biasing forward backward scheme on each small time step, its vertical discretization is implicit, which results in a simple tridiagonal system over each column of the model grid. An efficient algorithm to solve tridiagonal system given by Durran (1999) is adopted in the linear model. This algorithm amounts to two vertical integrations, thus the computation cost of each small time step is proportional to the total number of grid points.

The Rayleigth damping layer is implemented in all six faces of the model grid unless otherwise specified. The reverse of the coefficient γ gives the damping time

scale within the damping layers. Near the top boundary γ has the form similar to the Rayleigh damper in Durran (1999):

$$\gamma = \gamma_{\max} \cos^2(\frac{z - z_{top}}{H_\gamma}\frac{\pi}{2}), \tag{3.13}$$

where γ_{max} is its maximum damping coefficient, H_γ is the depth of the damping layers. γ is zero everywhere outside the damping layer. This specific form of sponge layers seems has a minimal impact on model results in this study.

All variables are staggered on half levels vertically with the vertical velocity on full levels. The 'A grid' staggering rather than C grid is used for the prognostic variables δ and ζ. The difference between the Arakawa C grid and A grid is that horizontal momentum u and v is treated at half points. However, the vertical vorticity ζ and the horizontal divergence δ is commonly diagnosed directly on full points if C grid is used. In that sense, our system is equivalent to standard C grid system having u and v as prognostic variables.

The vertical staggering requires boundary conditions for w in order to close the tridiagonal system. For simplicity, rigid boundary conditions are used here. Rayleigh damping is adopted to avoid possible wave reflection. At the lateral boundaries, a simply outflow boundary condition are adopted. As an example, zonal wind at the east boundary is approximated by a simple advection,

$$u_{b,j,k}^{t+\Delta t} = u_{b,j,k}^{t} + \frac{\max(u_{b,j,k}^{t}, 0)\cdot\Delta t}{\Delta x}(u_{b,j,k}^{t} - u_{b-1,j,k}^{t}), \tag{3.14}$$

All horizontal differentiations, including pressure gradient and advection, are discretized use the fourth order finite difference scheme. The Laplacian of pressure in the divergence equations, for example, has the finite difference form in x direction:

$$\frac{\partial^2 \Phi}{\partial x^2} = \frac{-(\Phi_{i+2} + \Phi_{i-2})/12 + (\Phi_{i+1} + \Phi_{i-1}) \cdot 4/3 + \Phi_i \cdot 15/6}{\Delta x^2}, \tag{3.15}$$

Advection terms are fourth-order accurate in the inner domain and second order accurate near the boundaries. As an example, the advection of a scalar Ψ by mean wind $\overline{U}$ in one direction has a finite difference form,

$$\overline{U} \frac{\partial \psi}{\partial x} = \overline{U}_i \frac{8 \cdot (\psi_{i+1} + \psi_{i-1}) - (\psi_{i+2} + \psi_{i-2})}{12 \Delta x}, \tag{3.16}$$

b. Test of the linear model

b.1 An initial value problem of hydrostatic gravity wave

The linear model is first tested with evolving inertia-gravity waves in a 2D horizontal channel. This test case was described by Skamarock and Klemp (1994). This initial value problem of hydrostatic wave case helps for code error checking. For simulated gravity waves, it gives an indication of phase error of gravity waves in the numerical solution. The inertia-gravity waves are generated by initial perturbed potential temperature in a horizontal homogeneous environment:

$$\theta(x, z, t = 0) = \Delta\theta_0 \frac{\sin(\pi z / H)}{1 + (x - x_c)^2 / a^2}, \tag{3.17}$$

where $\Delta\theta_0 = 0.01\,\mathrm{K}$ is the amplitude of initial perturbations, H is the channel height. The channel is bounded by rigid walls at the top and bottom. In this simple case, the time dependant solution has an analytic form,

$$\theta(\tilde{x},z,t)=\theta(\tilde{x},z,0)+\Delta\theta_0 a\sin(lz)\times\int_0^{\infty}\frac{k^2N^2}{k^2N^2+l^2f^2}e^{-ak}(\cos\lambda t-1)\cos k\tilde{x}dk\,, \quad (3.18)$$

where $\tilde{x}=x-Ut$, U is the constant background wind. In a test case of hydrostatic gravity wave, a channel of length L = 8000 km is used with other parameters have values Δx = 20 km, Δz = 1 km, a=100 km, U=20 m/s, N=$10^{-2}s^{-1}$, f=$10^{-4}s^{-1}$. The cosine integral in the analytical form of the solution is numerically evaluated using a Matlab routine that adopts the Gauss-Kronrod quadrature method.

Figure 3.1 shows the solutions at 60,000 s from the analytical integral and the RK3 model. The analytic solution (Fig. 3.1 b) is strictly symmetric about the translating initial disturbance. The time step of the RK3 model is 800s with small time step 18. The RK3 model produces very accurate solutions comparing to the analytical solution (Fig. 3.1 c). However, there is still some amplitude and phase error at the leading edge downstream the translating disturbance. This error may relate to model time step, or grid spacing. Overall, the performance of the linear divergence-vorticity model is satisfying.

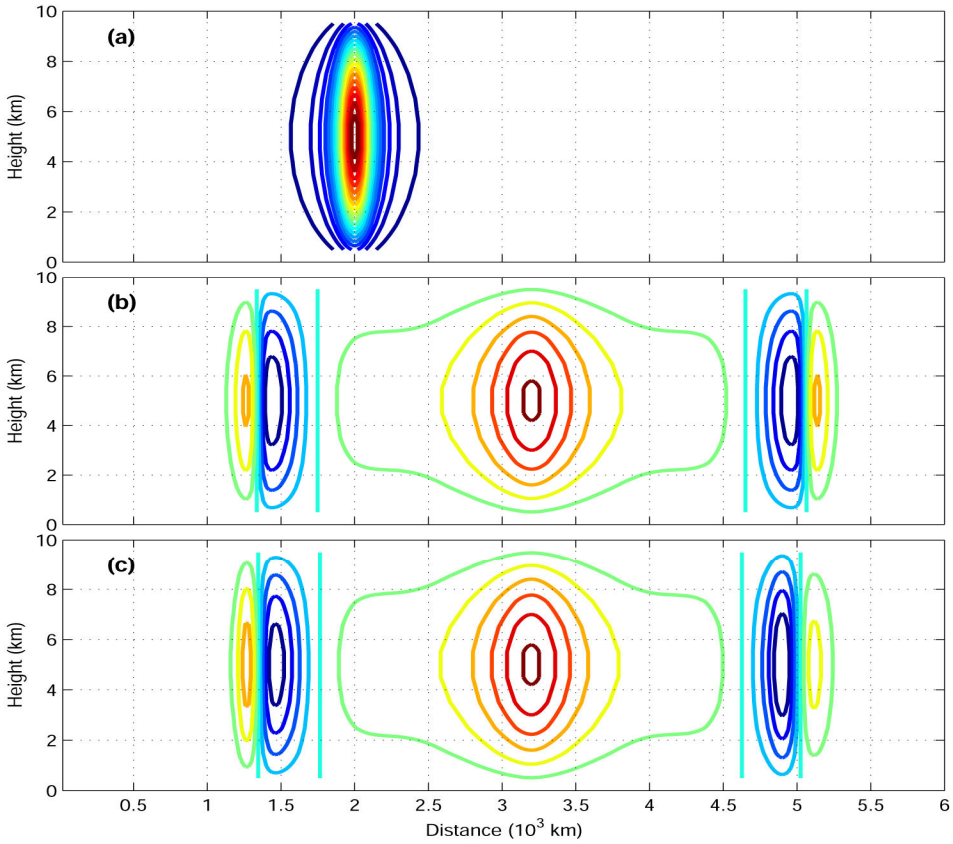

Figure 3.1 (a) The initial θ perturbation and (b) the analytical solution at 60,000 s and (c) the RK3 model solution at 60,000 s. The contour values are from -1 to 1 every $5x10^{-4}$ K.

b.2 Forced wave responses to an elevated mesoscale heating

Another test case for the linear model is the steady state gravity wave response generated by time-invariant elevated heating in a homogeneous environment (Lin 1994). This test is necessary since our linear model will be used to obtain steady state solution. The time independent heating rate is specified as:

$$\dot{\theta}(x,y,z) = \Delta\theta_0 \left(1 + \frac{(x-x_c)^2 + (y-y_c)^2}{R^2}\right)^{-3/2} \exp(-\frac{z}{H}), \qquad (3.19)$$

where $\Delta\theta_0 = 10^{-4} K/s$, ($x_c$, y_c) is the center of heating rate $\dot{\theta}$, R (H) is the characteristic half horizontal (vertical) scale. In this run, the constant background wind is 10 m/s. Top sponge layer is applied at the top 3 km. Other parameters are: dx = 20 km, dz = 200 m, f = $10^{-4}s^{-1}$, N= $10^{-2}s^{-1}$, R=80 km, H=1 km.

Figure 3.2 shows the simulated steady state vertical velocity at 1 km (a) and 6 km (b), and at a vertical plane (c). The inertia-gravity waves propagate both vertically and horizontally. Because of the Coriolis force, an inertial wave train is generated downstream the heating at low levels. This downstream wave train makes the wave pattern more complicated than the mountain wave problem (Holton 2004). The V shape pattern at low levels and upper levels is due to wave propagation effects (Smith 1980). Although these waves are not strictly monochromatic but have multiple harmonic components, a dominant horizontal/vertical wavelength can still be found by measuring the distance between adjacent troughs or peaks. At the same height, the horizontal wavelength λ_h apparently increases away from the heating source (Fig. 3.2. a and b). Even at the location (X=0), λ_h decreases with height. On the other hand, vertical wavelength decreases away from the wave source as X increases. As an example, the estimated vertical wavelength from a vertical profile of the vertical velocity (Fig. 3.2 d) is roughly 6 km directly above the heating, and roughly 5.5 km at X=6 R away from the heating source. Above the wave source, the dominant horizontal wavelength is the scale of wave source, λ_h=2R=160 km. Wave frequency is related to the horizontal/vertical wavelength by the dispersion relation. In this steady state problem, the ground based frequency (ω) is simply zero $\omega = \omega_i + Uk$. Therefore, the intrinsic wave frequency (ω_i) is

determined by Doppler shifting, $\omega_i = -Uk$. This gives an intrinsic frequency $\omega_i = 3.93\, f$. On the other hand, the dispersion relation, $\omega_i^2 = f^2 + N^2 \cdot \lambda_z^2 / \lambda_h^2$ gives the vertical wavelength $\lambda_z = 6.08\ km$, which is close to the estimated vertical wavelength above the wave source at $X=0$.

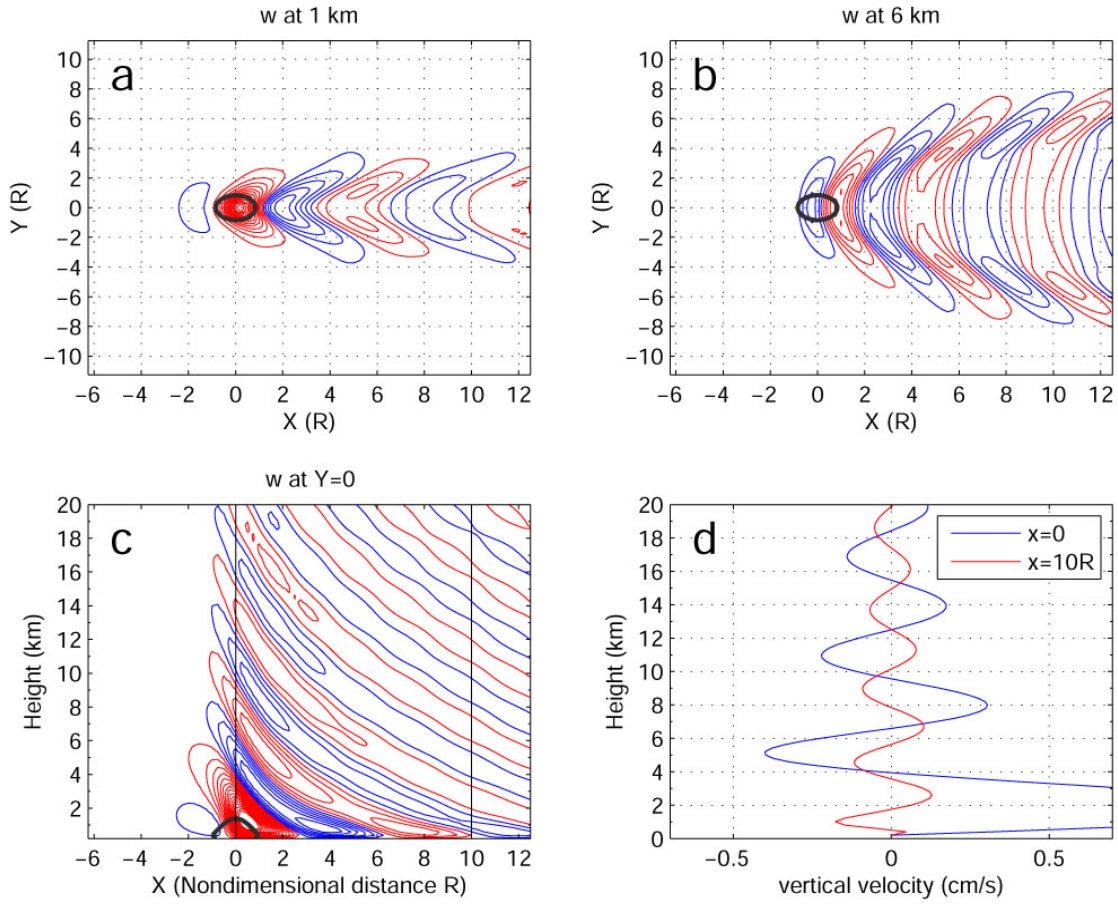

Figure 3.2 Inertia-gravity waves from elevated heating. Panels (a) and (b) show the vertical velocity at 1 km and 6 km. Panel (c) shows the vertical velocity along the vertical cross section. Panel (d) shows a vertical profile of the vertical velocity at the 0 *R* and 10 *R* indicated in (c). Black line in panels a, b and c indicate the heating forcing at the contour 1/e of its maximum.

Wave frequency is also different at different distance downstream the heating source, which is related to the increasing horizontal wavelengths away from the wave source. However, difference in the dominant horizontal wavelength at different distance remains to be determined. This is due to wave propagation effects because of dispersive nature of gravity waves; that is, monochromatic components of gravity waves with different wavelengths transfer energy to different heights and at different rates. A heuristic argument is discussed below.

Given the dispersion $\omega_i^2 = U^2K^2 = f^2 + N^2 \cdot \lambda_z^2 / \lambda_h^2$ in a 2D homogeneous flow, the group velocity (Cg_x, Cg_z) is written as

$$Cg_x = \frac{\partial \Omega}{\partial k} = \frac{\omega_i^2 - f^2}{\omega_i} \cdot \frac{1}{k} = \frac{U^2k^2 - f^2}{-Uk^2}, \text{ and}$$

$$Cg_z = \frac{\partial \Omega}{\partial m} = \frac{1}{\omega_i} \cdot \frac{N^2k^2}{m^3} = -\frac{N^2k}{Um^3}, \tag{3.20}$$

(k, m) are horizontal and vertical wavenumbers. Thus rays are defined by

$$\frac{dx}{dt} = Cg_x, \frac{dz}{dt} = Cg_z, \tag{3.21}$$

The ray equations are completed by considering variations of wave parameters along the ray. In the constant background wind,

$$\frac{dk}{dt} = \Omega_x, \frac{dm}{dt} = \Omega_z, \frac{d\omega}{dt} = \Omega_t, \tag{3.22}$$

The dispersion relation is $\omega = \Omega(x, z, k, m, t) = -Uk$. Ω_x , Ω_z and Ω_t are all zero; hence k, m, ω and group velocities are all constant along rays. Thus rays are simply straight lines. These straight rays are determined by the initial parameters such as initial

wavenumbers, or group velocities. The elevation angle of initial rays is also an indication of the ratio *Cgz/Cgx*. It can be easily verified that rays at a larger horizontal distance have longer λ_h at the same height; rays at higher altitude have larger λ_z at the same distance. Wave components with shorter horizontal wavelengths λ_h and longer vertical wavelengths λ_z have a smaller horizontal group velocity (Cg_x) and a larger vertical group velocity (Cg_z). On the other hand, wave components with larger λ_h and shorter λ_z have a larger Cg_x and smaller Cg_z. Since group velocities indicate the energy propagation, energy of wave components at small horizontal scales is transferred upward at small *X*; only components with larger λ_h can reach larger *X*. Therefore, the phase line (also the tangent of contour line) of wave pattern has smaller horizontal tilting angles in the large *X* region. This heuristic argument quantitatively explains the spatial distribution of wave numbers.

This test of flow over elevated heating demonstrates that the forced linear divergence-vorticity model is able to achieve a steady state solution in a simple flow environment. This test is different from some earlier results (Lin 1994) in that heating forcing in the current setting has a larger horizontal scale and the wave response has a lower frequency. It is probably the simplest problem of steady state wave response due to constant forcing. In the next section, our focus turns to the waves in the jet exit region within vortex dipoles, which is much more complex than the current test case. In the jet-dipole wave problem, background flow is 3D and forcing may include different types forcing. The determination of the wave vertical wavelength is a more complex problem, which is simplified in the current heating wave case.

3.3 Wave responses to prescribed forcing in the dipole flow

Using the linear model, we intend to study wave response to forcing diagnosed from the primitive equation model. However, at this point, both the scales and locations of forcing are unknown, and it is also unclear that how the wave characteristics are determined from these forcing. Therefore, studying wave response of the linear system to known forcing is particularly helpful to understand the characteristics of emitted waves.

Ideally, the prescribed forcing has a localized smooth structure with certain horizontal and vertical scales. Specifying the idealized forcing using an analytic function gives the flexibility of choosing these scales. These scales are important because they may determine the characteristics of forced wave response. As an example, horizontal scale of the forcing and the dispersion relation completely determine the wave characteristics in the problem of steady wave response to elevated heating, as discussed in the previous section. The idealized forcing considered here has the Gaussian shape,

$$F_\delta(x,y,z) = \Delta_0 \exp\left(-\frac{(x-x_c)^2 + (y-y_c)^2 \cdot 9/4}{R_H{}^2} - \frac{(z-z_c)^2}{R_z{}^2}\right), \qquad (3.23)$$

where (x_c, y_c, z_c) denotes the geometric center of the forcing, Δ_0 is the amplitude of the forcing, and the half horizontal scale R_H, and half vertical scale R_z are the other two control parameters. Varying its location (x_c, y_c, z_c), and scales R_H, R_z may help understand the effects of background wind on the properties of forced gravity waves. In most cases, localized forcing is placed at the jet core; this also collocates with the

localized structure of ΔNBE (Fig. 2. 5). The ratio of forcing scale in x direction and in y direction, 3/2, is very close to that from the localized ΔNBE structure.

For the results discussed below, the basic state in the linear model is a subset of the 30-km domain (D2) of the MM5 simulated middle level vortex dipole at the 210th hour, including winds and potential temperature from 3 km to 19 km. The model grid in the linear model has a dimension of 140x145x80 points and horizontal (vertical) grid spacing of 30 km (200 m). In the following discussions, response to prescribed forcing to the divergence equation is studied, but an example is also discussed to show that in one case the vorticity forcing is equivalent to the divergence forcing. Nevertheless, in this section we do not imply which of these forcing is important for jet-dipole waves.

a. Wave response to idealized forcing at different scales

First, idealized Gaussian shape forcing is placed in the jet core but has different horizontal and vertical scales. The control simulation (Cntl) has a forcing with R_x = 225 km and R_z = 1.5 km. For the rest of sensitivity experiments, the 1st letter of their names indicate the forcing is either large (L) or small (S) scales, while the 2nd letter indicates that either horizontal (H) or vertical scales (V) are modified. LH1 and LH2 are two simulations with half horizontal scales two and four times larger compared with Cntl with R_x = 450 km and 900 km. SH1 and SH2 are two experiments with smaller half horizontal scales R_x = 112.5 km and 11.25 km. LV1 and LV2 are two experiments with larger half vertical scales R_z = 4.5 km and R_z = 10.5 km. SV1 has smaller half vertical scale 0.5 km. Table 3.1 summarizes all the eight experiments.

Table 3.1. Eight experiments with different half horizontal and vertical scales, '—' indicates the value is same as the Cntl case.

	Cntl	LH1	LH2	SH1	SH2	SV1	LV1	LV2
R_x (km)	225	450	900	112.5	11.25	—	—	—
R_z (km)	1.5	—	—	—	—	0.5	4.5	10.5

Figures 3.3 and 3.4 display the steady state solution to the forcing prescribed in Table 3.1. Figures 3.3 a and 3.4 a show the steady state solution to the localized forcing in Cntl. The resulting wave response is symmetric about the jet core in the vertical plane. The general wave pattern is similar to the MM5 simulated waves (e.g., Fig. 2.2 a and c) while the wave amplitude is weaker than the MM5 simulated waves. From the horizontal view, a wave packet is clearly identified along the flank of the anticyclone. This wave packet is due to strong horizontal advection of the vortical flow in the anticyclone. The horizontal and vertical wavelength is different in different levels, which is due to wave refraction from wind shear.

In the case of LH1 (Figs. 3.3 b and 3.4 b) and LH2 (Figs. 3.3 c and 3.4 c), the horizontal scale of the forcing increases twice and four times with the same vertical scale. Compared with Cntl, waves in LH1 have larger amplitude, but waves in LH2 have smaller amplitude. Nevertheless, vertical wave patterns do change significantly in LH1 and LH2, although the horizontal wave patterns in LH1 and LH2 are quite similar.

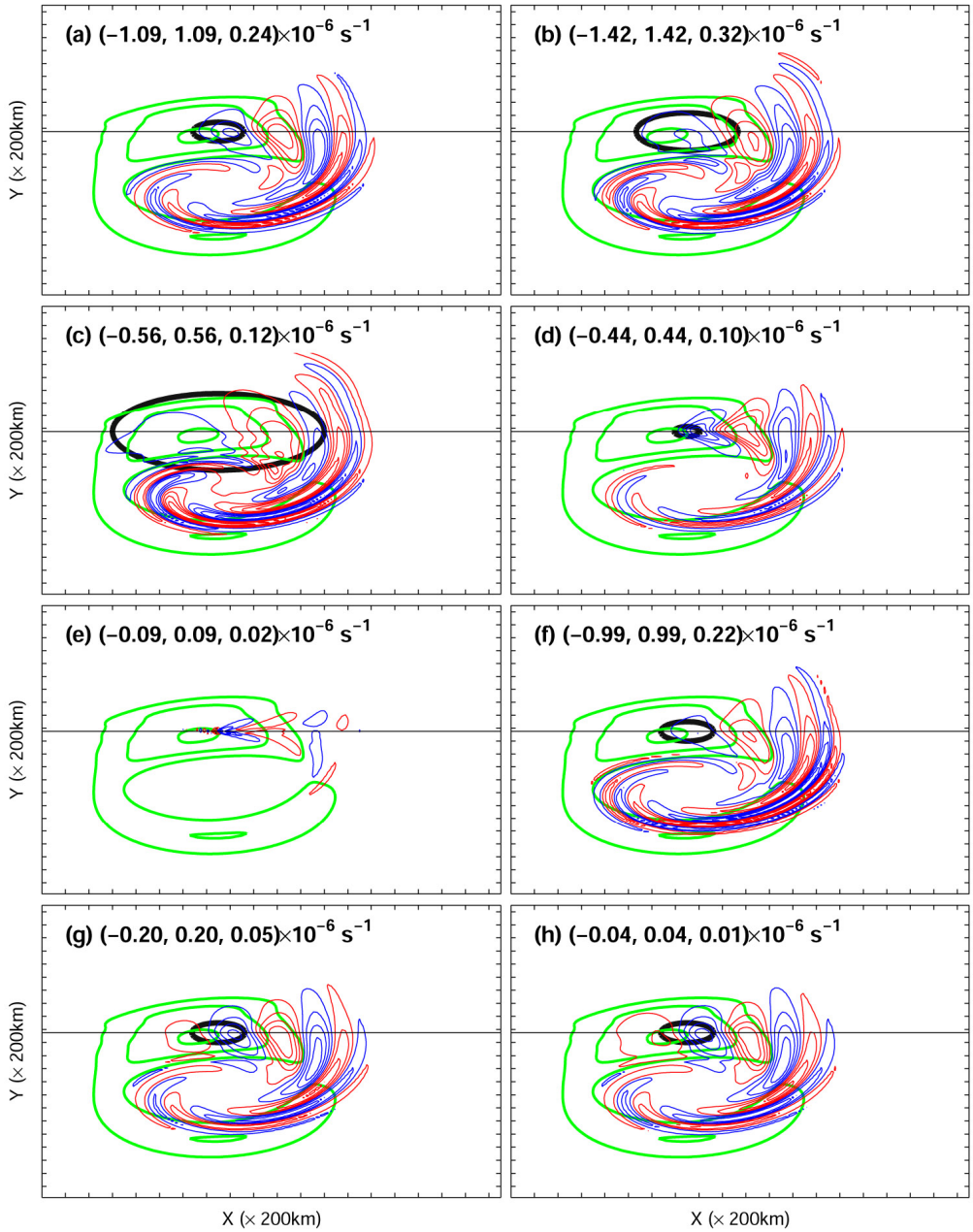

Figure 3.3 Horizontal views of the forcing and responses for Cntl (a), LH1 (b), LH2 (c), SH1 (d), SH2 (e), SV1 (f), LV1 (g) and LV2 (h). In each panel, the horizontal divergence at 13.9 km is plotted in red lines for positive values and in blue lines for negative values. The maximum and minimum values of the responses are also shown in each panel. A single contour level of the forcing term F_δ (1/e of its maximum) is indicated by dark solid lines. Wind speed at 11.5 km is indicated by green lines (ci=5 m/s starting from 20 m/s).

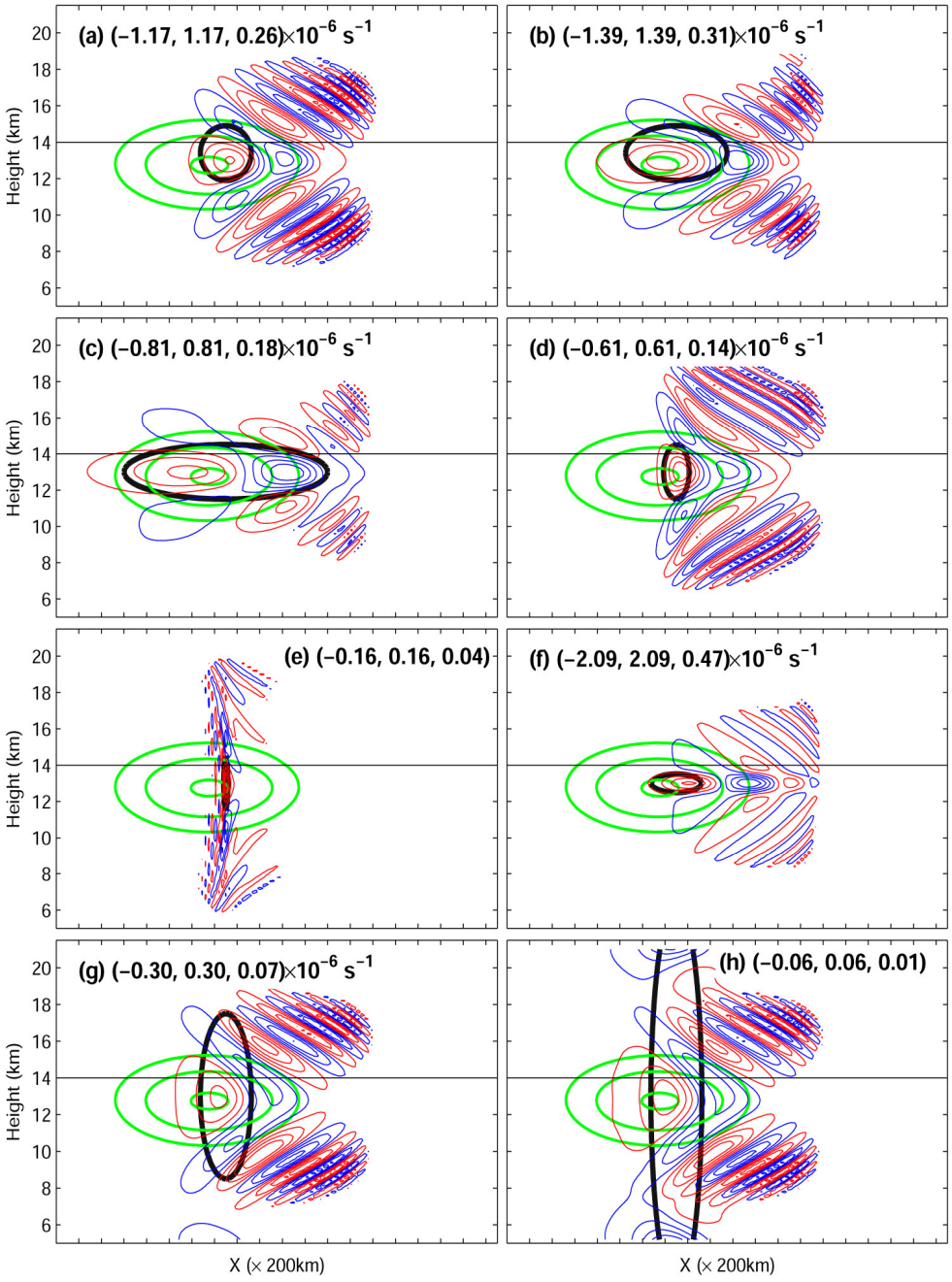

Figure 3.4 Vertical views of the forcing terms and responses along the dipole axis for Cntl (a), LH1 (b), LH2 (c), SH1 (d), SH2 (e), SV1 (f), LV1 (g) and LV2 (h). In each panel, the horizontal divergence along the vertical cross section indicated in Fig 3.3 is plotted in red lines for positive values and in blue lines for negative values. The maximum and minimum values of the response are also shown in each panel. A single contour of the forcing term F_δ (1/e of its maximum) is indicated by dark solid lines. Wind speed at 11.5 km is indicated by green lines (ci=5 m/s starting from 20 m/s).

SH1 (Figs. 3.3d and 3.4d) has the forcing at half horizontal scale. SH1 shows more vertical oriented waves with steeper tilting angles compared with Cntl, which indicates the vertical propagation of waves. SH2 (Figs. 3.3e and 3.4e) is an extreme case since the forcing horizontal scale is 20 times smaller than that in Cntl. Both the forcing and the response are barely resolved at the current horizontal grid spacing of 30 km. Wave responses are concentrated at very small scales, and waves in SH2 can propagate to higher levels (20 km) than waves in other experiments, owing to its large vertical group velocities. In this case, nonhydrostatic effects become important and the Coriolis force is marginally important.

Forcing in SV1 (Figs. 3.3 f and 3.4 f) is only one third of the vertical scale of the value in Cntl. Not surprisingly, the corresponding inertial wave train has smaller aspect ratio (Fig. 3.4 f), and thus the inertial force is more important than the buoyancy force. Nevertheless, the horizontal wave pattern at high levels is not greatly affected. LV1 (Figs. 3.3 g and 3.4 g) and LV2 (Figs. 3.3 h and 3.4 h) have the wave responses to forcing with a vertical scale 3 and 7 times of that in Cntl. The general wave pattern for LV1 and LV2 are quite similar, although the wave amplitude is different in these two cases. The wave absorbing layers become problematic for LV2 near the bottom and top boundaries. From LV1 and LV2, it seems that the vertical scale of the forcing, if similar to or greater than the vertical of the jet flow, is not an important factor to the wave pattern in these two cases.

Overall, both horizontal and vertical wave patterns at high levels are robust features in this dipole flow. The exception in these experiments comes when the forcing

has a large aspect ratio and the nonhydrostatic effect becomes important. This strongly suggests that steady wave responses are tied to the wind environment in addition to the forcing terms. The wind environment refers to horizontal and vertical wind shear in the vortex dipoles, and also the vortical motion of vortices.

b. Response to idealized forcing at different places

Different from the Cntl experiment, localized forcing is moved to the rear side of jet in this section. Three experiments are performed: the forcing is either biased to the anticyclone, or to the cyclone, or in between the vortices. The forcing has a half horizontal and vertical scale of R_H=112.5 km and Rz = 0.75 km, half of those values in Cntl (Figs. 3.3 a and 3.4 a).

Figure 3.5 shows the wave patterns in the three experiments. The most conspicuous difference in these experiments is the formation of horizontal wave patterns due to advection by the vortical flow. When the forcing is biased toward the anticyclone (Fig. 3.5 d), correspondingly the wave pattern is most seen in the anticyclone. It is also true for the forcing biased to the cyclone (Fig. 3.5 f). While the forcing is moved to the midway of the cyclone and the anticyclone (Fig. 3.5 b), banded wave structures appear in both sides, with more part in the anticyclone probably due to strong wind at the flank of the anticyclone.

These experiments demonstrate that, because of horizontal advection of the vortical flow, wave pattern at upper levels can be quite different if the source is located at different regions at the levels of the jet core.

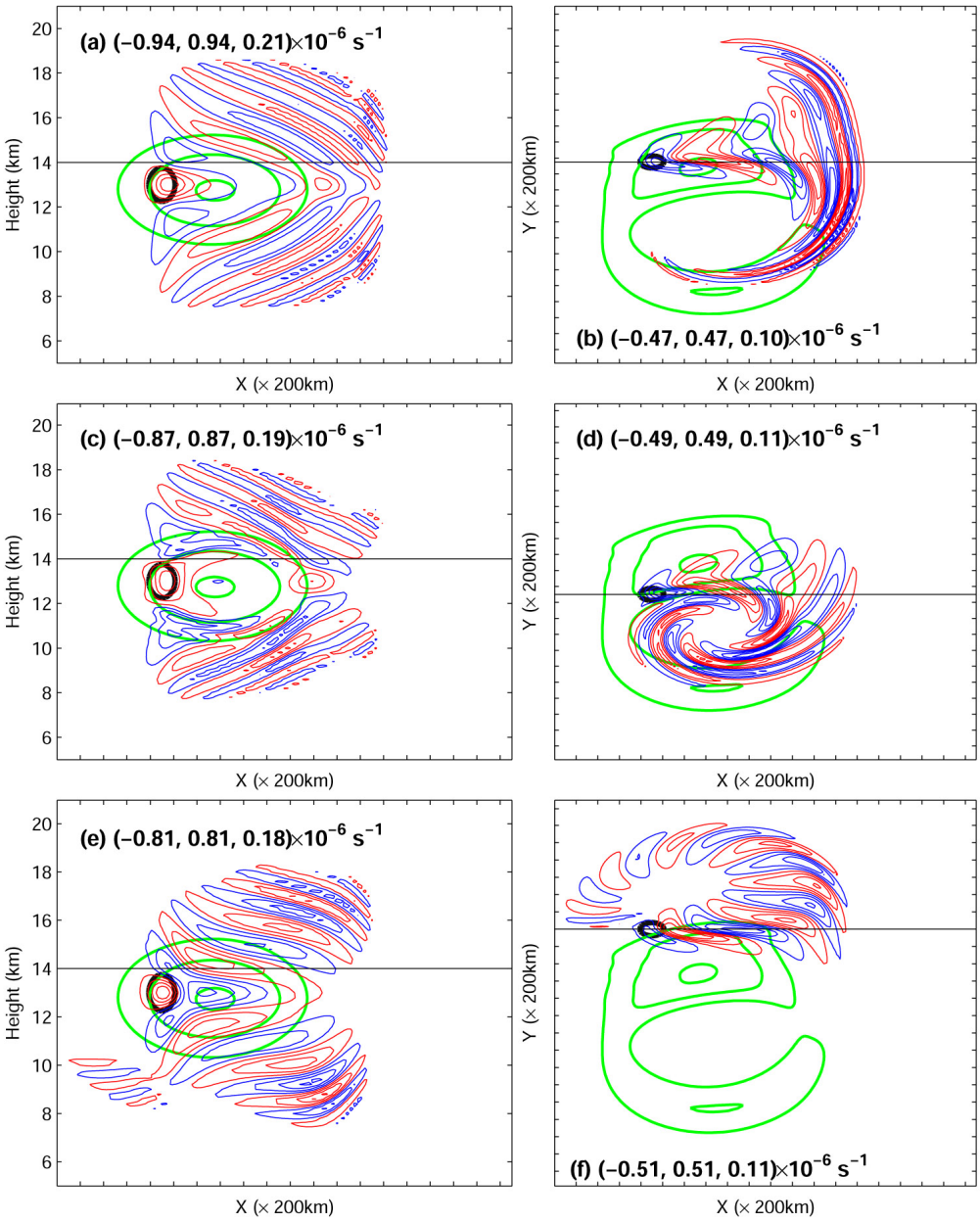

Figure 3.5 Horizontal divergence (red, positive; blue, negative) along the vertical cross section (left column) and at 13.9 km (the right column) for the three cases considered in section 3.3. In each left panel, the vertical cross section is indicated in the corresponding right panel by the gray solid line. The maximum and minimum values of the response are also shown in each panel. Wind speed and forcing is contoured at 20, 25 and 30 m/s.

c. Wave response and ray tracing in a quasi 2D wind environment

As discussed before, the lateral propagation is due to advection by the vortical flow in the vortex dipole, which complicates the wave propagation scenario. In order to further separate the horizontal advection effects due to the vortex flow, a slice of flow field along jet is taken to create a 2D wind environment that only changes in x and z direction. The 2D flow is further expanded in y direction. Although the flow remains 2D, 3D propagation is simulated with the same wave sources as specified in the previous part. These experiments are referred as quasi 2D experiments. It should be noted that the quasi 2D flow environment is not kinematically consistent with the some basic dynamic constraint such as thermal wind balance or geostrophic wind balance.

Figure 3.6 shows the wind speed at 11.5 km and the wind at vertical cross sections. This flow is simple enough to be fitted to an analytical function that is separable in x and z direction:

$$\widetilde{U}(x,z) = U_{\max} \cos\left[\left(x - x_c\right)/D_H\right]^4 \sec\left[\left(z - z_c\right)/D_z\right]^2, \qquad (3.24)$$

where (x_c, z_c) is the center of the jet that has the maximum wind speed U_{max}, and D_h and D_z are horizontal and vertical scales of the 2D wind. D_h = 1814 km and D_z = 3.77 km is found by a simple nonlinear fitting procedure. Fig 3.6 b also shows that the fitted 2D winds are very close to the MM5 simulated winds at the vertical plane.

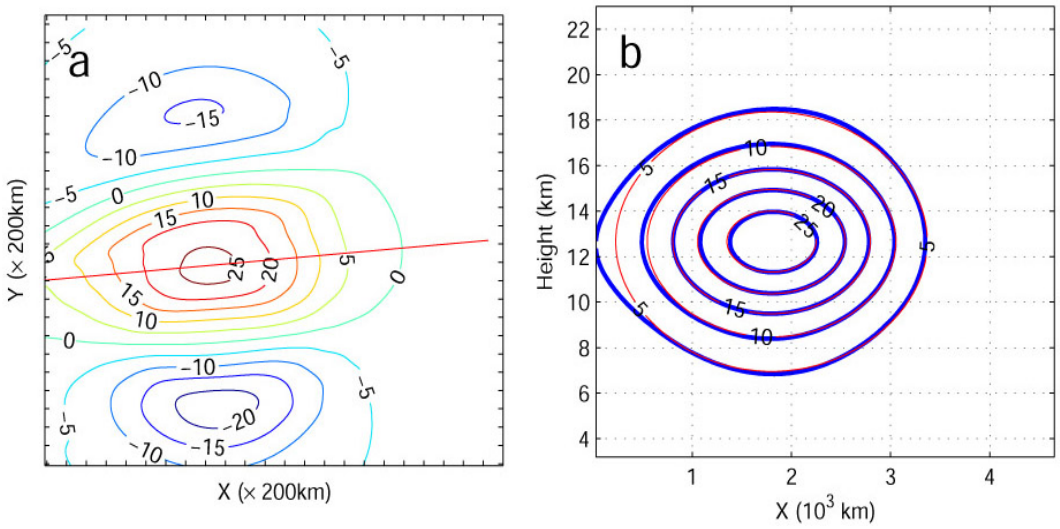

Figure 3.6 Wind speed (a) at 11.5 km and (b) along the vertical cross section indicated by the red solid line in (a). The analytical wind speed (red) is also plotted in (b).

The wave responses from sources at different scales in the linear model are plotted in Figs. 3.7 - 3.9. In general, wave patterns in the horizontal plane are quite different from those in Figs. 3.3-3.4, as expected. Fig. 3.7 shows the horizontal views of wave patterns. It seems that wave response has little y dependence if horizontal scale is sufficiently large (e.g., LH2 Fig. 3.7 c). The horizontal wave patterns at 13 km are similar to those of steady state wave response to elevated heating. Fig. 3.8 shows that wave patterns in the vertical plane are surprisingly similar to those in the simulations in the 3D dipole wind, although the magnitude may be different.

It is also helpful to compare vertical velocities in this quasi-2D wind environment. Fig. 3.9 shows that almost for all cases the vertical velocity has a quadruple pattern and gravity waves are generated downstream, although the forcing term F_δ has only localized monopole structure. The only exception is the SH2 case (Fig. 3.9 e) in which the nonhydrostatic effect dominates and no apparent quadruple pattern is observed. However, the horizontal scale of the forcing in SH2 is barely resolvable by the linear model at the 30 km horizontal resolution. Comparison among Fig. 3.9 a-e suggests that the horizontal scale of the quadruple pattern also increases when the horizontal scale of the forcing increases. Comparison among Figs. 3.9 a, f-h seems to suggest a similar conclusion for the vertical scale dependence; however, the vertical scale does not increase when the forcing scale is 7 times of that (Fig. 3.9 h) in Cntl. These comparisons imply that wave emission depends how effective of forcing is projected into propagating wave modes. A linear analysis will help classify the wave generation scenario in this quasi-2D jet flow and may be considered in the future.

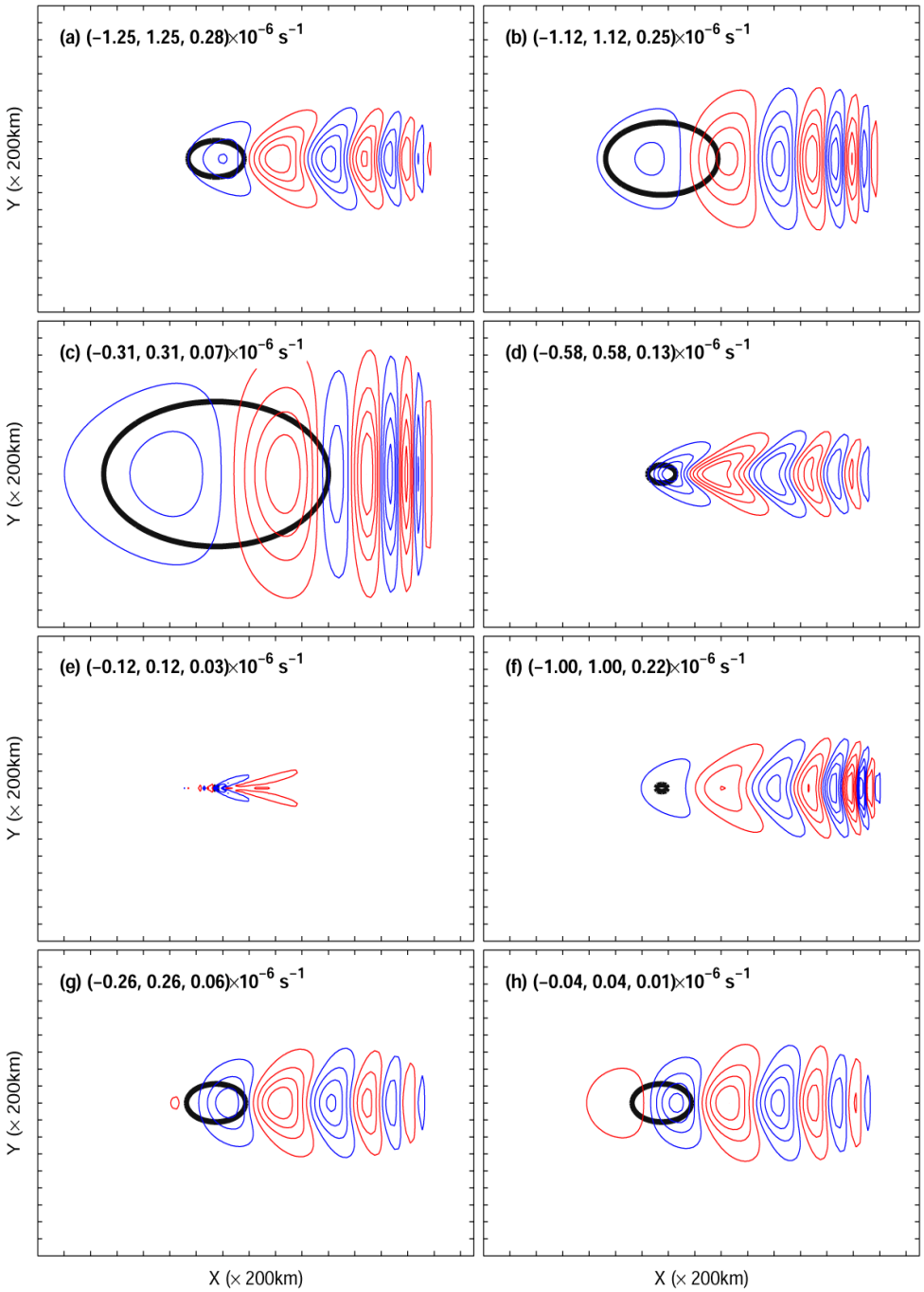

Figure 3.7 The same as Fig. 3.3 except that background wind is quasi-2D as discussed in the text.

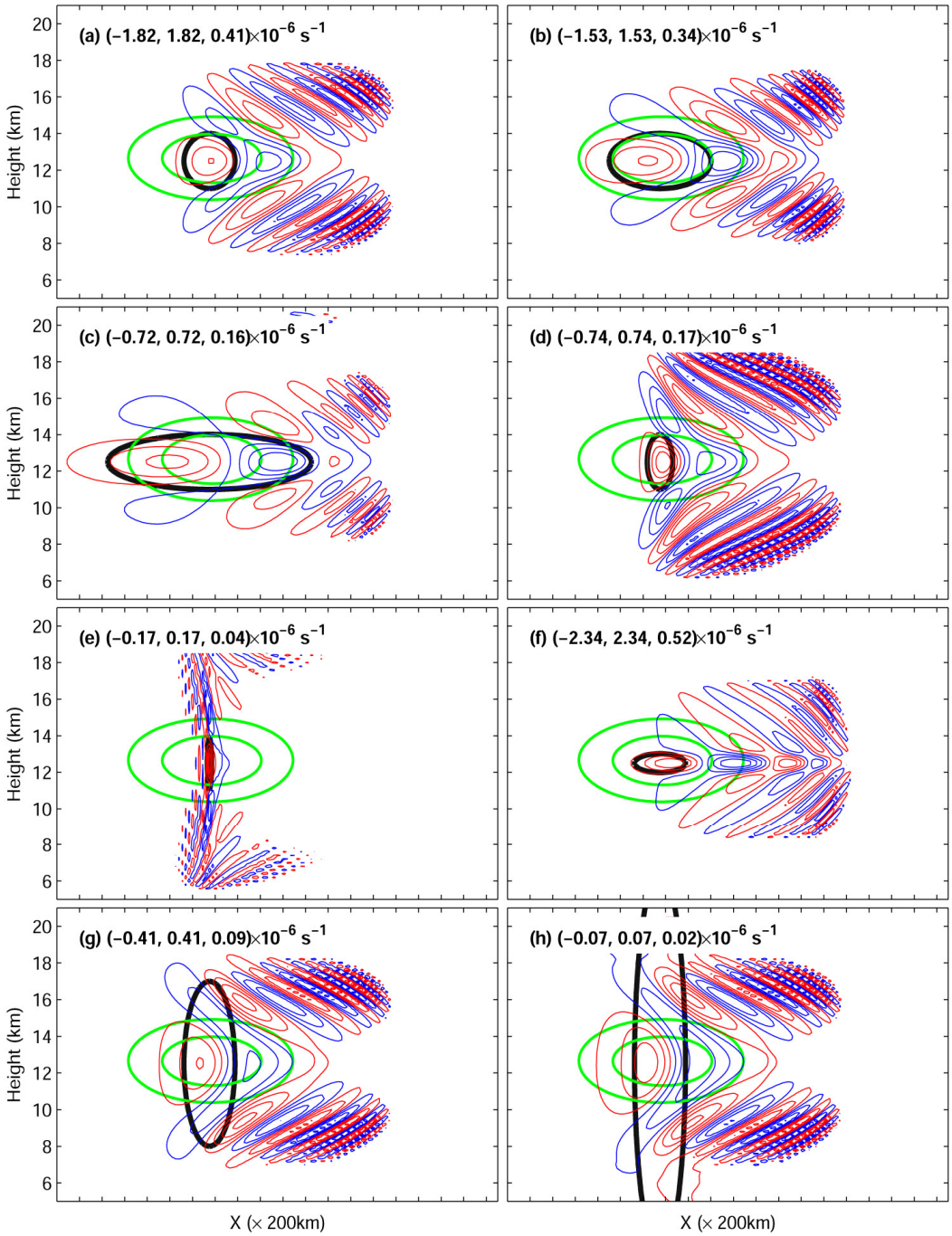

Figure 3.8 The same as Fig. 3.4 except that background wind is quasi-2D as discussed in the text.

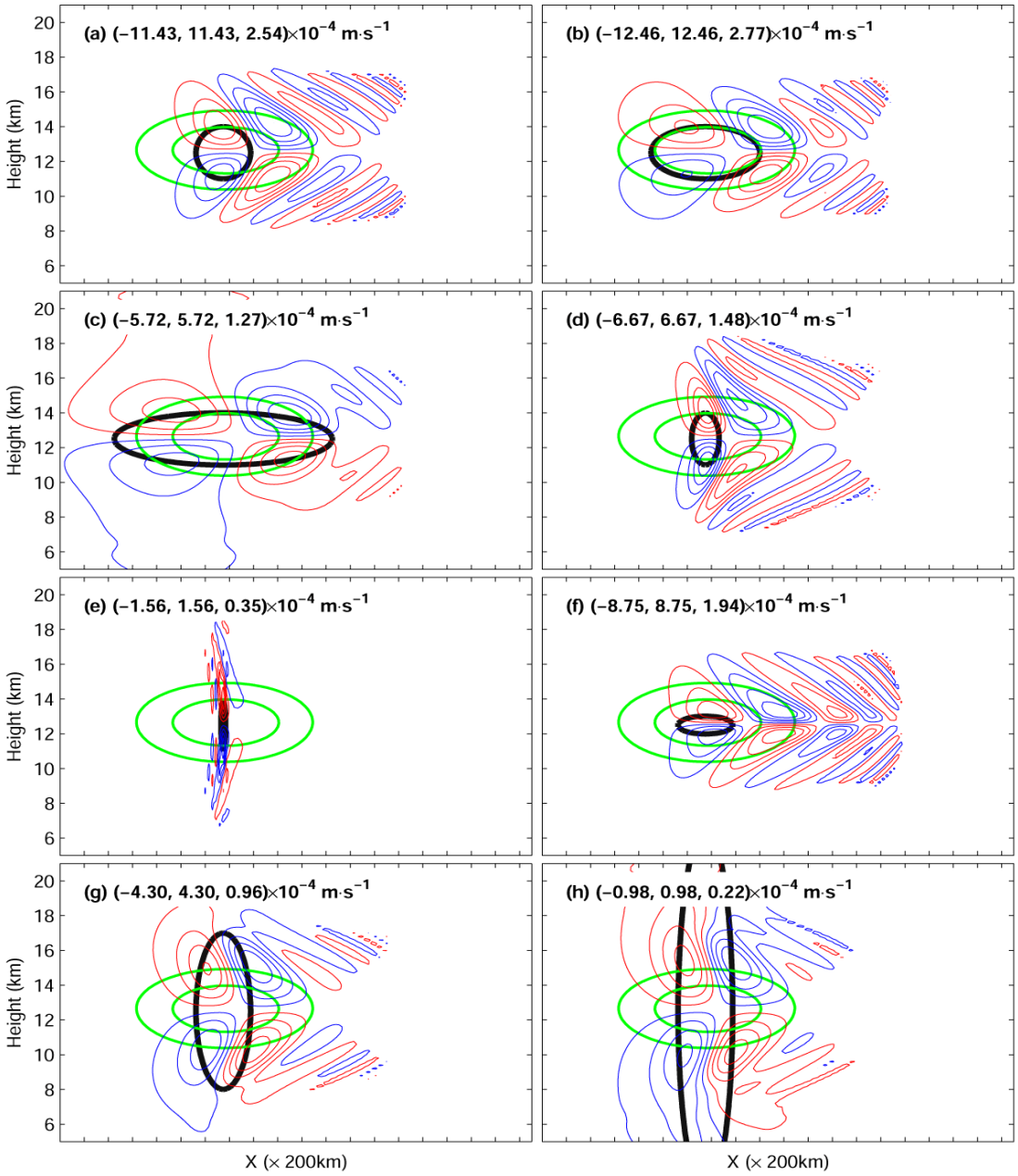

Figure 3.9 The same as Fig. 3.8 except that the vertical velocity is plotted.

Next, ray tracing in a simple 2D wind is considered. The 2D ray tracing equations based on the dispersion $\omega_i^2 = (\omega - Uk)^2 = (f^2m^2 + N^2k^2)/(k^2 + m^2)$ can be written as

$$\frac{dx}{dt} = Cg_x, \frac{dz}{dt} = Cg_z, \frac{dk}{dt} = -k\widetilde{U}_x \text{ and } \frac{dm}{dt} = -m\widetilde{U}_z, \qquad (3.25)$$

where group velocities are $Cg_x = \widetilde{U} + k\frac{N^2 - \omega_i^2}{\omega_i \Delta}$, $Cg_z = m\frac{N^2 - \omega_i^2}{\omega_i \Delta}$ and $\Delta = k^2 + m^2$. This dispersion includes the nonhydrostatic effect; hence it is also suitable for nonhydrostatic gravity waves. Although analytical solution of the ray tracing equations is not easy to find, numerically solving this ODE system is straightforward.

Before solving ray tracing equations numerically, some qualitative analysis of the equation is helpful. Because the *dk/kdt* and *dm/mdt* are proportional to $\widetilde{U}_x$ and $\widetilde{U}_z$ and they are both negative above the jet exit region, both k and m grows with respect to time as long as $\widetilde{U}_x$ and $\widetilde{U}_z$ remain negative. If horizontal and vertical wind shear does not change significantly along the trajectories, this growth is exponential. As a result, wavelengths decrease significantly, and wave packets freeze into the background wind, eventually behaves as passive tracers. This type of behavior of wave packets is very similar to the wave capture discussed in (Plougonven and Snyder 2005, Bühler and McIntyre 2005). As long as the wave packets stay above the jet region with negative horizontal and vertical wind shear, the shrinkage of wavelengths continues unless the following three situations happen: either unsolved subgrid scale processes become important, or wave packets leave the shear region, or critical levels are encountered.

Figure 3.10 shows a ray that is initially located at the jet core with an initial horizontal and vertical wavelength 200 km and 62 km. This ray travels upward with a quickly decreasing vertical wavelength (panel c). The wave packet stops vertical propagation at roughly 4.5 km (panel a) above its origin, where both the intrinsic frequency (panel b) and vertical group velocity (panel d) approach zero. This ray calculation is exact since no wind interpolation needed along the ray as for the GROGRAT model (introduced in Section 2). It is also an example of shear effect on wave propagation. Note that the vertical wavelength of 62 km for this ray is unrealistic. Ray tracing with a much smaller initial vertical wavelength (e.g. 5 km) gives similar results except that this ray reaches a much lower altitude than the ray in Fig. 3.10.

The ray calculation can be repeated to a large amount of rays with a wide range of initial λ_h and λ_z. Figure 3.11 shows the results for rays having initial λ_h ranging from 10 km to 500 km and λ_z from 1km to 100 km. These rays are integrated up to 20 buoyancy periods (~ 2.5 hours). The blue lines are the initial wave intrinsic frequency, which depends on λ_h and λ_z via the dispersion relation. The final wave packet characteristics shown in four panels all fall into two regions: one is the shading region that wave packet can escape the jet, and the other one is the white region that wave packet stay in the jet region. The transition between these two regions is narrow. In the shading region, the wave intrinsic frequency is much higher than the inertial frequency (Fig. 3.11 a), the final height (Fig. 3.11 b) is higher than the vertical scale of the jet (D_z = 3.77 km), final λ_z remain large (Fig. 3.11 c), and the vertical group velocity reaches more than 1 m/s (Fig. 3.11 d).

The above 2D ray tracing analysis gives an exact result of possible distribution of wave spectrums above the jet. Because the wave amplitude equation has not been considered here, the ray solution is incomplete. Nevertheless, ray tracing may potentially help understand the energy spectrum above strong sheared flow such as atmospheric jets. One limitation of the above ray tracing analysis is that it is merely considers a two dimensional jet. The wind shear wave trapping effects are probably over estimated since no horizontal propagation in the cross stream direction is permitted here.

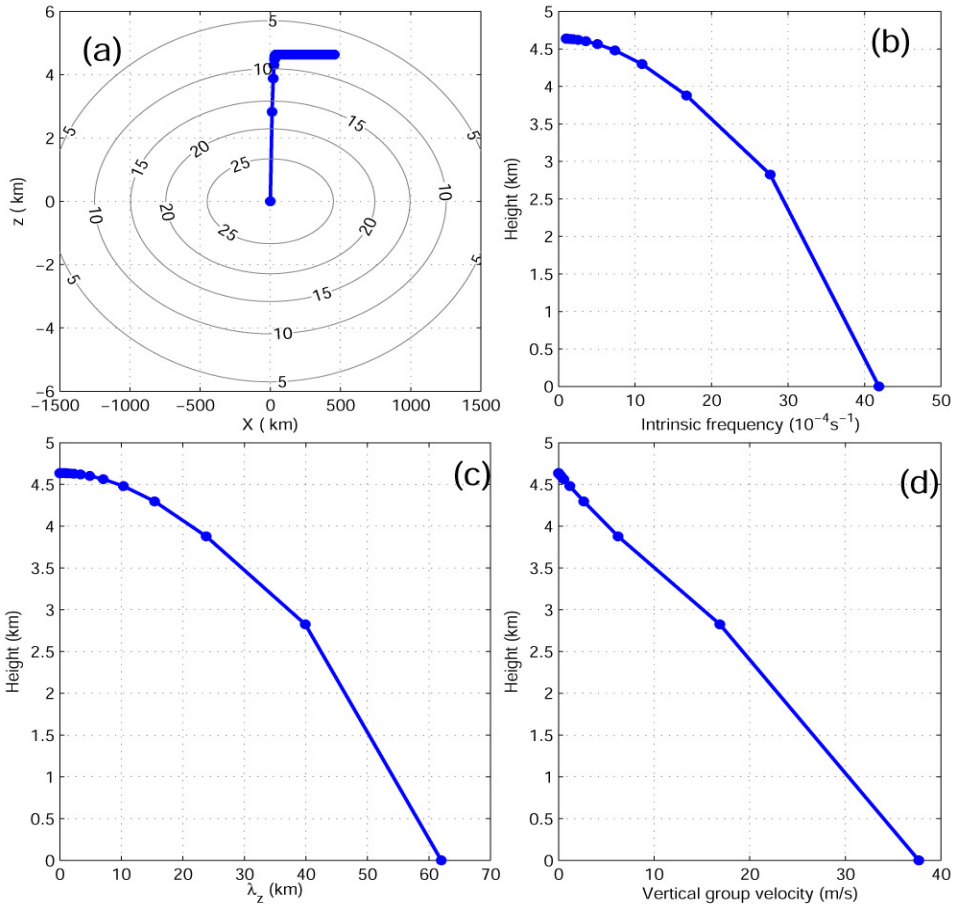

Figure 3.10 A ray with initial horizontal and vertical wavelengths (200 km, 62 km) in the 2D flow.

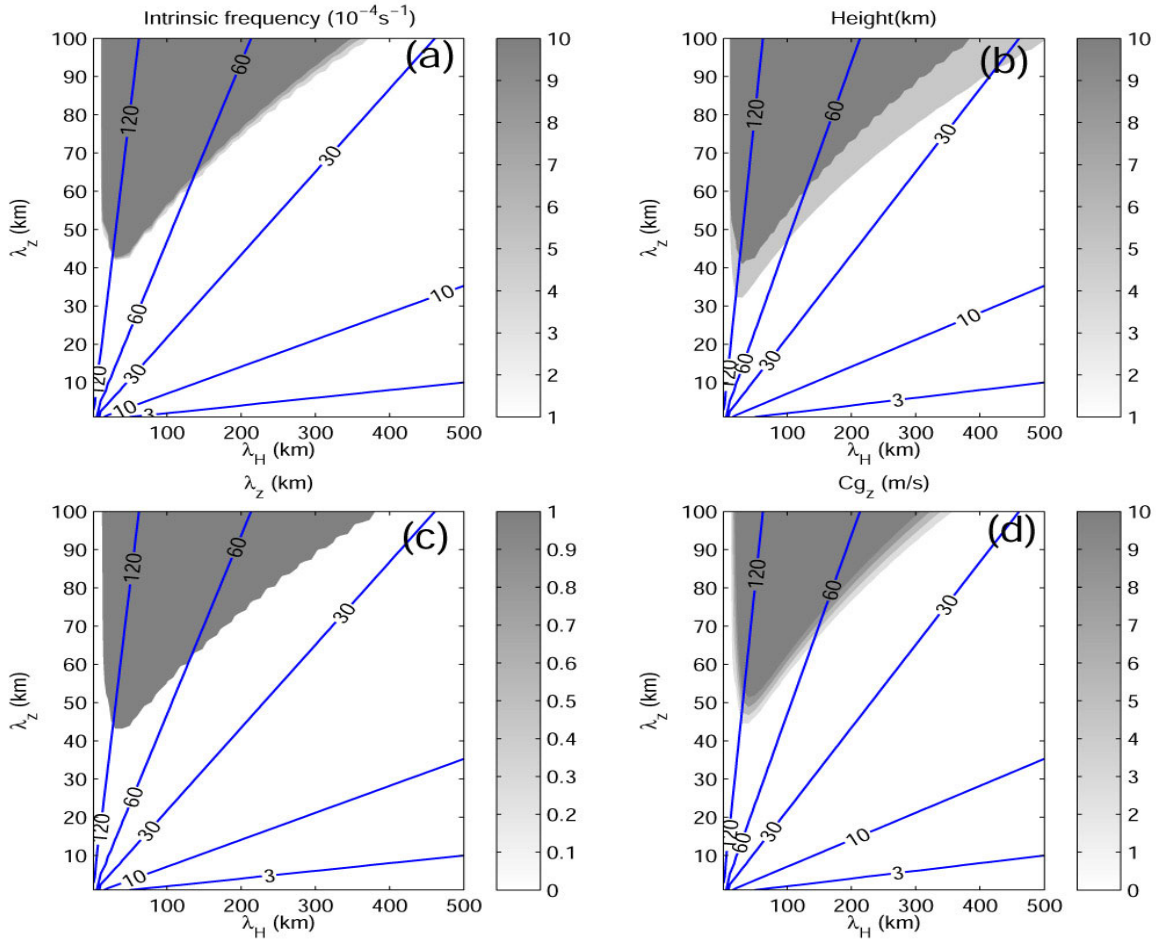

Figure 3.11 The intrinsic frequency (a), ray height (b), vertical wavelength (c) and vertical group velocities (d) of wave packets in a parameter space (λ_h, λ_z) at 20 buoyancy periods. Two regimes are identified in this figure. Panels show the intrinsic frequency with white region indicating the wave frequency close to inertial frequency and light shaded region indicating a propagating wave regime. The blue lines indicate the initial intrinsic frequency with a unit of inertial frequency *f*.

d. An example of wave cancellation due to different wave forcing

As discussed in section (3.1), the wave operator may be written as,

$$L(w') = G_\delta + G_\varsigma + G_\theta \,, \tag{3.7}$$

where L(*w'*) is an implicit wave operator, $G_\delta = (\partial_t + \overrightarrow{U_B}\nabla)\frac{\partial F_\delta}{\partial z}$, $G_\varsigma = f\frac{\partial F_\varsigma}{\partial z}$, and $G_\delta = -\frac{g}{\Theta}\Delta F_\theta$. Provided that the linear assumption is valid, the total response is the sum of individual responses to the forcing F_δ, F_ζ or F_θ. Wave cancellation is highly possible if different forcing cancels, therefore causes the weakening of wave amplitude. Now consider a case with F_δ specified as that in Fig. 3.3a, and $F_\zeta = -\overrightarrow{U_B}\nabla F_\delta / f$, thus $G_\delta + G_\zeta$ =0. This implies that wave response to F_δ and F_ζ is zero.

Figure 3.12 displays F_δ, G_δ, G_ζ and F_ζ, the total forcing $G_\delta + G_\zeta$ and their linear response for a specified F_δ. Note that G_δ and G_ζ have an opposite sign, as expected. Due to numerical errors, $G_\delta + G_\zeta$ is not exactly zero (Fig. 3.12 e) but very small and have a noisy structure with a horizontal scales similar to G_δ or G_ζ. The response (Fig. 3.12 f) still has a wave pattern, but the maximum value of vertical velocities of the response is $1.5\text{x}10^{-5}$ m/s, which is nearly 100 times smaller than the response to F_δ alone (Fig. 3.9 a). This is an example of wave cancellation; that is, although both F_δ and F_ζ may produce wave response with relatively amplitudes but their total is not effective for wave generation.

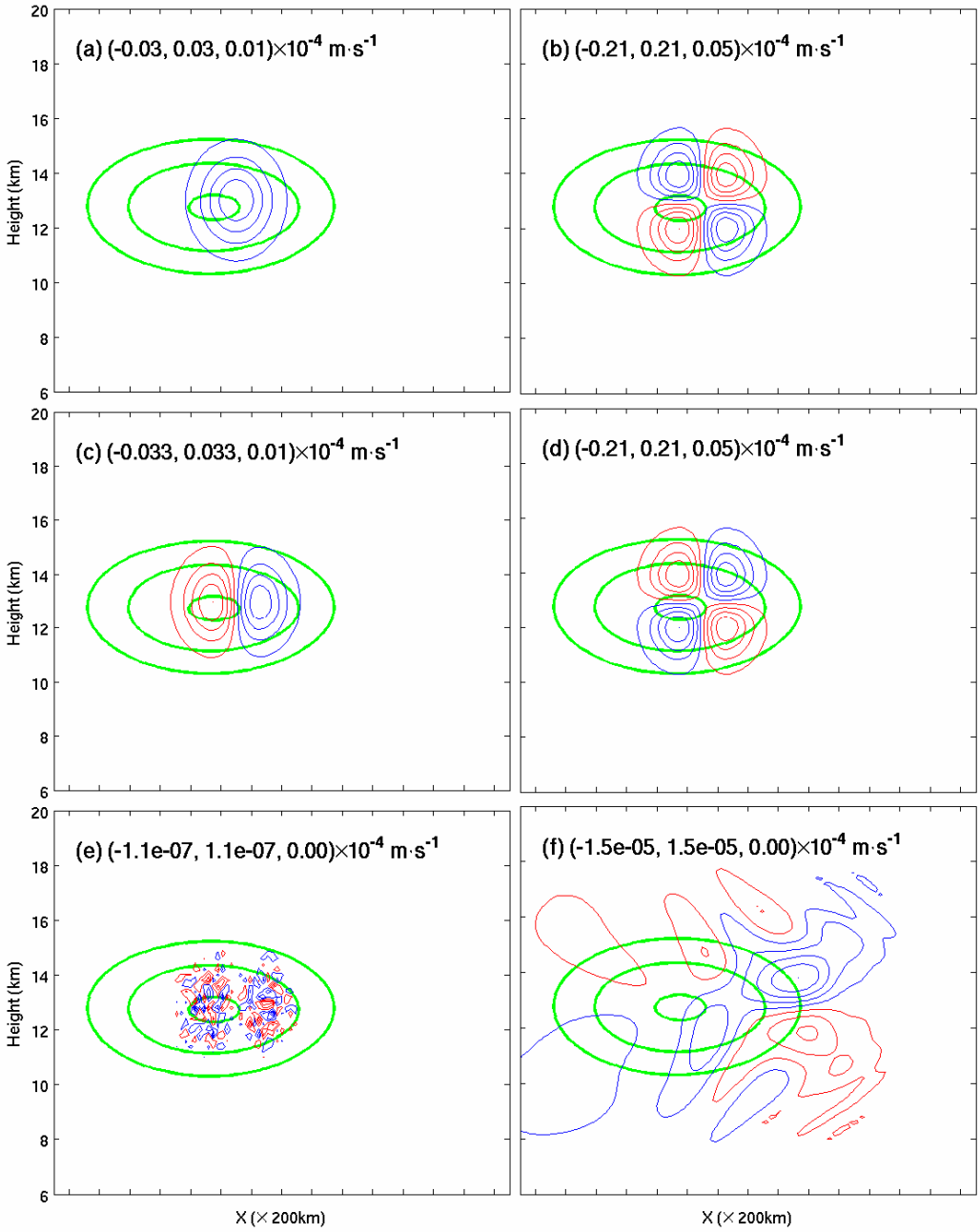

Figure 3.12 F_δ and G_δ are plotted in (a) and (b). F_ζ and G_ζ are plotted in (c) and (d). Total forcing $G_\delta + G_\zeta$ is plotted in (e). Vertical velocity response to $G_\delta + G_\zeta$ is plotted in (f). The plotted domain is smaller than that in Fig. 3.9. The green contour is the wind speed (20, 25 and 30 m/s).

The spatial pattern of F_δ , G_δ and G_ζ is worth careful examination. F_δ has localized Gaussian shape, but G_δ has a quadruple pattern in the jet core. This quadruple pattern is also seen in the response fields upstream of the waves in a few cases (Fig. 3.9 a, b, c, g and h) and even in the MM5 simulation (details discussed in Section 4.2). The origin of this quadruple pattern is related to the way we compute G_δ from F_δ using $G_\delta = -\overrightarrow{U_B}\nabla\frac{\partial F_\delta}{\partial z}$ in the steady flow of the vortex dipole. The spatial derivatives involved in this calculation are a vertical derivative and horizontal advection. The vertical derivative of the Gaussian forcing produces a dipolar pattern in the vertical, while the horizontal advection by the localized jet flow produces a dipolar pattern along the jet flow (or streamlines). These two dipolar patterns result in this quadruple pattern seen in G_δ. This quadruple pattern also appears in the vertical velocity field in the response (Fig. 3.9 a). Downstream the quadruple pattern of G_δ are propagating gravity waves, as discussed in the previous. This case shows how localized jet helps build up the quadruple pattern in the forcing and the response.

e. Summary

A linear WKB type model is documented in this section. Through a series of linear model experiments, wave responses to different idealized forcing are obtained. Results suggest that the wave pattern in the dipole wind environment is a robust feature. When the prescribed forcing is first placed in the jet core region, varying the horizontal and vertical scales of the forcing does not significantly change wave patterns at high levels, but the wavelengths are affected. Although the propagation effect is not separated from the generation effect, these experiments suggest that forcing with different scales

may generate waves of different scales. Experiments with forcing placed in different regions of jet further demonstrate that wave pattern at upper levels can be widely different due to horizontal advection of the rotational flow in the vortex dipole. These experiments also suggest that the scale of the forcing does not monotonically determine the wavelengths at high levels above the jet core. It seems that there is a certain scale on which waves can be more efficiently excited.

The wind shear in the vertical direction and the horizontal direction along the dipole axis is further separated from the horizontal rotational motion. The resulting wave responses in a quasi-2D jet flow show similar wave pattern in the vertical plane along the dipole axis, but horizontal wave pattern is significantly different since cross stream dependence is less evident. This suggests it is possible to simplify the wave emission using a two dimensional framework. The resulting quasi-2D jet flow is fitted to an analytical function. 2D ray tracing in the 2D wind environment suggests there are two parameter regimes: one regime that wave packet can escape the jet, and the other regime that wave packet are trapped in the jet region.

An example of wave cancellation due to different forcing terms is also presented. This example demonstrates the usefulness of the equivalent forcing. It also suggests how localized jet helps build up the quadruple pattern in the equivalent forcing and in the corresponding wave response.

4. LINEAR WAVE RESPONSES FROM A LOCALIZED JET WITHIN THE MID-LEVEL VORTEX DIPOLE

4.1 Introduction

As noted in the introduction section, several hypotheses of wave generation are possibly applicable to wave generation within the vortex dipole. Through scale analysis of primitive equations, Plougonven and Zhang (2007) suggested that ΔNBE, along with tendency residuals in the vorticity and thermodynamic equations may force the generation of gravity waves. The importance of divergence tendency and the nonlinear balance residual in wave generation has been hypothesized by different authors (e.g. Kaplan and Paine 1977). Snyder et al. (1993) and Reeder and Griffins (1996) suggested that gravity waves from front are linear forced response due to the residual tendency terms. Despite differences in interpretation and in the underlying balance, the importance of residual tendency is also proposed in Snyder et al. (2007). However, the separation between balanced flow and gravity waves remains to be an open question. In fact, several authors (e.g. Ford et al. 2000) suggested such a strict balanced flow (sometimes termed slow manifold) do not exist.

The above discussion suggests forcing is likely the key to wave generation, although different authors may not agree on the specific content. On the other hand, responses to the forcing are obtained through appropriate linear dynamics. The linear dynamics (or linear wave operators) are also different in different studies. The linear model proposed in PZ07 and implemented in the previous section includes the

background wind on the left hand side of the linear operator. However, the background wind is not counted in the wave operator in the theory of spontaneous adjustment emission (Ford et al. 2000 and Ford 1994). Because of that, wave propagation effects are not considered in Ford's theory, but are included in the linear model since the linear model uses the background wind (shear) for nonlinear advection. In that sense, the linear model is more appropriate than Ford's theory. This section studies both forcing diagnosis and its linear responses in the dipole-jet environment.

The initial value approach using a linear model has been adopted by several authors to study gravity wave generation in simplified two dimensional flows. In a 2D frontal gravity wave problem, Reeder and Griffith (1996) integrated both a primitive equation model and a semi-geophysical model. Their semi-geophysical model is considered as a balanced model in which no gravity waves are admitted. With the forcing diagnosed from both the primitive model and the balanced model, they calculated the response from both forcing using a linear model. Their forced wave responses compared reasonably well with the simulated results of their primitive equation model. Pandya and Alexander (1999) and Song et al. (2003) both applied a quasi-linear model to study convectively generated gravity waves in a sheared 2D flow. Since their background flow is constant, they did not consider the flow separation. Their forced wave response shows reasonable agreement with the primitive equation solution, although details may not perfectly match the primitive equation solution. The basic approach in the current study is similar to these three studies. However, the dipole flow

considered here, albeit quasi-stationary, is much more complicated in terms of its three dimensional spatial structure than those considered in the three studies mentioned above.

Different from the linear model approach, Viúdez (2007) focused on the vertical velocity diagnosis using the general omega equation. He recovered the low wavenumber feature upstream the jet exit region inertia-gravity waves in the vertical velocity fields; this low wavenumber feature is the same ascent and descent couplet discussed in Snyder et al. (2007). Based on this finding, Viúdez concluded that these waves originate from one particular forcing to the general omega equation, i.e., the material rate of change of the ageostrophic differential vorticity. However, the general omega equation in Viúdez (2007) does not admit the wave solution, which is the key of his interpretation. The linear model introduced in Section 3 is able to fully recover the wave solution with appropriate forcing. Here, the forcing terms are diagnosed from the primitive equation solution. The linear model response to these forcing terms is reported in this section. It will be shown that the vorticity forcing plays the leading role, which seems to be consistent with Viúdez's conclusion.

It has been conjectured by a couple of studies that one of the residual tendency terms, ΔNBE (the residual of the nonlinear balance equations), provides the forcing to the wave generation. Past studies also suggest that in many cases, ΔNBE is a good flow imbalance indicator and can be used to infer the location and timing of gravity wave events (e.g., Zhang et al. 2000). However, this conjecture has not been formally verified or disproved in any literature known to the author. Therefore, it is of great interest to study linear wave responses to the flow imbalance indicator ΔNBE.

Two cases are considered here. One is the wave response to the forcing diagnosed from the balanced fields as discussed above. The other is the wave response to ΔNBE. The vertical motion couplet features distinct from the QG omega are discussed first since this special feature has implications for wave generation. Linear responses to the diagnosed forcing are discussed next. Also, wave response to ΔNBE is presented.

4.2 Forcing diagnosed from the balanced flow and the responses

a. Review of secondary circulations associated with the dipole jet

The localized jets in the middle level and surface vortex dipoles discussed in the previous section are characterized by a Rossby number ~ 0.2. To the first order approximation, geostrophic balance dynamics describe the basic flow feature. Beyond that, quasi-geostrophic (QG) dynamics govern the commonly known secondary circulation associated with jet in the sub synoptic scales, which are part of so called balanced dynamics to the next order correction. This asymptotic balanced dynamics, albeit nontrivial, can be carried out to even high orders, so that a better approximation of the primitive equation set can be obtained. For example, Muraki et al. (1999) discussed such a possibility termed as 'QG+1' dynamics. Gravity waves are not part of the balanced dynamics and thus distinct from them in terms of the time scales and spatial patterns. Next we review some secondary flow features as the next order correction to the balanced dynamics in the dipole jet.

Figure 4.1 a-b shows the full vertical velocity at 210 h. Fig. 4.1 c-d shows the classical four-cell pattern of the QG vertical velocity at 13.9 km at 210 h. The QG vertical velocity is calculated using QG omega equation (Holton 2004), which is

available from the RIP package. The secondary circulations are mainly due to flow acceleration/deceleration at the jet entrance/exit region. For example, southward ageostrophic motion (Fig. 4.1 c) induced by flow deceleration is seen at the jet level in its exit region. This southward motion, together with downward motion in the anticyclonic side, a return (northward) flow at low levels (~ 8 km) and upward motion in the cyclone side (Fig. 4.1 d), closes an anticlockwise circulation below the jet level when viewed from its downstream. In contrast, a clockwise circulation is seen above the jet level with upward (downward) motion in the anticyclone (cyclone). As a result, these vertical motions form a quadruple pattern in the exit region of the jet (Fig. 4.1 b).

Figure 4.1 e-f shows the difference between full w and QG w. An ascent/descent couplet is present both above and below the level of the maximum wind (~11.5 km). This feature has been discussed by Snyder et al. (2007) and Viúdez (2007). It is used to infer the Rossby number dependence by Snyder et al. 2007. Viúdez (2007) recovered this low wavenumber feature by inverting the generalized omega equation and concluded that this is responsible for wave generation. He found that the origin of this ascent/descent couplet feature is the material rate of change of the ageostrophic differential vorticity. In the following section, it will be shown that our linear model can also recover this ascent/descent feature.

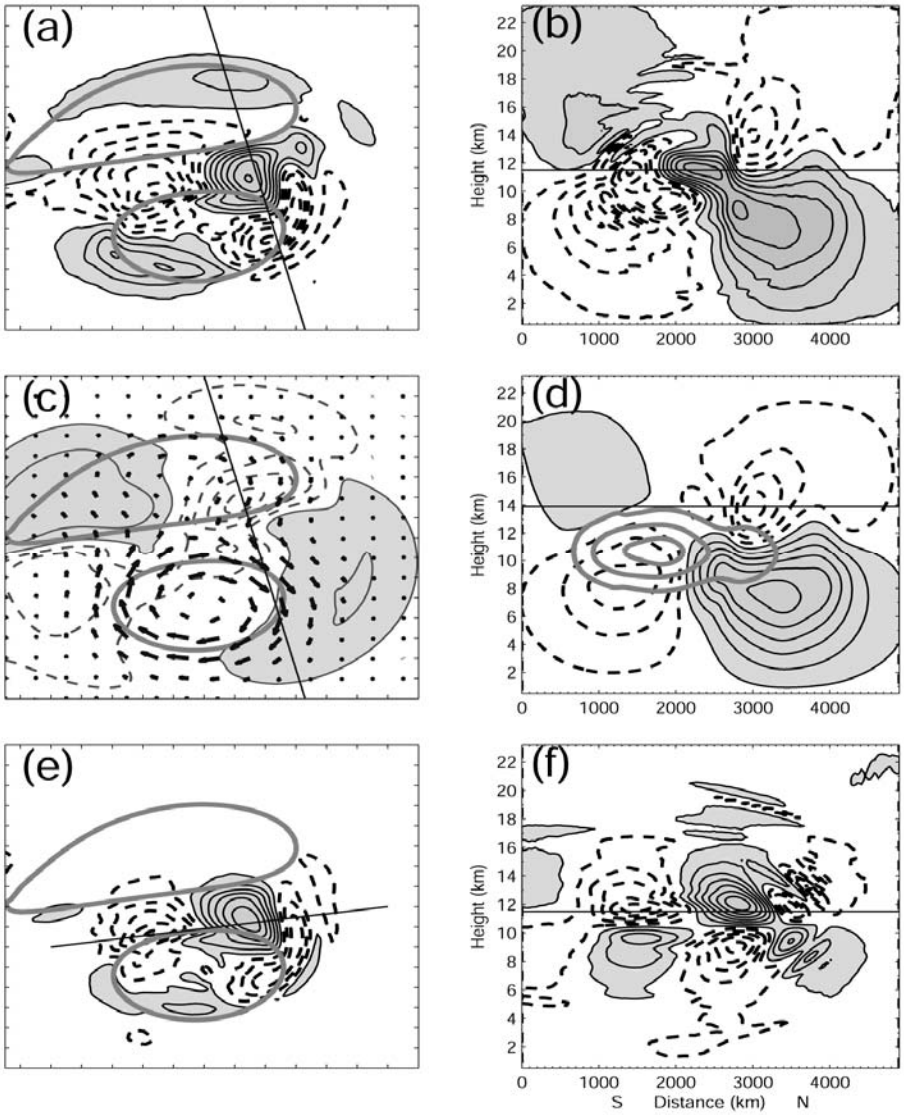

Figure 4.1. Vertical velocity (ci = 0.05 cm/s; solid and shaded, positive; dashed, negative) and PV (thick gray solid lines, 0.5 and 3.5 PVU) plotted at 210 h at 11.5 km (a) and in the vertical plane (b) indicated by the thin line in panel (a). Panels (c) and (d) are almost the same as (a) and (b), except that the QG vertical velocity is plotted. Ageostrophic wind vectors are also plotted in (c) and ageostrophic wind speed (ci = 2.5 m/s, gray contours) is plotted in (d). Panels (e) and (f) are the same as (a) and (b) except that difference between full w and QG w are plotted. The horizontal thin lines in the right panels indicate the height of either the divergence or the vertical velocity in the left panels. The distance between ticks in the left panels is 300 km.

b. Forcing diagnostics

Forcing from gravity-wave-free primary flow is the key to the response of the linear model. There are two ways remove waves from diagnosed forcing. One way is to calculate the forcing from model output and then separate the large scale forcing from the small scale waves using digital filters. However, direct calculation of the three terms F_δ, F_θ and F_ζ from MM5 output will likely contain gravity waves regardless any filtering technique to be used. This raises some concerns that forced waves in the linear model may be themselves contained in the forcing. As a result, separation of background flow from waves using filtered dynamical models is necessary. In this approach, the MM5 solution is approximated with a balanced state from which forcing can be diagnosed. Reduced equation sets that approximate large scale geophysical flow and filter out gravity waves are useful here. For example, geostrophic and quasi-geophysical models are such models that provide low order approximations. However, geostrophic balance is not suitable here since QG models significantly underestimate the magnitude of large scale flow (e.g., McIntyre and Norton 1990). A better choice is to obtain balanced flow through potential vorticity inversion combined with the nonlinear balance equation. Potential inversion operator has been proved to be highly accurate in the rotating shallow water model (McIntyre and Norton 2000). The benefit of using direct potential vorticity inversion is that all balanced fields are readily available through direct potential vorticity inversion, rather than through forward time integration of a balance model. The potential vorticity inversion procedure discussed in Section 2.2 is employed to obtain balance flow.

For the current problem, the background flow from the 30-km domain of the MM5 simulation provides variables including horizontal winds, vertical velocity, pressure and potential temperature as input for the linear model. Most variables such as u, v and θ can be easily obtained by inverting EPV. Computing the balanced vertical velocity w, however, is not straightforward, since that involves solving a more complicated elliptical equation system. In practice, two options are available. First, the vertical velocity in the large scale balanced flow is approximated by the QG vertical velocity, which has similar amplitude to or less than the amplitude of wave disturbance. It turns out that the QG vertical velocity suits this purpose well. Second, we can use w derived from the balanced wind using incompressibility condition $U_x + V_y + W_z = 0$. No significant difference between these two options is found for the final linear model results. Results using the QG vertical velocity are discussed below.

Figure 4.2 shows the three forcing terms F_δ, F_ζ and F_θ (Eqns. 3.3 and 3.5). They are computed from the balanced approximation to the MM5 solution at 210 h. The time tendency of large scale flow ($\partial_t \delta_B$, $\partial_t \zeta_B$, $\partial_t \theta_B$) in Eqn. 3.3 and 3.5 has been dropped off for the large scale flow, since the characteristic time scale of large scale flow is much larger than those of disturbance, and these time tendency terms are much smaller than the other terms. F_δ and F_ζ are computed following Eqn. 3.5. Computation based on a simplified version of the three forcing terms in Eqn. 3.6 produces similar results. The forcing terms in Fig. 4.2 have been smoothed by a 2D digital filter with a cut-off wavelength 600 km. Nevertheless, F_δ in Fig. 4.2 a and b does not have the localized structure as ΔNBE (Fig. 2.5). This is because F_δ is mainly composed of two terms: the

nonlinear advection of divergence and ΔNBE, and they cancel each other. In fact, since ΔNBE=0 provides a balanced constraint for the potential vorticity inversion operator, the residual of nonlinear balance equation in the forcing term F_δ automatically disappear. Also, no apparent localized or compact structures are found in F_θ (Fig. 4.2 c and d) near the jet core. Among the three forcing terms, only the vorticity forcing F_ζ (Fig. 4.2 d) does show some compact structures and reaches its maximum and minimum between 9 and 11 km near the jet core.

The equivalent forcing terms G_δ, G_θ and G_ζ corresponding to F_δ, F_θ and F_ζ, together with the total forcing $G_\delta+G_\theta+G_\zeta$, are plotted in Fig. 4.3. Among the three equivalent forcing terms, G_ζ has the maximum amplitude $0.1\times10^{-16} m^{-1}\cdot s^{-3}$, while G_δ and G_θ have their maximum amplitude $0.0015\times10^{-16}\ m^{-1}\cdot s^{-3}$ and $0.015\times10^{-16} m^{-1}\cdot s^{-3}$. Thus their sum is determined by G_ζ and has its maximum $\sim 0.1\times10^{-16} m^{-1}\cdot s^{-3}$. The sum of these three terms $G_\delta+G_\theta+G_\zeta$ reveals a clear compact structure with a quadruple pattern concentrated near the jet core. This quadruple pattern is also very similar to the idealized forcing in Fig. 3.12 b despite the difference in their amplitude. Thus, it also suggests an origin of the ascent-descent couplet in Fig. 4.1 and Snyder et al. 2007. This interpretation is further supported by results from the linear model, as discussed in details below.

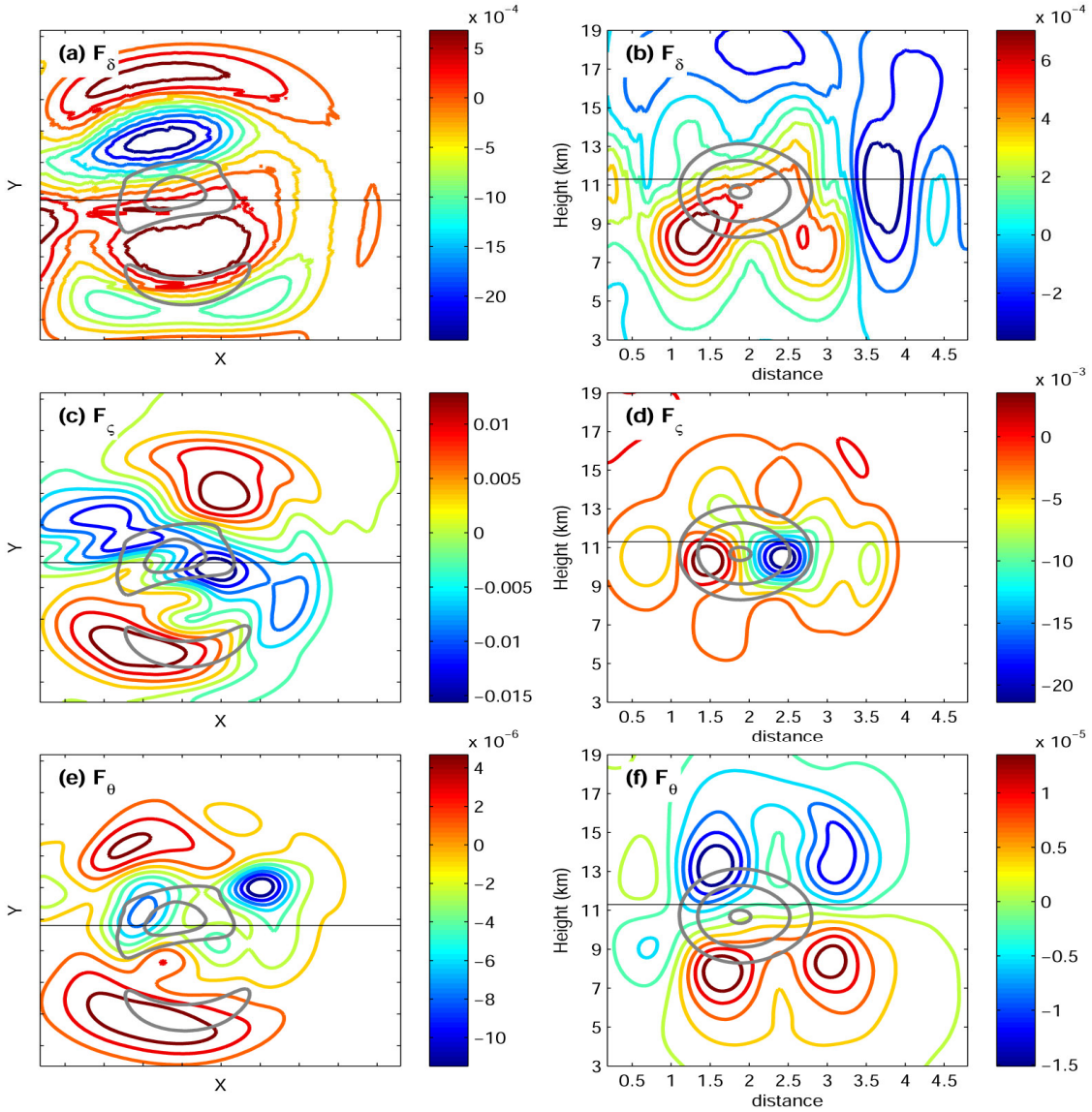

Figure 4.2 Three forcing terms F_δ, F_θ and F_ζ on horizontal (the left column) and vertical planes (the right column) computed using the rebalanced fields at 210 h. F_δ and F_ζ have a unit $1\times10^{-8} m\cdot s^{-2}$. F_θ has a unit $1K\cdot s^{-1}$.

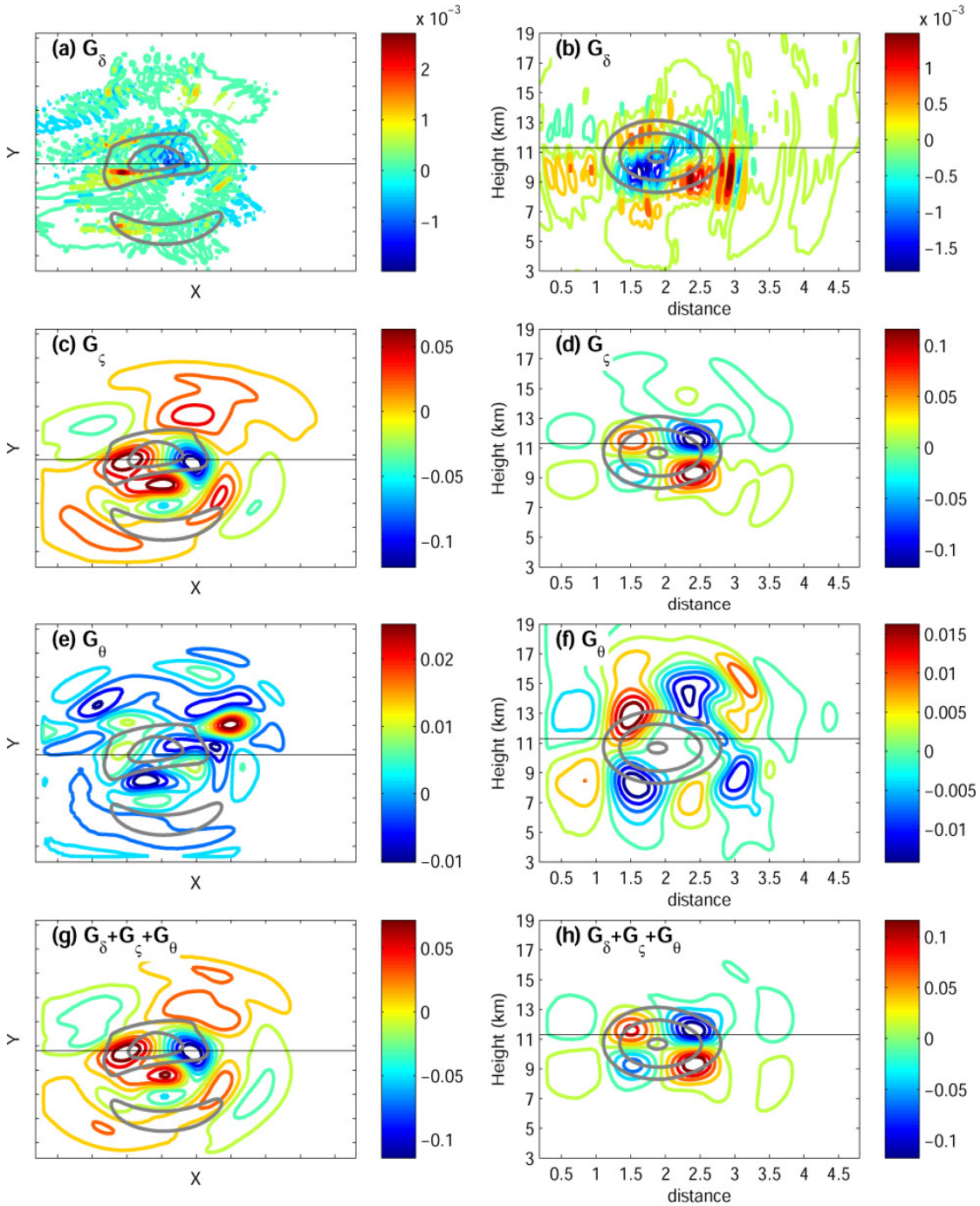

Figure 4.3 Three individual forcing terms G_δ, G_θ and G_ζ and their sum plotted on horizontal (the left column) and vertical planes (the right column). All fields have a unit $1\times10^{-16} m^{-1}\cdot s^{-3}$.

Note that when a multidimensional digital filter is used to separate wave signals from the large scale flow, the filtering technique appears to successfully separate wave from the background flow when the forcing terms F_δ, F_θ and F_ζ are plotted. However, the corresponding forcing terms G_δ, G_θ and G_ζ are not; wave pattern similar to the MM5 simulated vertical velocity can be found (not shown) in $G_\delta+G_\theta+G_\zeta$. Thus, the potential vorticity inversion procedure is a better choice to separate waves from the balanced flow. In fact, Fig. 4.3 also indicates that waves are almost separated from the large scale flow.

c. Response of the linear model to the diagnosed forcing

The linear model is integrated with forcing diagnosed in Fig. 4.3 starting from zero initial conditions. The following are some numerical details of the linear model. The non-dimensional constant horizontal and vertical diffusion coefficients for the scale selective 4th order diffusion scheme are $1x10^{-3}Dx^4/Dt$ and $1x10^{-3}Dz^4/Dt$, where Dx=30 km, Dz = 200 m, and Dt = 150 s are horizontal, vertical resolution, and time step. The computational domain for the linear model is a subset of Domain 2 in the MM5 simulation and has a dimension of 155x165x100 points. The solution in Fig. 4.3 includes not only a general pattern that compares well with the MM5 solution (details below), but also modes that possibly induced by the rigid top and bottom boundaries (or sponge layers). A small Rayleigh damping coefficient (with its maximum value of $1x10^{-5}\ s^{-1}$) is particularly helpful to eliminate these modes. The damping layer is 3 km deep near the bottom and top boundaries and 450 km wide near the lateral boundaries. Newtonian cooling is also included with a coefficient of $5.5x10^{-7}s^{-1}$ (500 hours). The spatial

structure barely changes after 200 hours. A quasi-steady state is achieved around 300-400 hours. The results discussed in the following are obtained through integration time up to more than 1000 hours with both background wind and forcing fixed over the whole integration time.

In the dipole flow, disturbance winds *u'* and *v'* can be inverted from divergence and vorticity by solving Poisson's equations giving appropriate boundary conditions. However, in practice, we neglect the shear terms such as $\overrightarrow{u'}\nabla\delta_B$, i.e., the advection of primary flow by disturbance winds. This is similar to the WKB approximation, but can significantly reduce the computational cost.

Figure 4.4 displays the response fields (including the horizontal divergence and the vertical velocity) to these forcing terms F_δ, F_θ and F_ζ from the linear model (Fig. 4.2). For comparison, the MM5 simulation is also plotted in Fig. 4.4, but with contour intervals twice of that for the linear model solution. In general, the linear model solution, at least the general pattern, reasonably agrees with the MM5 solution. Underestimate of the wave amplitude might be due to the smoothing effect of the low pass filter used for the wave forcing calculation. The wave pattern at 13 km and along the dipole axis is close to the MM5 simulation in terms of phase in the immediate jet exit region. For example, the first wave band (from the horizontal divergence) downstream the jet core appears almost the same distance relative to the 20 m/s wind contour. However, the wave bands do not extend to the anticyclonic region as in the MM5 solution (cf. Fig. 4.4 a and c). The transient waves below 5 km and above 16 km in the MM5 solution are absent in steady state solution. Nevertheless, they are present in the early time

integration of the linear model solution and disappear gradually. Another difference is the wave bands in the anticyclone region. These waves may have frequency smaller than the Coriolis parameter, as discussed in Section 2.4 (See Fig. 2.9). The difference between the MM5 solution and the linear model solution may arise from many approximations we have made.

Wave amplitude at the leading edge, however, is not expected to match between the linear model solution and the MM5 solution, since both horizontal and vertical wavelengths decrease to the scale that is barely resolvable by the numerical models at the far leading edge of wave packets. At that scale, the diffusion operator becomes important. Although the diffusion schemes in MM5 and the linear model are both biharmonic, MM5 used a horizontal deformation dependent diffusion scheme, while the linear model uses simply a constant coefficient. Therefore, grid scale motions behave differently in these two models. Nevertheless, neither of these two diffusion schemes is realistic since they are a simple treatment of subgrid scale processes. The end results of these two schemes are to filter out the small scale eddy mixing effect. Further investigation of subgrid diffusion and its potential impact is beyond the scope of the current study.

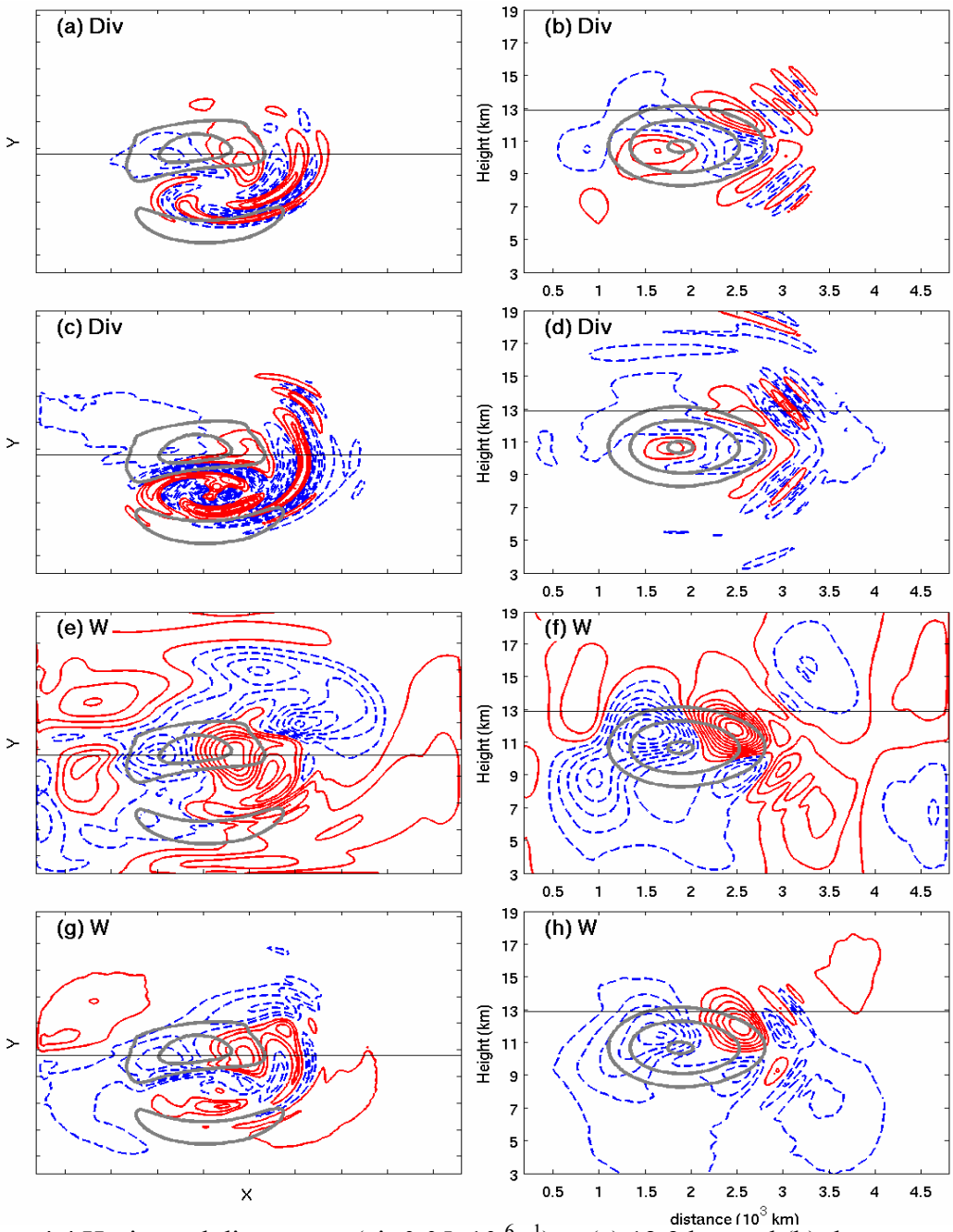

Figure 4.4 Horizontal divergence (ci=0.05x10^{-6}s^{-1}) at (a) 12.9 km and (b) the corresponding vertical cross section from the linear model. (c) and (d) are the same as (a) and (b) except ci = 0.1x10^{-6}s^{-1} from the MM5 solution at 210h. Panels (e) and (f) are the vertical velocity (ci=2.5x10^{-4}ms^{-1}) at 12.9 km and vertical plane from the linear model. (g) and (h) are the same as (e) and (f) except ci = 5.0x10^{-4}ms^{-1} from the MM5 solution at 210h. Wind speed (gray lines) is contoured at 20, 25, 30 m/s either at 11.5 km or along the vertical cross section. The solid gray lines at the left panels indicate the cross sections in the right panels.

Comparing panels e and g, f and h in Fig. 4.4 suggests that the linear model solution also captures the ascent/descent couplet of the vertical velocity at almost the same location as in MM5 solution. However, the amplitude is underestimated by the linear model, for example, both the horizontal divergence and the vertical velocity along the dipole axis are approximately more than half of the MM5 solution. From both the linear model solution and MM5 solution, the ascent/descent couplet above is maximized at 12 km. A second ascent/descent couplet with weaker amplitude is maximized at 9 km. Together they form a quadruple pattern collocates with the equivalent forcing $G_\delta+G_\theta+G_\zeta$. Downstream of this quadruple pattern are propagating inertia-gravity waves. This spatial structure of forcing and responses are similar to the results when idealized forcing is prescribed (cf. Fig. 3.10 a and Fig. 3. 13 b). The responses from both the diagnosed forcing and the idealized forcing suggest a wave generation picture: the large scale forcing first induce the large response (compared with that of gravity waves) in the form of ascent/descent couplet below and above the jet; then the flow passing the ascent/descent couplet naturally generate vertically propagating gravity waves in analogy to the flow pass elevated heating. Their vertical propagation may rely on whether the horizontal scale can be efficiently projected to vertical propagating wave modes in accordance of the dispersion relation. The projection of forcing to wave modes is certainly not monotonic in terms of the scales, i.e., it is not true that the larger of forcing scales, the stronger of wave response. This has been demonstrated in Fig. 3.4 a-d.

d. Response to the individual forcing terms

Linear model solutions are also obtained by applying each of the three forcing terms F_δ, F_θ and F_ζ. Figure 4.5 shows the results when F_ζ is applied to the linear model. Both the fields near the jet core and downstream wave signals are very similar in comparison with Fig. 4.5 except that the two fields are less noisy. Linear response to the each individual term of $F_\varsigma = -\overrightarrow{U_B}\nabla\varsigma_B - f\delta_B$, is also obtained. Again, the time tendency is neglected since it is very small. The spatial pattern of G_ζ with only $-\overrightarrow{U_B}\nabla\varsigma_B$ included is almost the same as G_ζ as $F_\varsigma = -\overrightarrow{U_B}\nabla\varsigma_B - f\delta_B$ (Fig. 4.3 c and d). Wave response to $-\overrightarrow{U_B}\nabla\varsigma_B$ is almost the same as F_ζ. Therefore, the advection of vorticity ($-\overrightarrow{U_B}\nabla\varsigma_B$) is mostly responsible for wave generation, $-f\delta_B$ plays only a minor role. This suggests the role of the jet flow on wave generation. That is, the horizontal advection due to the localized jet helps build up the quadruple pattern in the vertical velocity; this pattern is similar to those seen in the idealized forcing (e.g., Fig. 3. 12 b and d).

Figure 4.6 shows the linear responses from the other two forcing terms F_δ and F_θ. The linear response to F_δ and F_θ hardly contains any meaningful wave responses. Specifically, the corresponding fields near the jet core (e.g., the ascent/descent couplet) are absent and the wave solutions are at least five times weaker than waves forced by F_ζ with spatial pattern inconsistent with the MM5 solution. This is also consistent with the diagnosis of equivalent forcing G_ζ, G_δ and G_θ (Fig. 4.3) since G_δ and G_θ are at least one magnitude smaller than G_ζ. These sensitivity tests suggest that the vorticity forcing provides the leading contribution to wave generation in the dipole jet flow.

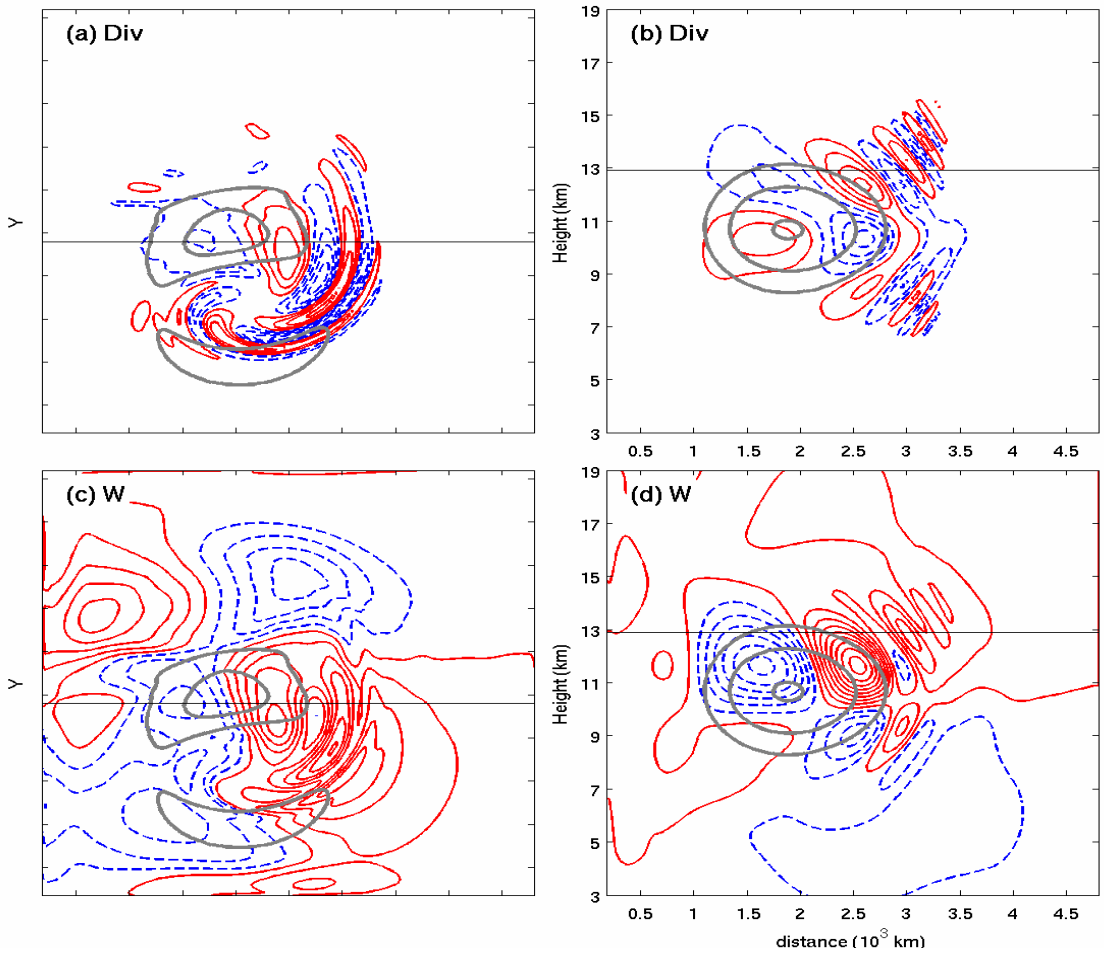

Figure 4.5 Linear responses to F_ζ from the linear model. Plotted in panels (a) and (b) are the horizontal divergence (ci=0.05x10^{-6}s^{-1}) at 12.9 km and in the vertical plane indicated by the solid gray lines in the right panels. Plotted in panels (c) and (d) are the vertical velocity (ci=2.5x10^{-4}ms^{-1}) at 12.9 km and in the vertical planes. Wind speed (gray lines) is contoured at 20, 25, 30 m/s either at 11.5 km or along the vertical cross sections.

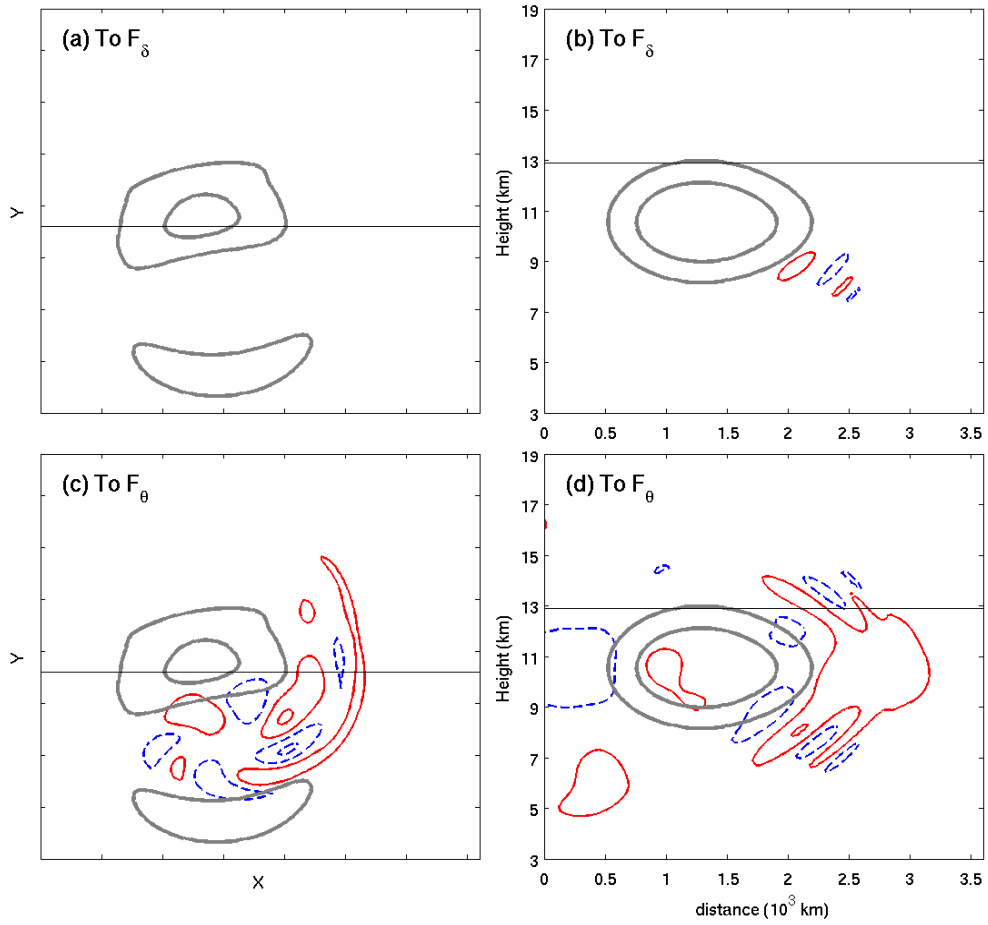

Figure 4.6 Linear response due to F_δ in panels (a) and (b) and F_θ in panels (c) and (d) from the linear model. Horizontal divergence (ci=0.05x$10^{-6}$$s^{-1}$) due to F_δ is plotted at 12.9 km in panel (a) and vertical plane in panel (b). Panels (c) and (d) are the same as (a) and (b) except that plotted is the horizontal divergence due to F_θ.

e. Sensitivity experiments

A couple of sensitivity experiments are also performed. These experiments demonstrate that the above linear model wave responses are very robust.

e.1 Effects of horizontal smoothing on the linear response

In order to evaluate the smoothing effect of the low pass digital filter, additional experiments are performed by changing the cut-off wavelength of the digital filter. In one simulation, the cut-off wavelength is chosen to be 240 km. The forcing terms are noisy (not shown), and the spatial structure is not as clean as that in Figs. 4.2 and 4.3.

Figure 4.7 a and b show the linear wave response in this run. It appears that wave amplitudes become stronger and general wave pattern are very similar to those discussed for Fig. 4.4 a and b. For example, wave signatures extend further to the anticyclone in Fig. 4.7 a. Nevertheless, the wave pattern is robust when different smoothing filter is applied. This experiment suggests that smoothing may cause the weakening of the forcing and its wave response. This is not unexpected because it is well known that the response function to a band pass filter is not an ideal window and damp the power nearby the chosen window.

e.2 Response to the forcing diagnosed from different vertical velocity

In order to evaluate the role of the vertical velocity, additional experiments are performed by using the vertical velocity derived from the balanced winds or zero vertical velocity for forcing diagnose. Figure 4.7 c and d show the horizontal divergence obtained from steady state solution from the linear model. The general wave pattern shows only minor changes. This suggests that the linear model solution is not sensitive to the QG vertical velocities in comparison in those in Fig. 4.4 a. This sensitivity test adds on the confidence of our ad hoc treatment of the vertical velocity in the wave operator.

e.3 Response to the forcing using the balanced wind for the linear model

In all the previous discussions, model winds are used on the left hand side of the linear operator. In order to evaluate this effect, experiments are also performed with balanced wind on the left hand side of the linear operator. Figure 4.7 e and f show the horizontal divergence from the linear response in comparison in those in Fig. 4.4 a and b. It appears that difference between these two solutions is marginal, although wave amplitude decreases a little since the balanced wind is used.

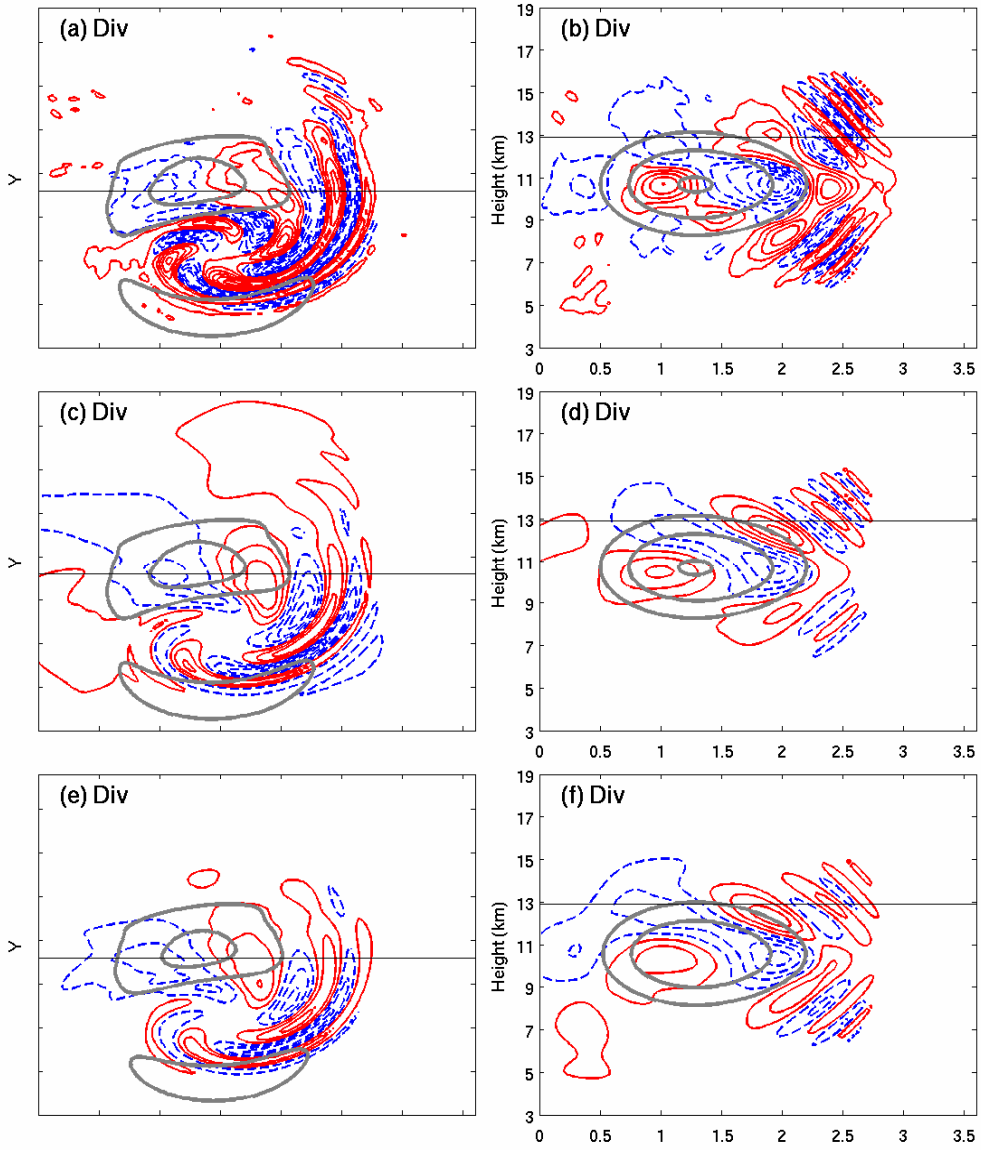

Figure 4.7 Sensitivity experiments. Horizontal divergence (ci=0.05x$10^{-6}$$s^{-1}$) at 12.9 km in panel (a) and along the vertical cross section in panel (b), when a 240 km filter is used to smooth the wave forcing terms for the linear model. Panels (c) and (d) are the same as panels (a) and (b), except that zero vertical velocity is used as the background vertical velocity. Panels (e) and (f) are the same as (a) and (b), except that balanced wind is used as the background wind. Background wind speed (gray lines) is contoured at 20, 25, 30 m/s either at 11.5 km or along the vertical cross section in each panel.

4.3 Linear response to the flow imbalance

The flow imbalance indicated by the residual of the nonlinear balance equation has been discussed in Section 2. It has a localized spatial structure that collocates with the jet core. It is suggested in many literatures (e.g., Kaplan and Paine 1977, Zhang et al. 2000) that ΔNBE is a good flow imbalance indictor. Past studies also suggest that ΔNBE can be used to infer the location and timing of gravity wave events. However, this conjecture has never been formally verified or disproved. It is thus of great interest to study wave response to this flow imbalance indicator ΔNBE in this linear model.

Figure 4.8 shows ΔNBE and derived form of ΔNBE, $G_{\Delta NBE}$, following Eqn. 3.8,

$$G_{\Delta NBE} = -(\partial_t + \overrightarrow{U_B}\nabla)\frac{\partial}{\partial z}\Delta NBE\,, \qquad (4.1)$$

These terms are computed using the MM5 output at 210h. Besides the localized structure in ΔNBE, the forcing of the vorticity equation. Note that these three terms has been filtered by a 2D band pass filter with a cut off wavelength 600 km in order to remove the small scale wave signatures. Nevertheless, the tilted patterns of $G_{\Delta NBE}$ along the dipole axis in these derived forcing terms resemble the waves with distinct crests and troughs. It is possible that they are part of wave signals that are not completely removed by the digital filters. This also highlights that the forcing terms can be easily contaminated by waves themselves if balanced fields are not used.

Figure 4.9 shows the response of the linear model to these forcing. The wave pattern from the horizontal divergence field is similar to the wave solution in the MM5 solution. However, the wave phase is reversed. There is also a phase shift from the horizontal divergence at 12.9 km (Fig. 4.9 c) between the linear model solution and the

MM5 solution (Fig 4.9 c and d). The difference between these two solutions is more pronounced in the vertical velocity fields (Fig 4.9 g and h). The ascent/descent couplet is not as strong as that in the MM5 solution. Despite these differences, the general wave pattern from the horizontal divergence is still similar to the MM5 solution if these fields are plotted with reversed sign.

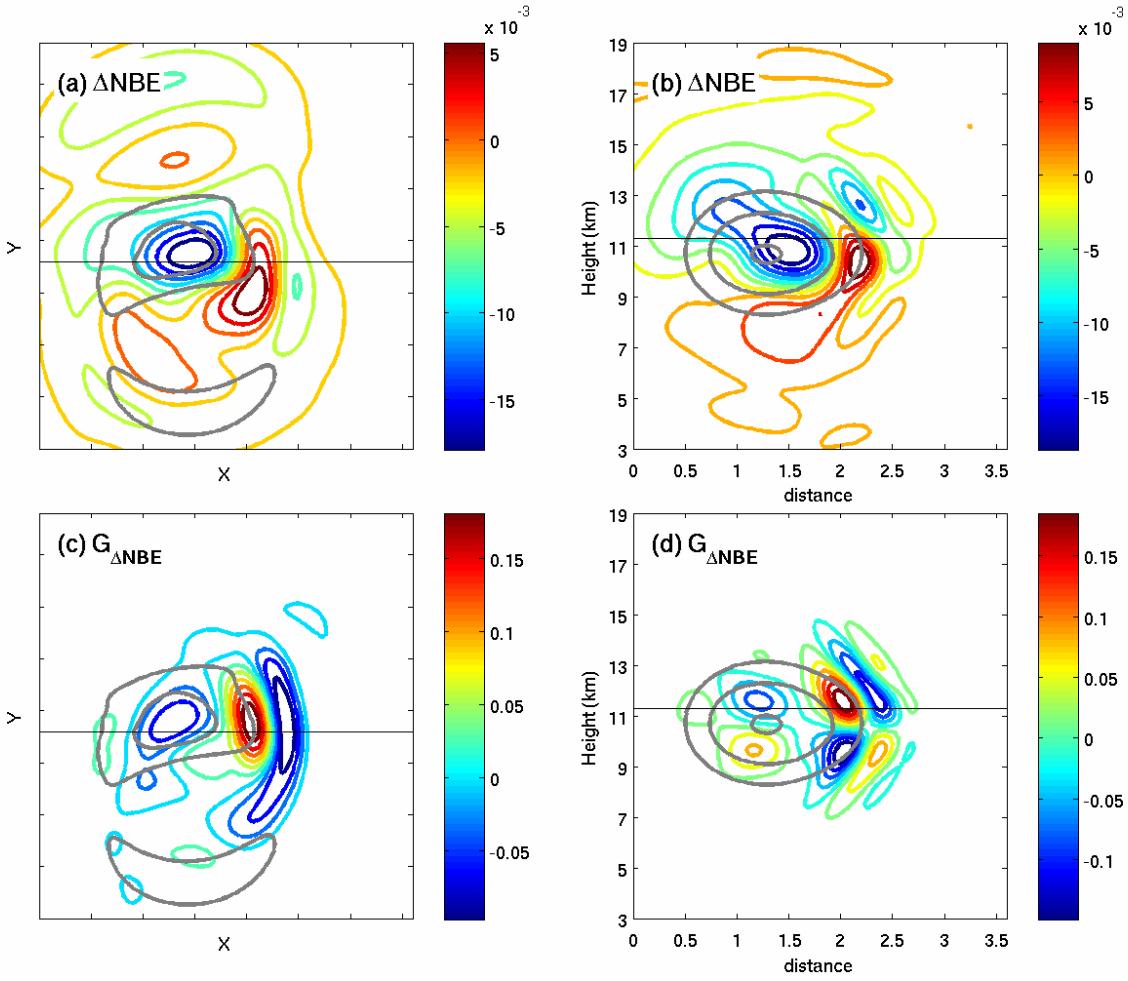

Figure 4.8 ΔNBE at (a) 11.5 km and (b) the corresponding vertical plane, and $G_{\Delta NBE}$ at (a) 11.5 km and (b) the corresponding vertical plane. ΔNBE has a unit of $1\times10^{-8}s^{-2}$. $G_{\Delta NBE}$ has a unit of $1\times10^{-16}m^{-1}\cdot s^{-3}$.

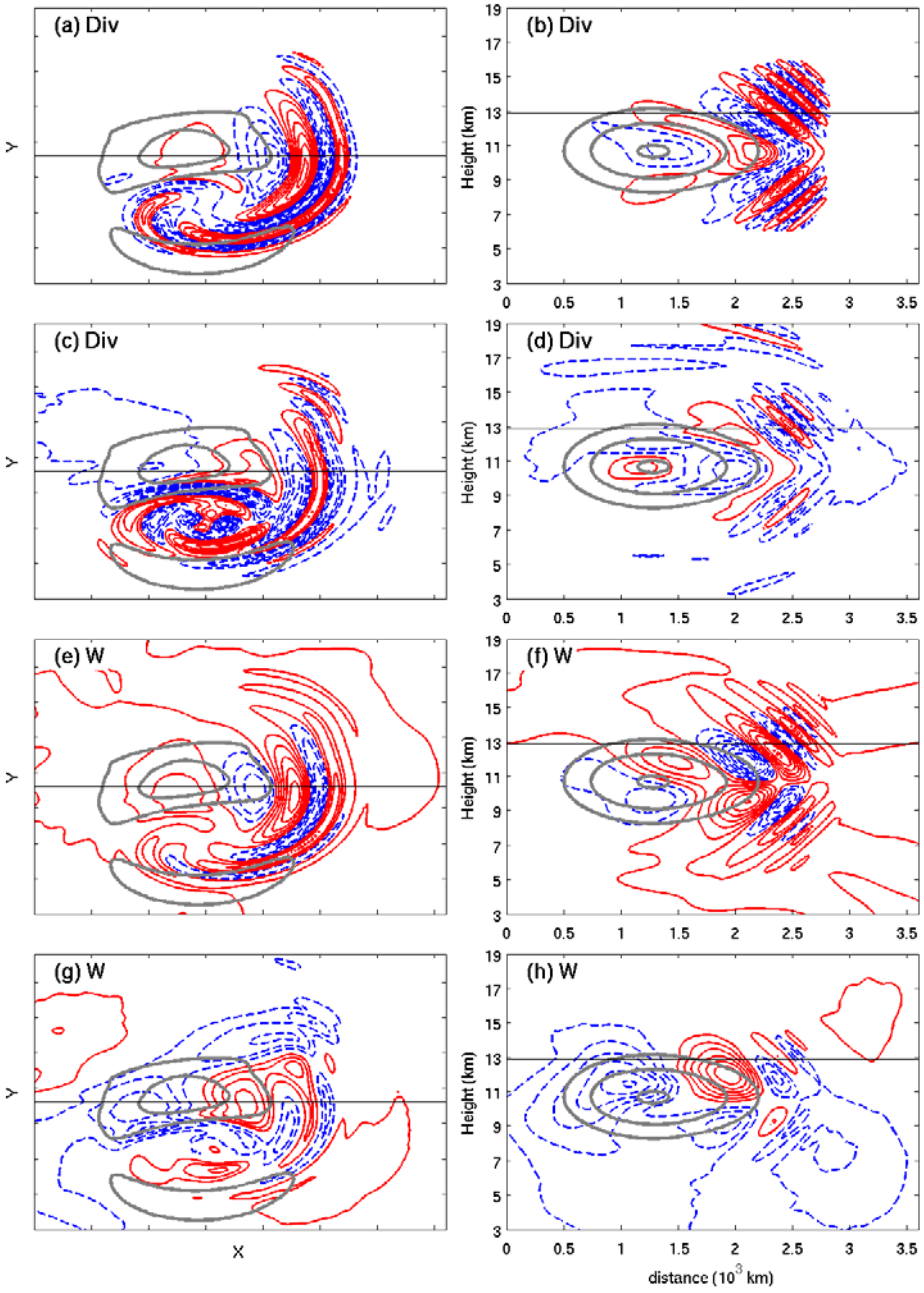

Figure 4.9 The same as Fig. 4.4 except that ΔNBE is used as the wave forcing.

There is a possibility that wave response to ΔNBE come from the waves contained in the forcing. However, from the prescribed forcing discussed in the previous section, it is more likely that the localized structure of ΔNBE is responsible for waves with reversed phase in the ΔNBE response. To understand why ΔNBE forces waves with reversed sign, let us consider $G_{\Delta NBE}$, the equivalent forcing of ΔNBE,

$$\begin{aligned} G_{\Delta NBE} &= -(\partial_t + \overrightarrow{U_B}\nabla)\frac{\partial}{\partial z}(f\varsigma + 2J(u,v) - \nabla^2\Phi) \\ &= -f\frac{\partial}{\partial z}(\partial_t + \overrightarrow{U_B}\nabla)\varsigma + [f\partial_z\overrightarrow{U_B}\cdot\nabla\varsigma - (\partial_t + \overrightarrow{U_B}\nabla)\frac{\partial}{\partial z}(2J(u,v) - \nabla^2\Phi)]. \\ &= -f\frac{\partial}{\partial z}(\partial_t + \overrightarrow{U_B}\nabla)\varsigma + \cdots \end{aligned} \quad (4.2)$$

In the above, the total flow is used to evaluate ΔNBE rather than using the balanced flow (the terms denoted by a subscript B) as in Eqn. (3.9). The dominate forcing term G_ζ as identified in the previous section is,

$$\begin{aligned} G_\varsigma &= -f\frac{\partial}{\partial z}F_\varsigma = -f\frac{\partial}{\partial z}\left[-(\partial_t + \overrightarrow{U_B}\nabla)\varsigma + f\delta\right] \\ &= f\frac{\partial}{\partial z}(\partial_t + \overrightarrow{U_B}\nabla)\varsigma + \cdots \end{aligned}, \quad (4.3)$$

Thus we can identify one term in common in $G_{\Delta NBE}$ and G_ζ, that is, $f\frac{\partial}{\partial z}(\partial_t + \overrightarrow{U_B}\nabla)\varsigma$ appears in both $G_{\Delta NBE}$ and G_ζ but with a reversed sign. Note that $f\frac{\partial}{\partial z}(\partial_t + \overrightarrow{U_B}\nabla)\varsigma$ comes from the advection of relative vorticity $-\overrightarrow{U_B}\nabla\varsigma$, which is the leading contribution to wave forcing and its appearance in G_ζ produces wave response with almost right phase. On the other hand, $-f\frac{\partial}{\partial z}(\partial_t + \overrightarrow{U_B}\nabla)\varsigma$ appears in $G_{\Delta NBE}$, thus it is not surprising

that $-f\frac{\partial}{\partial z}(\partial_t + \overrightarrow{U_B}\nabla)\varsigma$ will produce waves with phase reversed. The appearance of relative vorticity term in ΔNBE possibly explains how *ΔNBE* ($G_{\Delta NBE}$) generates wave response with phase reversed. In fact, $f\varsigma$ as the only forcing to the divergence equation also produces wave response with a reverse sign but stronger wave amplitude (not shown).

Since the vorticity term ($f\varsigma$) in ΔNBE is linear, one might suspect that wave forcing is a linear mechanism. However, this is not complete picture since ΔNBE is only part of the forcing in the formulation of PZ07. The forcing is essentially nonlinear because the vorticity forcing in Eqn. 3.5 is dominant by the nonlinear terms, that is, the horizontal advection of vorticity.

Combining $G_{\Delta NBE}$ and G_ζ gives,

$$G_{\Delta NBE} + G_\varsigma = f^2\partial_z\delta + f\partial_z\overrightarrow{U_B}\cdot\nabla\varsigma - (\partial_t + \overrightarrow{U_B}\nabla)\frac{\partial}{\partial z}(2J(u,v) - \nabla^2\Phi)\,. \qquad (4.4)$$

The remaining terms are the difference between $G_{\Delta NBE}$ and G_ζ. Nevertheless, the above analysis does not imply that the remaining terms on the right hand side do not produce wave responses. Rather, it suggests how *ΔNBE* is related to F_ζ, and it is relative vorticity appearing in either *ΔNBE* or F_ζ that contributes to observed wave pattern.

The linear response to the flow imbalance considered in this section confirms that flow imbalance indicator *ΔNBE* is able to produce wave response, but the phase of wave response is reversed. This suggests that localized *ΔNBE* is a very useful indicator for the wave generation, at least in the current vortex dipole flow.

4.4 Summary and discussion

This section investigates the source mechanism of gravity waves within the dipole flow. The three types of forcing enforced to the linear model that are formulated by Plougonven and Zhang (2007) are diagnosed from balanced flow. The potential vorticity inversion procedure that is constrained by the nonlinear balance is used to obtain the balanced flow. The forcing terms diagnosed from the balanced flow provide some physical insight by themselves. Their spatial structure and magnitude are compared in their *equivalent form*. Among the three, the vorticity forcing is one magnitude larger than the other two and shows a quadruple pattern in the vertical. The linear model is used to find steady state wave solutions the diagnosed forcing.

Results from the linear model computations reveal that the vorticity forcing is the leading contribution to both gravity waves in the jet exit region and the ascent/descent couplet in the jet core. In general, the linear model solution is in reasonable agreement with the MM5 solution, although the wave magnitude is only more than half of waves in the linear model. Our conclusion seems to be consistent with Viúdez (2007). However, the linear model approach is able to recover the wave solution, which is not in Viúdez (2007).

Based on the wave forcing diagnosis and the linear model solutions, a wave generation scenario is suggested: the large scale forcing diagnosed from the balanced flow first induces the large scale responses (compared with that of gravity waves) in the form of ascent/descent couplet below and above the jet; the jet flow passing the ascent/descent couplet naturally generates vertically propagating gravity waves in

analogy to the flow passing elevated heating. The role of the localized jet seems clear: the horizontal advection of the localized jet provides one way to build up the quadruple pattern in the vertical velocity seen in the idealized forcing, the diagnosed forcing, and the response; the jet flow passing the forcing generate waves in the linear model; finally the horizontal shear and vertical shear of jet flow strongly constrains wave characteristics, as revealed by the 4D ray tracing analysis (Section 2.4) and 2D ray analysis (Section 3.3).

The linear response to the flow imbalance indicator *ΔNBE* demonstrates that the localized ΔNBE can generate steady wave responses of similar spatial pattern seen in the MM5 solution, but with wave phase reversed in the horizontal divergence field. A possible explanation is that relative vorticity, the leading contribution of wave forcing, also appears in ΔNBE but with a negative sign. Therefore, ΔNBE generates waves with phase reversed. Our linear model approach confirms ΔNBE can be safely used as an indicator of wave forcing and a predicator of gravity wave events.

From the wave forcing diagnosis of vortex dipoles, our results also suggest that the three forcing terms (the divergence, vorticity and thermodynamic forcing) can be used as the wave predicator. These wave forcing terms or even the derived *equivalent forcing* terms may not have localized structures as ΔNBE. Nevertheless, it should not be generalized that the vorticity forcing is the leading contribution in other types of flow. Instead, the importance of different types of forcing may be flow dependant. In the next section, it will be shown that the thermodynamic forcing is also important for gravity wave emission from a baroclinic jet.

5. LINEAR WAVE RESPONSES FROM A BAROCLINIC JET

5.1 Introduction

Upper level jet streaks and surface fronts are also present in the conceptual synoptic setting put forward by Uccellini and Koch (1987). These two mesoscale features are often considered possible sources for mesoscale gravity waves. The synoptic and mesoscale setting are also quite typical for mid-latitude jet-front systems during the life cycle of baroclinic waves. The first numerical study of gravity waves in such context was conducted by O'Sullivan and Dunkerton (1995). Later, Zhang (2004, hereinafter refer as Z04) performed idealized baroclinic wave simulations using a mesoscale model. He found mesoscale gravity waves with prevalent horizontal wavelengths of 100-200 km and intrinsic frequencies of approximately 3-4 f in the exit region of the upper-level jet. The wavelength and frequency were later reexamined in Wang and Zhang (2007, hereinafter refer as WZ07) and Lin and Zhang (2008, hereinafter refer as LZ08). These two studies found that these waves can be separated into two components with different wave characteristics: the medium-scale and the shorter-scale waves. Most recently, WZ07 and Plougonven and Snyder (2007) examined similar gravity wave activities during different life cycles of baroclinic waves. However, clear demonstration of the source mechanism of these waves is still lacking.

Geostrophic adjustment or generalized balance adjustment have been proposed as the wave source mechanism in the literature. Z04 found that the location and timing of the residual of the nonlinear balance equation ΔNBE, as a flow imbalance indicator, can

be used to predict the gravity wave event. Nevertheless, as noted by Lane et al. (2004) and LZ08, it is difficult to unambiguously determine which mesoscale systems are related to wave generation. For example, even with the advanced ray tracing analysis, the role of surface front and upper level jet remains yet unclear.

In view of the obvious difficulties of identifying the sources of the jet-exit-region waves, this section applies a linear model documented in Section 3 to the baroclinic-jet wave problem. In Section 4, the usefulness of linear model approach has been demonstrated in the vortex-dipole wave problem. Although gravity waves are quite similar in terms of their phases and locations relative to either the dipole jet or the baroclinic jet, they are also different in several aspects. First, the localized jet is quasi-steady in the moving framework of vortex dipoles, while the baroclinic jet is strengthening with respect to time. Second, the localized jet is relative simple in terms of its 3D structure, while the baroclinic jet is accompanied by surface fronts, which are another important wave sources. Third, gravity waves in the exit region of the localized jet have a stationary phase in an appropriate framework with an intrinsic frequency of $\sim 1.4 \times 10^{-4} s^{-1}$, but waves in the vicinity of the baroclinic jet are transient and have a higher frequency roughly $3\text{-}4 \times 10^{-4} s^{-1}$. Because of these differences, the linear model approach for the baroclinic jet is also different from that for the localized jet. Specifically, it is inappropriate to seek steady state wave solution for baroclinic jets; instead, time evolving background wind and forcing must be taken into account.

This section is structured as the following. The basic feature of gravity waves in the exit region of a baroclinic jet in Zhang (2004) is reviewed first. The linear model

driven by flow imbalance is discussed next. Flow separation via EPV inversion and linear response to forcing diagnosed from the balanced flow is further explored by running multiple linear model experiments.

5.2 Review of gravity waves and baroclinic waves in Zhang (2004)

The mesoscale model MM5 (Dudhia, 1993) used in Z04 and Wang and Zhang (2007) is configured to eliminate the effects of spherical geometry, topography and moisture. Potential vorticity inversion procedure was employed to create the initially balanced 3D jet and EPV perturbations that are seeded at the tropopause level. The control simulation in these two studies employs three model domains with grid spacing of 90, 30 and 10 km, respectively. The coarse model domain (D1) extends 27,000 km in east-west direction and 9000 km in north-south direction. Such a huge domain is chosen in order to minimize the influence from lateral boundaries. The 30-km domain (D2) is a rectangular subdomain 6,300 km long and 4,800 km wide within D1. The 10-km domain (D3) is a rectangular subdomain 3,100 km long and 2,500 km wide within D2.

The life cycle of the baroclinic waves in CNTL starts from the initial 3D EPV perturbations seeded at the tropopause level. In short, subsequent baroclinic development is similar to the classic life cycle of baroclinic waves in many aspects (Simmons and Hoskins 1978, Thorncroft et al. 1993). The idealized baroclinic waves have a horizontal wavelength of ~3900 km. The time scale for full the synoptic features is around 3-4 days. After 72 hours, features found at the surface include a continuously deepening surface cyclone/anticyclone, strengthening cold and warm fronts, and emergence of an occluded front as part of a “T bone” structure (Shapiro and Keyser

1990). After this time, the tropopause above the surface cyclone, accompanied by a strengthening upper level jet steak, descends continuously to the lower troposphere. Weak gravity wave signals in the exit region of the upper level jet streak begin to emerge around 102h.

Figure 5.1 displays the simulated baroclinic wave at 114 h in 30-km domain. At this time, the minimum sea level pressure reaches 934 hPa; upper tropospheric jet continues to distort and has the maximum wind speed over 45 m/s at 8 km; several distinct gravity wave bands appear at 13 km in the vicinity of the 8-km jet streak. This figure is the same as Fig. 1 in LZ08.

Figure 5.2 shows zoomed-in-views of the vertical velocity at 13 km and the corresponding vertical cross sections from the 30-km domain output. Figure 5.2 (a) and (b) are the MM5 simulated vertical velocity. The wave packet at low stratosphere (13 km) is not monochromatic. The horizontal wavelength (Fig. 5.2 a) changes from ~ 500 km at the west end of the wave packet to ~ 250 km at the east end. Wang and Zhang (2007) and Lin and Zhang (2008) demonstrated that these wave packets have multiple components with different wave characteristics. These two studies analyzed the wave characteristics from the 10-km MM5 output and concluded that the wave packets may

have two components: one is the shorter scale component that is preserved by a high pass filter with cut-off wavelength 200 km, and the other is the medium scale component that is preserved by a band pass filter with cut-off wavelength 200 and 600 km. Here, 2D digital filters are also applied to the MM5 simulated vertical velocity at the horizontal resolution of 30 km. Figure 5.2 (c) and (d) are filtered w that are preserved by a high pass 2D filter with a cut-off wavelength of 400 km. Panel (e) and (f) are filtered w that are preserved by a band pass 2D filter with cut-off wavelength 400 km – 600 km. Wave packet in Fig. 5.2 c have a horizontal wavelength ~ 300 km after applying a high pass filter, but ~ 450 km after applying a band pass filter (Fig. 5.2 e). These horizontal wavelengths are different from those estimated values from the 10 km domain output in WZ07. For example, the horizontal wavelength at 13 km in the 30 km domain is ~ 300 km, which is larger than that (~150 km) in the 10 km domain. This resolution dependence of horizontal wavelength of wave parameters is not surprising. This has been discussed by Plougonven and Snyder (2007).

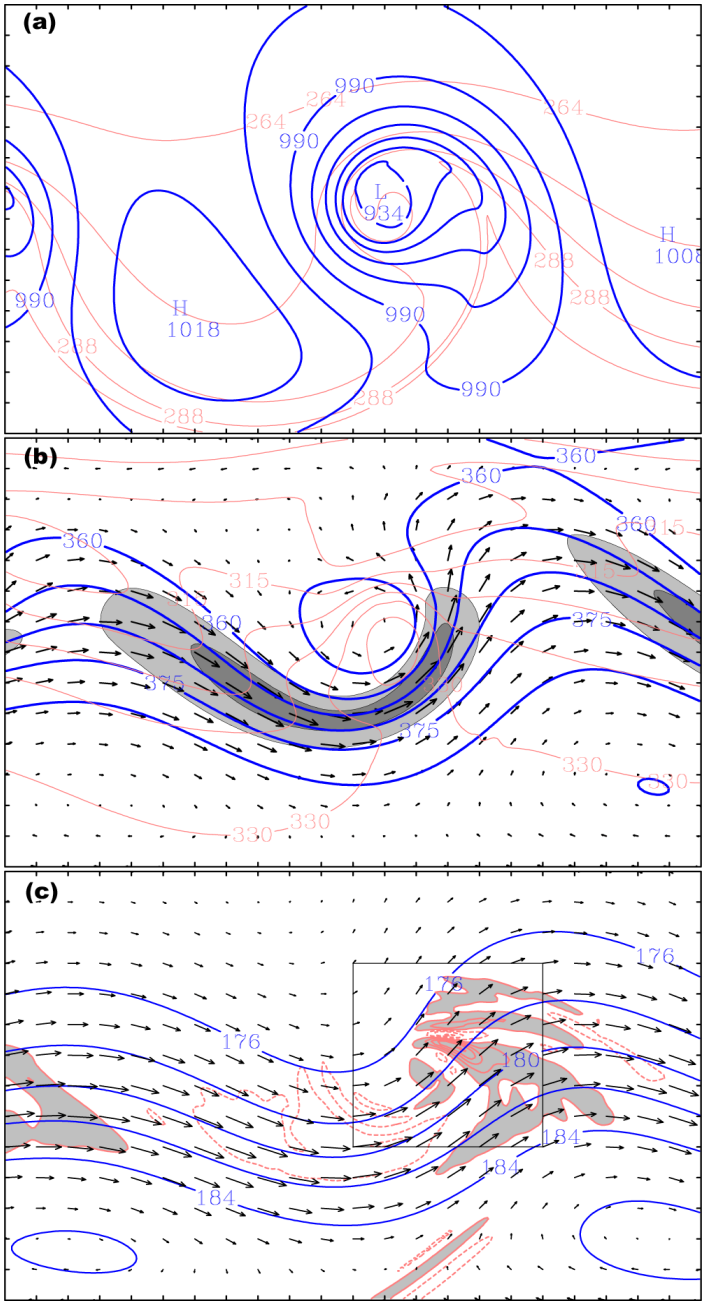

Figure 5.1 The CNTL of Z04 simulated (a) surface potential temperature (thin line, Δ = 8 K) and sea level pressure (thick line, Δ = 10 hPa), (b) 8-km pressure (thick line, Δ = 5 hPa), potential temperature (thin line, Δ = 8 K) and winds (maximum of 50 m s^{-1}, values greater than 40 shaded, ci = 5 m s^{-1}), and (c) 13-km pressure (thick line, ci = 2 hPa), the horizontal divergence (thin line; solid and shaded, positive; dashed, negative; ci = 2 × 10^{-6} s^{-1}) and wind vectors (the maximum 25 m s^{-1}) valid at 114 h. The distance between tick marks is 300 km.

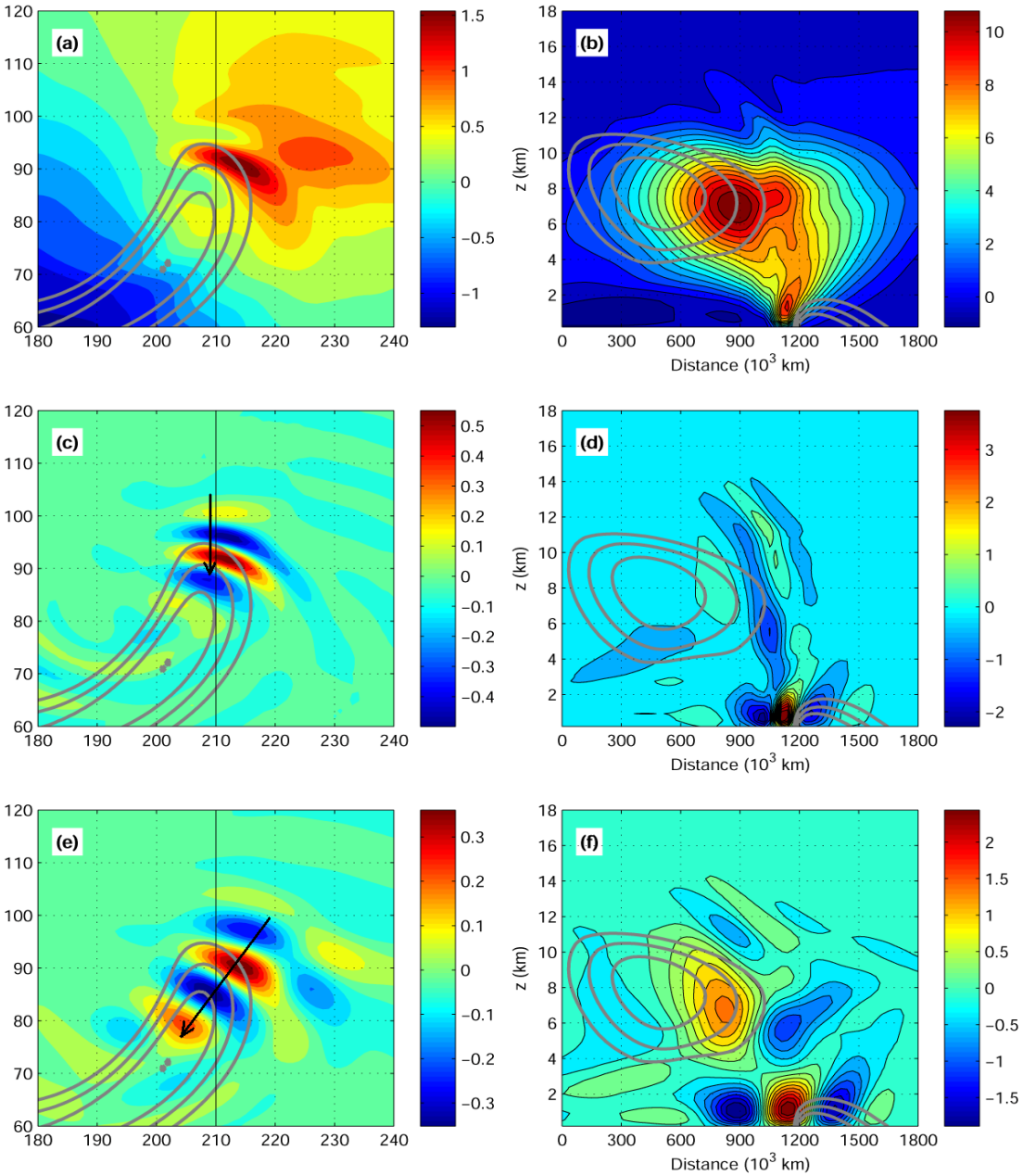

Figure 5.2 Zoomed-in views of the simulated vertical velocity (cm/s) (a) at 13 km and (b) the cross section indicated by the dash line in (a). Panels (c), (d), (e) and (f) are similar to (a) and (b) except that filtered w is plotted. (c) and (d) are filtered w after applying a high pass filter. (e) and (f) are filtered w after applying a band pass filter. Wind speed (solid, 40, 45, 50 m/s) at 8 km and along the cross sections is plotted in each panel. The distance between adjacent ticks is 300 km in (a), (c) and (e). The arrows in (c) and (e) indicate the wave vector orientation.

The roughly estimated intrinsic frequencies of the filtered two wave components are *3.6 f* and *2.5 f*. These values are close to the estimated values from 10 km MM5 simulation in WZ07 for shorter scale wave component ~3.7 *f* and for medium scale wave component ~2.8 *f*. Therefore, the wave intrinsic frequency is quite robust in both 30 km and 10 km simulations. This is consistent with the finding by Plougonven and Snyder (2007). These two wave components also have different wave vector orientations. The shorter scale component has the wave vector pointing due south, and are advected by horizontal wind to north; The medium scale component has the wave vector point to due southwest, and are advected by horizontal wind to northeast.

The dependence of wave characteristics on the resolution is not our focus here. Rather, this section intends to study the wave source mechanism using a linear model. All analysis will be based on the 30 km simulation.

5.3 Wave response to the forcing diagnosed from the balanced flow

Next we consider wave forcing diagnosed from the balanced fields and the corresponding wave response in the linear dynamics. The forcing diagnosis through EPV inversion is discussed first, followed by discussions on the linear response to the diagnosed forcing.

a. Balanced state from EPV inversion and forcing diagnosis

The balanced winds through the direct EPV inversion differs from the primitive equation solution in that the divergent modes in balanced state are significantly smaller than (or totally removed from) the primitive equation solution. Gravity waves are one

type of divergent modes with much small amplitudes comparing with the vortical modes such as baroclinic waves.

The EPV inversion is performed for hourly MM5 output. Gravity waves are mostly absent in the balanced state from EPV inversion. To see this, Fig. 5.3 displays the horizontal divergence at 13 km in the whole 30 km domain (D2) from both the MM5 output and the balanced state at 114 h, and the difference between these two. At 114 h, the wave packet with several distinct wave bands (Fig. 5.3 a) is absent in the balanced state (Fig. 5.3 c), which shows a large scale pattern that is in phase with the baroclinic wave and has the maximum value of $1x10^{-5}s^{-1}$. This is one magnitude smaller than that in primitive equation solution. The difference between these two (Fig. 5.3 e) is dominated by divergent modes in the MM5 solution. However, note that there is also a weak band structure in the balanced state (Fig. 5.3 c) located over the surface front. This is due to discontinuity of potential temperature associated with the surface warm front, which is used as surface boundary condition to perform EPV inversion.

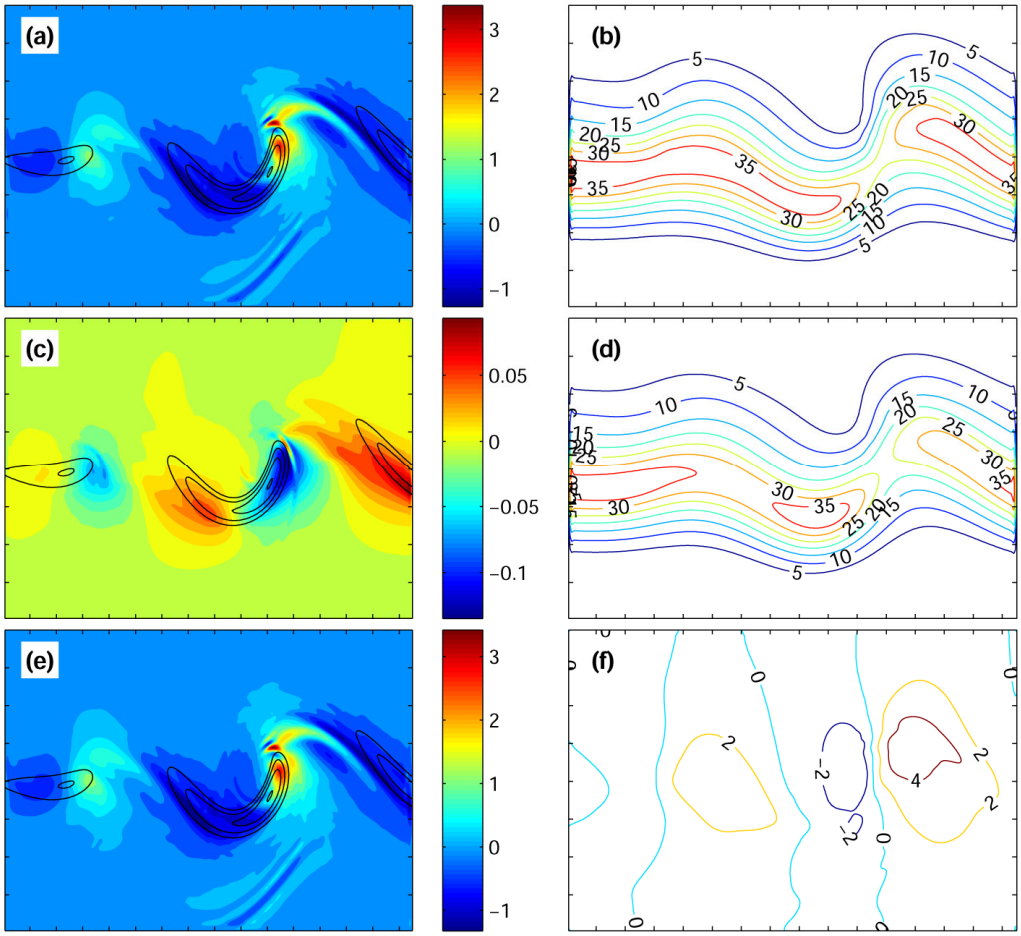

Figure 5.3 Horizontal divergence ($\times 10^{-5} s^{-1}$) at 13 km from (a) the MM5 solution, (c) the balanced state and (e) the difference between these two valid at 114 h. Zonal wind at 13 km valid at 114 h is plotted for (b) the MM5 solution, (d) balanced state and (f) the difference between them. Wind speed (solid, 40, 45, 50 m/s) at 8 km is plotted in solid contour lines (40, 45, 50 m/s) in (a), (c) and (e).

Nevertheless, difference in horizontal winds between the balanced state and the MM5 solution is relatively small. Zonal winds in MM5 solution (Fig. 5.3 e) and the balanced state (Fig. 5.3 d) are similar in both patterns and magnitudes (35 m/s). The difference of the zonal wind at 13 km in these two is at most 4 m/s, which is ~ 10 percent of the maximum zonal wind. This difference is more likely due to approximations made in the PV inversion, where total wind is approximated by the stream function and potential. As discussed in Lynch (1989) and Chen and Kuo (1992), harmonic winds in the limited domain may be neglected in this approximation.

Figure 5.3 only shows a snapshot of the difference between the balanced state and the MM5 solution. In general, the EPV inversion procedure can safely used to remove wave signatures from the background wind. Nevertheless, the balanced vertical velocity is not easy to obtain through the EPV inversion procedure. Again, the QG vertical velocity is used since gravity waves are not admitted in the QG framework. Using variables from the balanced state, it is straightforward to compute the three forcing terms and their equivalent forms.

Unlike the quasi-stationary jet in vortex dipoles, the forcing terms derived from the balanced baroclinic jet are time evolving. Their amplitudes are increasing in phase with the developing baroclinic wave. Figure 5.4 displays a snapshot of the three forcing terms F_δ, F_θ and F_ζ valid at 108 h. All small scale components have been smoothed out by applying a 2D low pass digital filter with a cut off wavelength 300 km. These forcing terms have a clean localized structure both at the upper level (8 km) and near surface (1 km). F_δ is the least important to the wave forcing, as we shall see later. Physically, F_θ is

the Lagrangian of background potential temperature, and F_ζ is the Lagrangian of background vorticity plus the Coriolis term. The Lagrangian terms can be divided into two parts: one is the local change rate of θ, ζ, and the other part is the advection by the background winds. It turns out that the advection parts dominate the rest. Thus it is not surprising that strong horizontal advection by the jet low contributes the formation of the localized spatial structures of F_θ and F_ζ near the jet streak. Note that almost all forcing terms have banded structures near the surface. This comes from the surface front. Also wind speed has additional maximum near the northwest end of the surface warm front.

The derived forcing terms G_δ, G_θ, G_ζ and their sum at 108 h are displayed in Fig. 5.5. G_δ varies from -0.1 to 0.1 ($\times 10^{-16} m^{-1} \cdot s^{-3}$). G_θ and G_ζ vary from -15 to 5 ($\times 10^{-16} m^{-1} \cdot s^{-3}$). At 8 km, their sum $G_\delta + G_\theta + G_\zeta$ (Fig. 5.5 h) has spatial structure almost the same as G_θ, indicating that G_θ is the largest forcing terms among the three. This is different at the surface where G_ζ (Fig. 5.5 d) appears to be the largest among the three. The sum $G_\delta + G_\theta + G_\zeta$ (Fig. 5.5 h) is determined by both G_θ and G_ζ. It is also interesting to notice that the total (G_δ+G_θ+G_ζ) is larger near the surface than that at the upper level (cf. Fig. 5.5 g and h). Nevertheless, these forcing terms are evolving on the time scale of inertial period in terms of their scale and amplitude. It is not easy to find a localized spatial structure, such as a quadruple pattern within the dipole flow that might be responsible for wave generation.

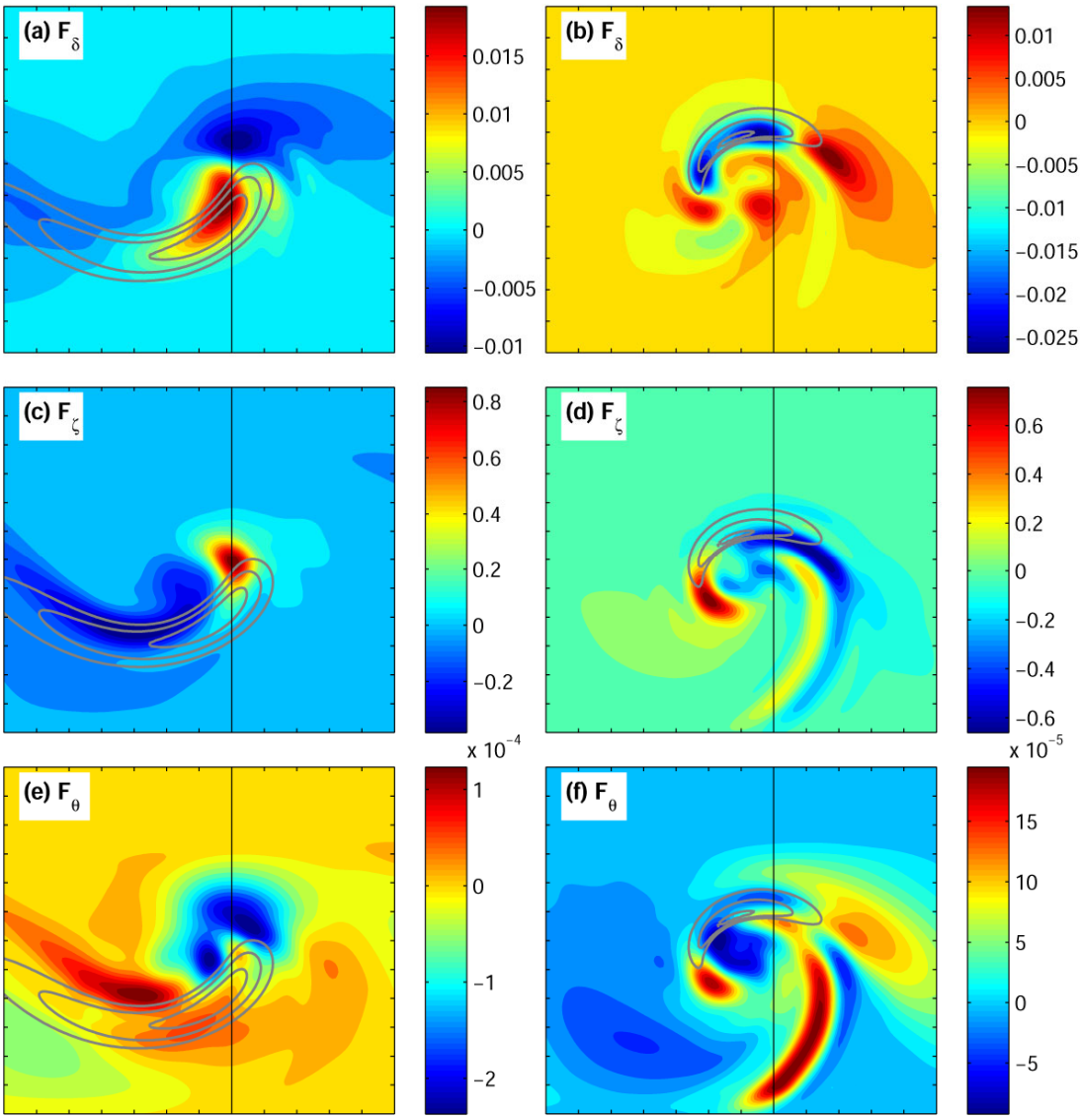

Figure 5.4 Three forcing terms F_δ, F_θ and F_ζ at 8 km (the left column) and 1 km (the right column). Wind speed (40, 45, 50 m/s) is also plotted on each panel. F_δ and F_ζ have a unit $1\times10^{-8} m\cdot s^{-2}$. F_θ has a unit $1 K\cdot s^{-1}$.

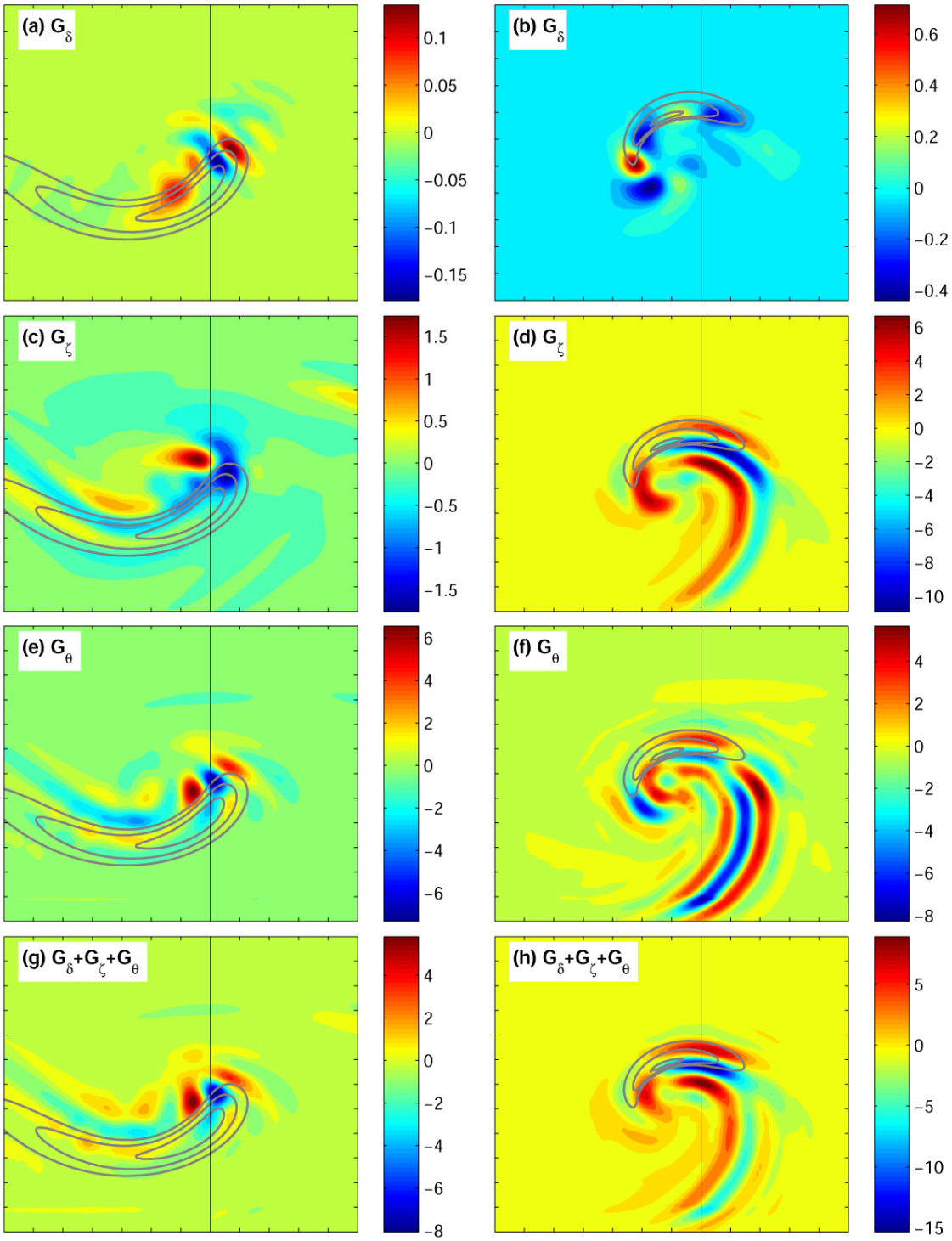

Figure 5.5 Three individual forcing terms G_δ, G_θ and G_ζ and their sum plotted at 8 km (the left column) and 1 km (the right column). Wind speed is contoured at 40, 45, 50 m/s in each panel. All derived forcing terms have a unit of $1\times10^{-16} m^{-1}\cdot s^{-3}$.

The surface front is the most ambiguous source of wave generation in the baroclinic jet-front systems, as has been extensively discussed by Z04 and LZ08. Large values of these forcing terms near the surface thus suggest that the surface front plays important roles in wave generation. Nevertheless, analysis from the forcing alone can not be relied to deduce the contribution of the surface front and the upper level jet/front to waves seen in low stratosphere. In the following, results from our linear model experiments will be discussed.

b. Wave response from the linear model

Here, we are not seeking a steady state solution for reasons discussed in the introduction part. Instead, linear response is solved by integrating the linear model from certain initial time with zero initial conditions. Both the forcing and the background state are allowed to change with respect to time. To remove small scale wave components possibly contained in the forcing terms, a low pass filter with the cut-off wavelength 360 km is applied to all forcing terms. The linear model ingests both the smoothed forcing terms and the balanced winds at each hour to allow a time-evolving background wind and the forcing terms. The temporal jump of both forcing terms and the background winds may cause some inaccuracies here. This is not a serious issue since our purpose here is to understand wave source mechanism but not to investigate numerical accuracy.

The linear model is driven by the forcing terms F_δ, F_θ and F_ζ and integrated from 102 h to 114 h. The initial conditions at 102 h for the linear model are zero for all prognostic variables. Wave absorbing sponge layers are added near the lateral and top boundaries. The 3D rectangular domain for linear model is only slightly smaller than 30

km domain of MM5 (D2), having a dimension of 250x155x60 grid points and horizontal (vertical) grid resolution 30 (0.367) km. The chosen initial time 102 h is sufficient since linear response at later time (e.g., 114 h) is insensitive to the initial time of the linear model.

Figure 5.6 shows the vertical velocity at 13 km and along the vertical cross sections to the all the forcing terms and each forcing term. This experiment refers to ALF. Linear response in ALF (Fig. 5.6 a and b) shows clear wave pattern in the exit region of the jet streak. Comparing with wave pattern in Fig. 5.2, the vertical velocity has maximum value of 1.5 cm/s, which is larger than that in the MM5 simulations (1 cm/s in Fig. 5.2 a and c). Linear response to each individual forcing term is also computed. These three experiments refer to VOR, DIV and THE. Figure 5.6 c and d show the response to the thermodynamic forcing (THE) at 114 h, e and f show the response to the vorticity forcing (VOR), and g and h show the response to the divergence forcing (DIV). Among these three, magnitude of the wave packet in DIV is the smallest, while wave packets at 13 km in VOR and THE have similar magnitude. The sum of these three responses to individual terms equals to the response to the all forcing terms in Fig. 5.6 a and b, which is consistent with the linear assumption.

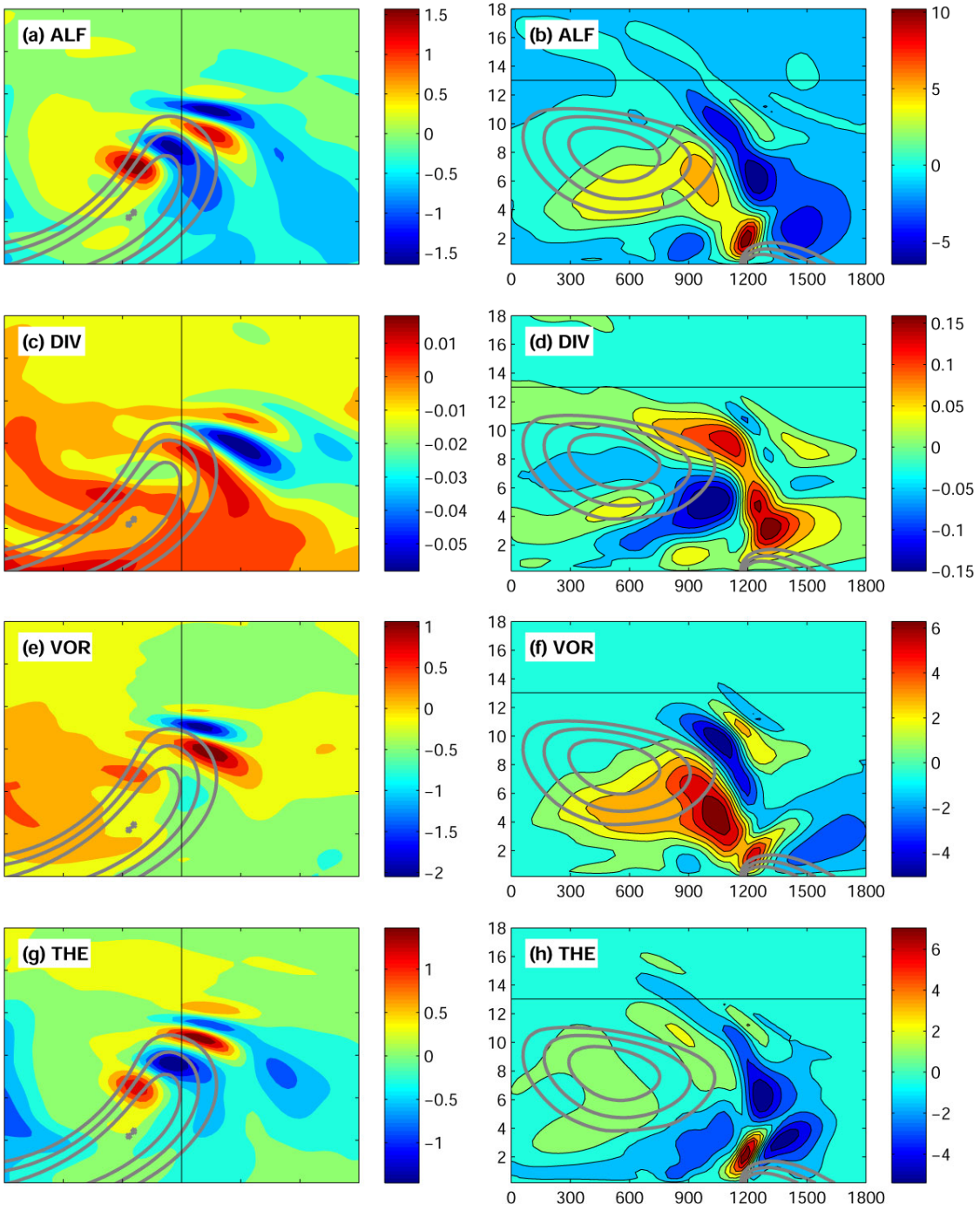

Figure 5.6 Vertical velocity at 13 km and wind speed (40, 45, 50, 55 m/s) at 8 km in (a) for ALF, (c) for DIV, (e) for VOR, and (g) for THE. The corresponding right column shows the vertical velocity and wind speed along the vertical planes indicated by the solid lines in the left column. Vertical velocity has a unit of 1 cm/s.

The magnitude of the wave packet varies from -2 cm/s to 1 cm/s in VOR (Fig. 5.6 e), and varies from -1.5 cm/s to 1.5 cm/s in THE. This similarity of wave amplitude in VOR and THE (Fig. 5.6 e and g, f and h) suggests that the vorticity forcing appears to be equally important to the thermodynamic forcing. Despite this amplitude similarity in VOR and THE, their wave pattern and horizontal wavelengths at low stratosphere (13 km) are different. The wave packet in response to F_θ has a shorter horizontal wavelength ~ 300 km, while the wave packet due to F_ζ has a larger horizontal wavelength ~ 450 km. It is not surprising to see that wave response in DIV is small since the horizontal divergence is much smaller after performing EPV inversion (Fig. 5.3 a and c). This is consistent with the usual assumption that rotational modes dominates over divergent modes in the balanced states for synoptic flow.

To further determine the contribution of surface front, the forcing terms are split into two parts: one is the surface part having the forcing terms above 4 km quickly decrease to zero and the other is the mid/upper tropospheric part having the forcing terms below 4 km quickly decrease to zero. An exponential decaying function is used to split these forcing terms. For instance, the surface forcing part F_ς^s of the forcing term F_ζ is set to $F_\varsigma \cdot \exp(-(z-4)^2)$ if z < 4 km, and F_ς if z > 4 km. This splitting is repeated for all four experiments (ALF, VOR, THE and DIV) (in Fig. 5.6). Thus eight additional linear model experiments are performed. Table 5.1 summarizes the four experiments described above and these eight experiments. ALFup and ALFdn refer to the experiments forced by all forcing terms, which are split into surface part and mid/upper tropospheric part. Similarly, VORup and VORdn refer to the experiments forced by F_ζ

that is split into surface and mid/upper tropospheric part, THEup and THEdn refer to the experiments forced by F_θ that is split into surface and mid/upper tropospheric part, and DIVup and DIVdn refer to the experiments forced by F_δ that is processed by splitting in a similar way.

Table 5.1. Twelve linear model experiments with different forcing terms. 'X' indicates the experiment has the corresponding forcing term or the forcing terms are processed with the corresponding splitting.

	F_δ	F_ζ	F_θ	> 4 km	< 4 km
ALF	X	X	X		
THE			X		
VOR		X			
DIV	X				
ALFup	X	X	X	X	
ALFdn	X	X	X		X
THEup			X	X	
THEdn			X		X
VORup		X		X	
VORdn		X			X
DIVup	X			X	
DIVdn	X				X

In most of these eight experiments, wave packets are found in the vicinity of the jet streak in the lower stratosphere (13 km), although wave phases and even the horizontal wavelengths simulated in these linear model runs do not match exactly the 30 km simulation from MM5. In general, wave packets have wave vectors pointing south in the "dn" experiments (ALFdn, THEdn, VORdn, DIVdn) when only near surface contributions are considered, while wave vectors appear to point southwest in the "up" experiments (ALFup, THEup, VORup, DIVup) when surface contribution is removed.

Also, horizontal wavelengths at 13 km are smaller (~300 km) in the “up” experiments than those (~ 450 km) in the “dn” experiments. Wave packets have an estimated horizontal wavelength 450 km in ALFup (Figs. 5.7 a and 5.8 a) and 300 km in ALFdn (Fig. 5.7 b). In terms of horizontal wavelengths and the wave vector orientation, wave packets in THEup and THEdn are similar to ALFup and ALFdn. Wave packets in both THEdn (Fig. 5.7 h) and VORdn (Fig. 5.7 f) appear to have similar wave vector orientation. Horizontal wavelengths in THEdn and VORdn both have horizontal wavelength ~ 300 km at the leading edge at 13 km, but their phase are different. Wave packets are not clearly defined in VORup but have a few distinct phases in VORdn. Thus the vorticity forcing mostly comes from the surface contribution due to the surface front. The contribution of the thermodynamic forcing from surface and middle/upper troposphere are both important. Finally, wave packets in DIVdn and DIVup are at least one magnitude smaller in comparison with wave packets in all other experiments, and wave vectors point south in DIVdn and southwest in DIVup.

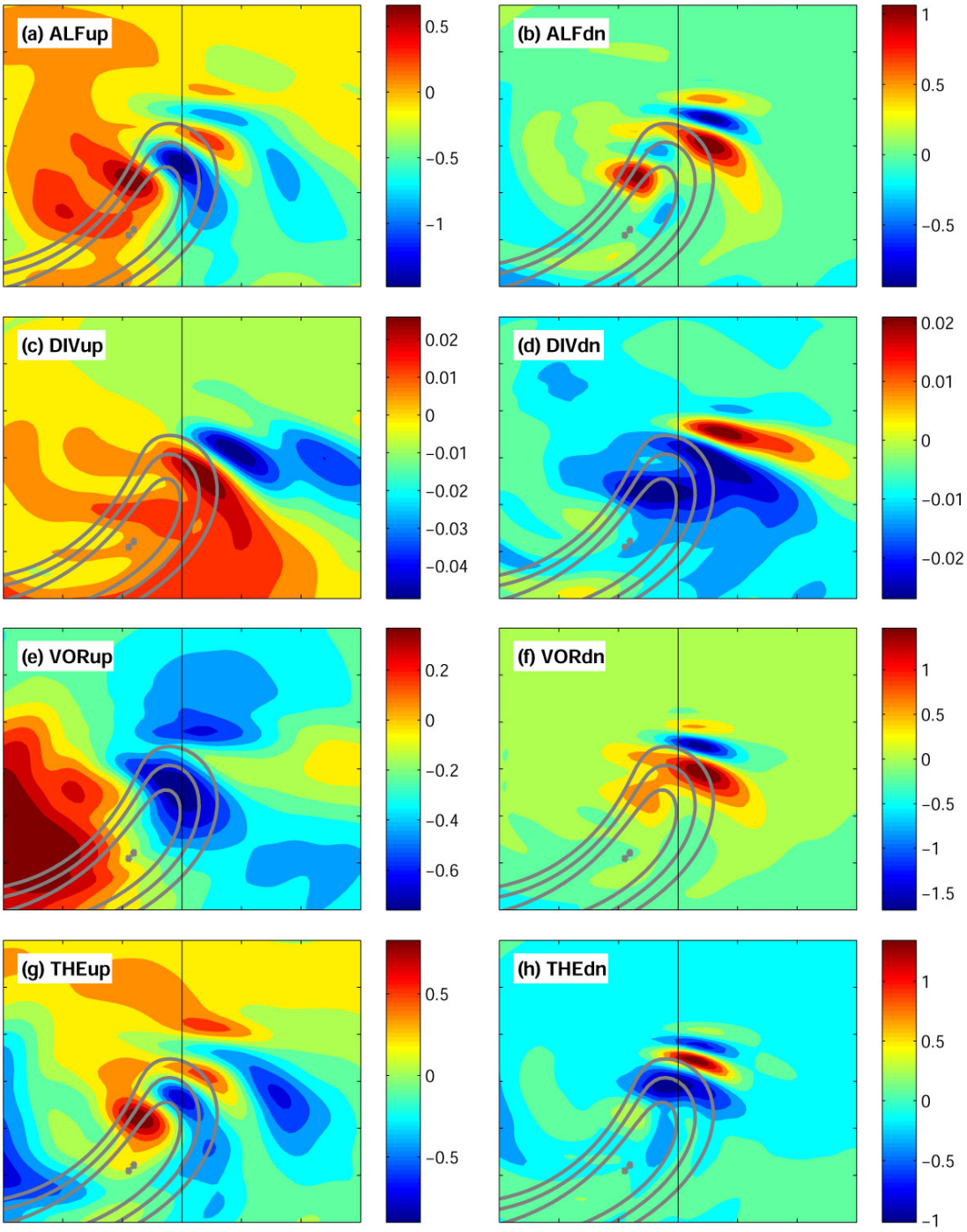

Figure 5.7 Vertical velocity at 13 km and wind speed (40, 45, 50, 55 m/s) at 8 km in the experiments for (a) ALFup, (b) ALFdn, (c) DIVup, (d) DIVdn, (e) VORup, (f) VORdn, (g) THEup and (h) THEdn.

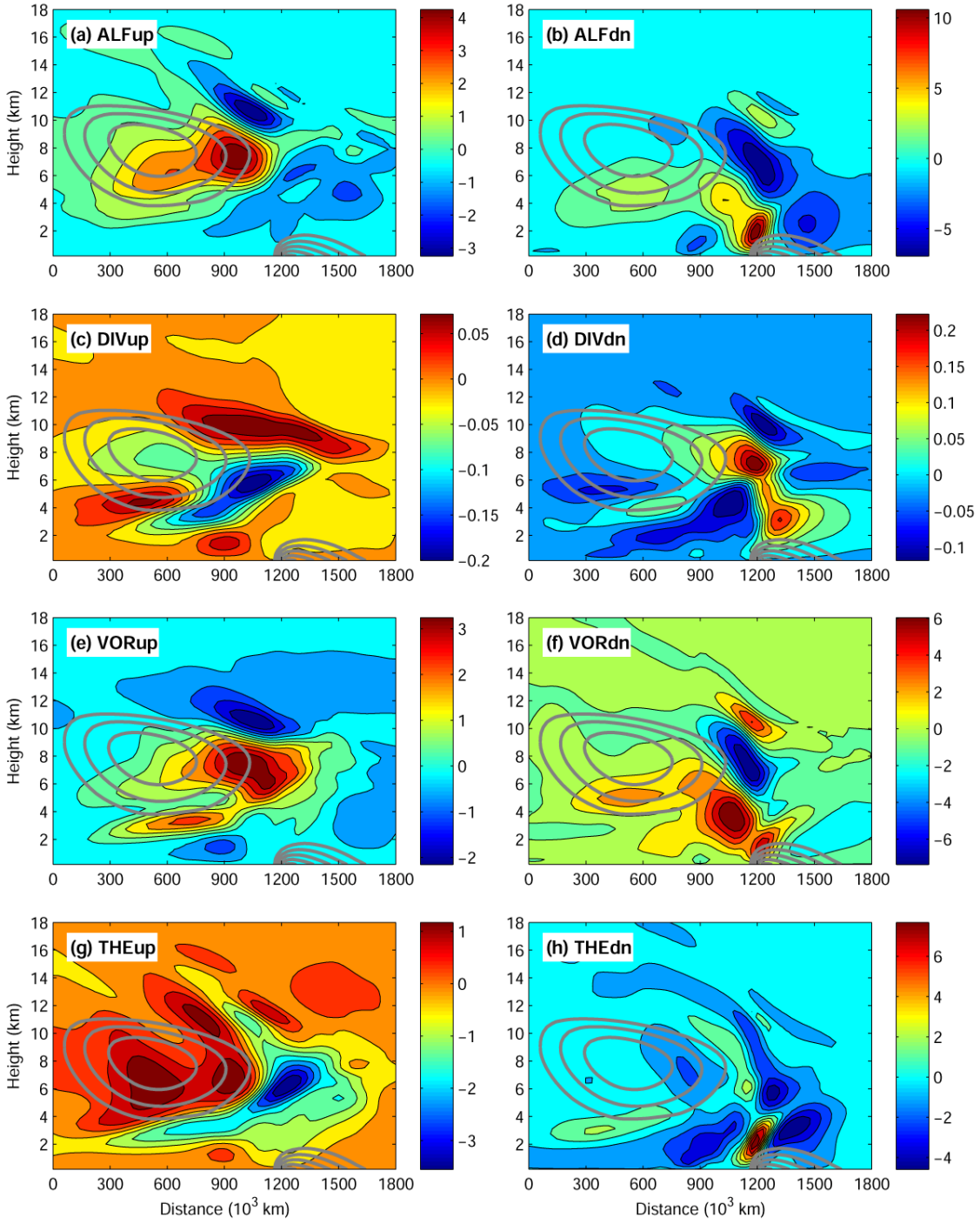

Figure 5.8 The same as Fig. 5.7 except that the vertical velocity and wind speed is plotted along the vertical plane indicated in the corresponding panel in Fig. 5.7.

The wave packet in ALFdn (Fig. 5.7 b) seems to originate from the surface front; comparing Fig. 5.7 b, f and h suggests that the surface front contributes to wave generation through the vorticity forcing, because the spatial pattern of the wave packet in ALFdn resembles closely to that in VORdn. On the contrary, the wave packet in ALFup (Fig. 5.7 a) seems to originate from the upper level jet/front; comparing Fig. 5.7 a, e and g suggests that the upper level jet/front contributes to wave generation through the thermodynamic forcing, because the spatial pattern of the wave packet in ALFup (Fig. 5.7 a) is more close to that in THEup (Fig. 5.7 g) and have a wave vector point southwest. In all, these linear model experiments suggests that forcing near the surface due to front is responsible for shorter scale waves observed in the low stratosphere (e.g.13 km), forcing in the middle/upper troposphere near the jet/front system is responsible for medium scale waves. Both the vorticity forcing and the thermodynamic forcing are important for the shorter scale waves having the wave vector pointing to south.

We argue that the south pointing shorter scale (~300 km) waves in ALFdn correspond to the shorter scale wave analyzed in WZ07, while the southwest pointing medium scale (~450 km) waves in ALFup correspond to the medium scale wave components. Note that here horizontal grid spacing is 30 km while waves analyzed in WZ07 and LZ08 is 10 km, which likely leads to the difference between the horizontal wavelengths for wave packets at 13 km in Figs. 5.7 and 5.8 and the results in WZ07. On the other hand, ray tracing analysis in LZ08 suggests that the medium scale waves in 10 km domain seems to originate from the jet/front system in the middle/upper troposphere,

while the shorter scale wave likely originates from the surface. Our linear model results are also consistent with LZ08's ray tracing results.

5.4 Wave response to flow imbalance ΔNBE

In order to assess the role of flow imbalance on the wave generation, wave response to the *ΔNBE* residual is computed using the linear model. The linear model driven by *ΔNBE* is integrated from 90 h to 114 h. The forcing terms are computed at each hour starting from 90 h. The flow imbalance ΔNBE is suggested by Z04 to be responsible for gravity wave generation. In the control simulation, ΔNBE has a localized structure near the tropopause level (6-8 km, details in his Figs. 10-11). Around 78 h, an area of imbalance (with *ΔNBE* greater than $0.5 \times 10^{-9} s^{-2}$) appears. This area of flow imbalance continues to expand with growing magnitude. Around 102h, the maximum of *ΔNBE* increased almost 400%, and weak gravity wave signals begin to emerge in the *ΔNBE* field in the exit region of the upper level jet streak. Thus, the location and timing of flow imbalance appears to indicate this gravity wave event.

Figure 5.9 displays the vertical velocity at 102 hour in panels a and c, and 114 hour in panels b and d. The linear model is integrated from 90 h. After 13 hours of integration, there are no apparent wave packets at 102 h. This is also consistent with the MM5 solution. However, several distinct wave bands gradually appear in the exit region of the jet streak. The roughly estimated horizontal wavelength at 114 h is ~ 450 km. The vertical wavelength estimated from the tilted bands in panel (d) is ~2.5 km. The estimated wave frequency is about 2.5 *f*. The wave magnitude is twice larger than that in the MM5 simulation (Fig 5.2. b and d). These wave packets do not match contour by

contour the medium scale waves that are discussed in WZ07. Neither do these waves match the linear response to all forcing terms (Fig. 5.6 a and b, the ALF experiment), or response to upper level forcing (Fig. 5.7 a and b, the ALFup experiment). The reason for this difference remains unknown. However, the wave frequency are close to the medium scale waves (2.8 *f*) estimated by WZ07 and LZ08. This linear model experiment suggests that the ΔNBE residual help generating gravity waves having small intrinsic frequency (< 3 *f*) and large horizontal wavelength (> 400 km). The ray tracing analysis by LZ08 also suggests that the origin of the medium scale waves located near the upper level jet front systems. Since the localized structure is clearly located at mid levels (from 4 to 9 km in Fig. 11 in Z04), the wave from the ΔNBE residual in this case seems to be consistent with the ray tracing analysis performed in LZ07.

In order to separate the surface contribution, the forcing terms are allowed to decrease smoothly to zero below 4 km. The wave pattern in the low stratosphere is almost unchanged (not shown). This test suggests that the 450 km waves generated by the NBE residual are not affected by the surface front.

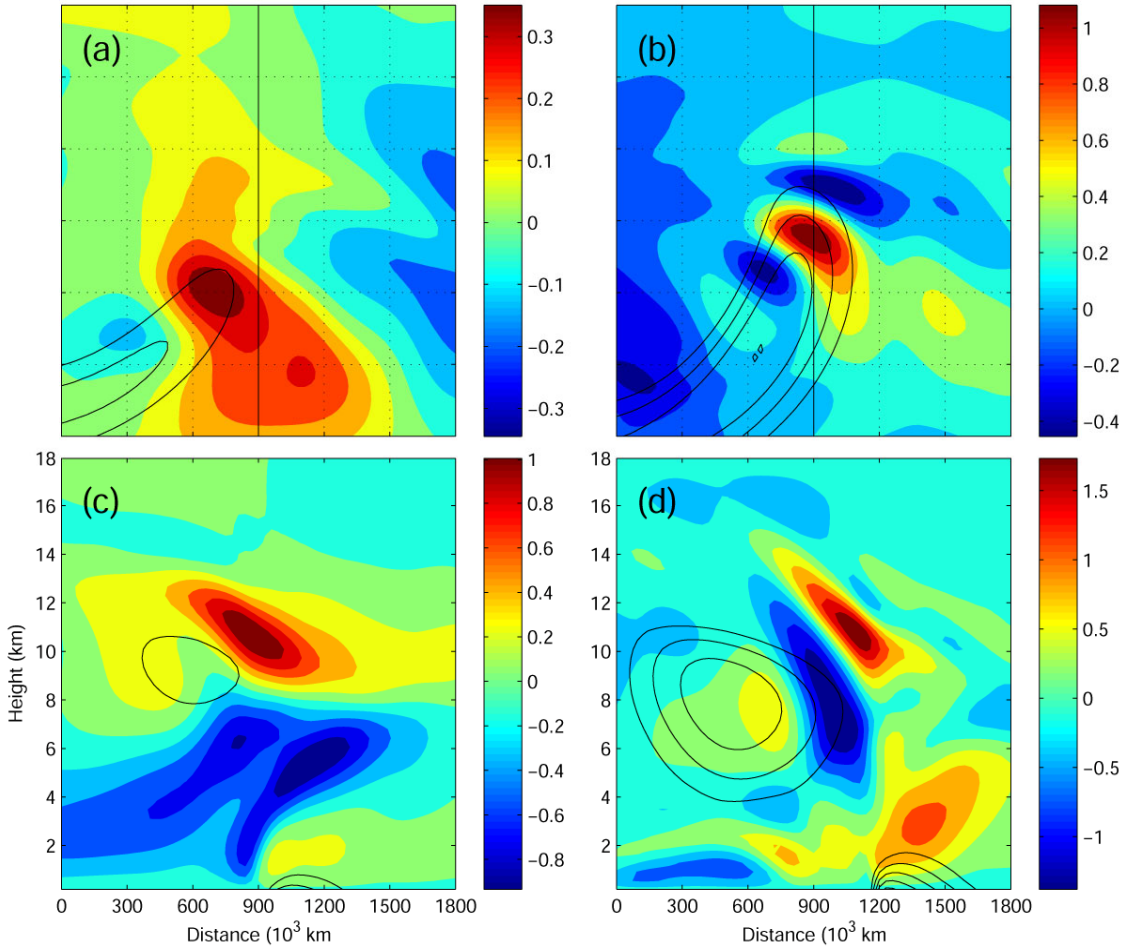

Figure 5.9 Vertical velocity valid at 102 h in panels (a) and (c) and at 114 h in (b) and (d). Vertical velocity is plotted in (a) and (b) at 13 km, and in (c) and (d) along the vertical cross sections indicated by the corresponding solid line in upper panels. Wind speed (solid, 40, 45, 50 m/s) at 8 km and along the cross sections is plotted in each panel. The distance between adjacent ticks is 300 km in (a) and (b).

5.5 Summary

This section investigates the linear dynamics of gravity waves in the vicinity of a baroclinic jet during the life cycle of an idealized baroclinic wave (Zhang 2004). Different from the primitive equation approach, a linear model driven by relevant forcing is employed to study wave origins. Three types of forcing formulated in Plougonven and Zhang (2007) is considered in the linear model: the divergence forcing, the vorticity forcing and the thermodynamic equation. These forcing are enforced to the corresponding disturbance equations. Wave packets are found in the jet exit region in the linear model solution, although they do not match in detalis the 30 km MM5 solution.

The linear model results suggest the following. First, the vorticity forcing and the thermodynamic forcing are equally important for waves in low stratosphere; the forcing to the divergence equation plays a lesser role. Second, two groups of wave packets are present in the linear responses, one is the shorter scale wave having horizontal wavelength ~ 300 km and the wave vector pointing south, the other is the medium scale wave having horizontal wavelength ~ 450 km with the wave vector pointing southwest. Forcing near the surface due to surface front is responsible for shorter scale waves, forcing in the middle/upper troposphere near the jet/front system is responsible for medium scale waves. The origin of these shorter scale and medium scale waves seems to be consistent with ray tracing analysis in Lin and Zhang (2008). Finally, flow imbalance (the residual of the nonlinear balance equation) can generate waves in the exit region of the baroclinic jet with more significant phase errors. This result suggests ΔNBE can also be used as a predicator of gravity wave events, as well as a flow imbalance indicator.

We have only looked at the possible origins of the jet exit region waves in this section. However, we have not discussed several other wave packets that appear in baroclinic life cycles (Lin and Zhang 2008; Plougonven and Snyder 2007). The shorter scale wave packet in the deep trough in Lin and Zhang (2008, their Fig. 2) are not well represented by the current linear model at a horizontal resolution of 30 km. It is also possible that this wave packet is smoothed out by the filter in the forcing computation. Plougonven and Snyder (2007) documented the wave packet at upper levels downstream of the ridge and upstream trough (their Fig. 3). This wave packet appears in very late time (168 h) of the baroclinic life cycle. Since the simulation in Zhang (2004) also does not capture this wave packet at a much earlier time (114h), it is reasonable that the linear model does not produce wave responses similar to the wave packet discussed in Plougonven and Snyder (2007). We suggest that our linear model can also be a valuable tool for future investigations of the origins of these different wave packets.

6. SUMMARY AND CONCLUSIONS

This doctoral study represents an effort to systematically explore the source mechanisms of gravity waves spontaneously generated in the vortical flow. This dissertation first documents inertia-gravity waves appearing in the exit region of localized jet within vortex dipoles. The source mechanism of such waves is revealed by a linear model analysis. The linear model approach is further employed to investigate the source mechanism of inertia-gravity waves in the exit region of a baroclinic jet.

Gravity wave generation and propagation from idealized vortex dipoles and jets are investigated with a nonhydrostatic, compressible mesoscale model. In all dipole simulations, a localized jet arises between the vortex pairs and inertia-gravity waves with intrinsic frequencies 1-2 times the Coriolis parameter appear in the jet exit region when the Rossby number of the flow is sufficiently large. The gravity waves of interest are nearly stationary with respect to (or phase-locked with) the localized jet. Gravity waves in the surface dipole are quite similar to those simulated in Snyder et al. (2007), while waves in the mid-level dipole are more pronounced near the anticyclone, similar to Viúdez (2008). Gravity waves in the exit region of the localized dipole jet are long living and evolve on the time scale of many inertial periods. It is unlikely that these waves are generated due to initial imbalance through well known geostrophic adjustment processes. Instead, these waves are likely forced response. Analysis suggests that the preferred appearance of gravity waves in these dipoles is due to the occurrence of the localized jets and their exit region. The phase locking between the jet and gravity waves

suggests that the localized jet spontaneously forces these waves. Nevertheless, a full understanding of the wave generation can not be obtained only from primitive model simulations.

Two issues concerning the simulated gravity waves are also discussed: the propagation effects and the wave amplitude dependence on the Rossby number. The propagation effects are recently suggested to play an important role in determining the gravity wave characteristics. Our WKB ray-tracing analysis demonstrates that background winds strongly constrain the variation of wave characteristics along the ray paths: the horizontal and vertical wavelengths both decrease, the intrinsic frequency approaches the inertial frequency, and the intrinsic phase speed and vertical group velocity decrease toward zero.

The dependence of wave amplitude on the jet strength, and thus the Rossby number, is also examined through distant-dipole experiments. The amplitude of stationary gravity waves from these simulations increases approximately with the square of the Rossby number when a 90-km grid spacing is used, but the rate of increase with Rossby number is noticeably larger when a smaller grid spacing is used. The resolution sensitivity is likely due to the fact that smaller scale waves with stronger amplitude appear in the leading edge of the wave front in the higher resolution simulation.

To further address the source mechanism of gravity waves within the vortex dipole, linear analysis is adopted and a linear numerical model is developed. The linear model is based on the analysis by Plougonven and Zhang (2007). It is essentially of WKB type since all shear terms such as those involving advection by perturbation winds

have been neglected. This linear model is driven by the forcing diagnosed from the large scale balanced flow. Three types of forcing are considered in the linear model: the divergence forcing, the vorticity forcing and the thermodynamic forcing. These forcing terms are diagnosed from balanced flow that is obtained by potential vorticity inversion, and enforced to the linear disturbance equations. It is found that for gravity waves from the localized jet in the vortex dipole the vorticity forcing is one magnitude larger than the other two and shows a quadruple pattern. Results from the linear model suggest that the vorticity forcing is the leading contribution to both gravity waves in the jet exit region and the ascent/descent couplet in the jet core. Sensitivity experiments demonstrate that the wave pattern from the linear model is a robust feature.

Based on the wave forcing diagnosis and linear model solutions, a wave generation scenario is also suggested: the large scale forcing diagnosed from the balanced flow first induces the large scale response (compared with that of gravity waves) in the form of ascent/descent couplet below and above the jet; the jet flow passing the ascent/descent couplet naturally generate vertically propagating gravity waves. The localized jet is characterized by a sufficiently large Rossby number and is important for both wave generation and wave propagation. On the one hand, the horizontal advection of the large scale vorticity due to the jet flow leads to the quadruple pattern in the vertical velocity seen in the vertical velocity fields in the diagnosed forcing and the wave response. On the other hand, the horizontal shear and vertical shear of the jet flow strongly constrains wave characteristics due to propagation effects.

The residual of the nonlinear balance equations is hypothesized in several studies to provide the wave forcing. This idea is tested with the linear model. Linear model produces steady wave responses to ΔNBE with similar spatial pattern to the wave solutions of MM5 simulated vortex dipoles, but with wave phase reversed. Despite the phase difference, it seems that ΔNBE, as a flow imbalance indicator, can be safely used as a gravity wave predicator.

Linear model approach is also adopted to study inertia-gravity waves in the vicinity of a baroclinic jet during the life cycle of an idealized baroclinic wave (Zhang 2004). Despite some phase and amplitude errors, wave packets are found in the jet exit region in the linear model solutions with a horizontal resolution of 30 km. The linear model results suggest the following. First, the thermodynamic forcing and the vorticity forcing are equally important to waves in low stratosphere, but the divergence forcing plays a lesser role. Second, two groups of wave packets are present in the linear response, one is the shorter scale wave having a horizontal wavelength ~ 300 km and the wave vector pointing south, the other is the medium scale wave having a horizontal wavelength ~ 450 km with the wave vector pointing southwest. Forcing near the surface due to surface front is responsible for shorter scale waves, forcing in the middle/upper troposphere near the jet/front system is responsible for medium scale waves. The scale separation of these waves seems to be consistent with Wang and Zhang (2007). The origin of these shorter scale and medium scale waves seems to be consistent with the ray tracing analysis in Lin and Zhang (2008).

It is worth noting that several dynamical simplifications have been made to achieve numerical efficiency of the linear model. First, a Boussinesq approximation enables to treat the geopotential height in a way similar to dynamic disturbance pressure. Second, all shear terms such as those involving advection by perturbation winds are neglected according to scale analysis. These simplifications no doubt affect the numerical accuracy of the linear model. Nevertheless, the linear model results are surprisingly in reasonable good agreement of the primitive equation solution. As for the phase errors of wave packet in the linear model, numerical inaccuracy may come from a few places. 1. Balance state computation through potential vorticity inversion. 2. The use of the quasi-geostrophic vertical velocity as the balanced vertical velocity. 3. The Boussinesq assumption of the linear model. 4. Rounding error of finite difference schemes.

Several issues remain to be addressed in the future. 1. We have not explored the impact of turbulent mixing and diffusion on small scale gravity waves. The mixing and diffusion effects are parameterized currently as the coefficients of the model diffusion operator in the NWP models. In the linear model, it is simply an artificial smoothing operator. In practice, wave propagation will likely contract the horizontal wave scale. As such, turbulence and mixing will eventually play a role. This also raises the question of numerical convergence of gravity wave simulation. However, the numerical convergence problem requires considerable numerical efforts and enormous computation resources. 2. Results in this study do not fully answer the following question: between the propagation effects and the source mechanism, which one is important to determine

wavelengths away from wave sources? From the experiments with prescribed forcing within the vortex dipoles, it is suggested that the scale of the forcing does not monotonically determine the wavelengths at high levels. But for waves from the baroclinic jet, no experiments have been conducted. 3. Amplitude dependence of simulated gravity waves on Rossby number does achieve numerical convergence when different horizontal resolutions. This is partly due to the unsolved issue of mixing and diffusion effects. 4. Nonhydrostatic forcing is not included in the linear wave operator. It is assumed that both large scale flow and gravity waves have a large aspect ratio, i.e. their horizontal scale is at least one magnitude larger than their vertical scale. Although nonhydrostatic effects are not an issue for the long waves, they are certainly important for short scale nonhydrostatic waves. 5. Wave solutions in the slowly developing distant vortex dipoles have not been obtained from the linear model. A better estimate of the wave amplitude dependence on the Rossby number may be obtained from the linear wave responses in the linear model. Also, there exists a flow regime (Snyder et al. 2007) that propagating waves can not be found in the primitive equation solutions if the localized jet is too weak. This flow regime has not been explored. Finally, it should be noted spontaneous gravity wave generation is only investigated in two types of vortical flow: vortex dipoles and baroclinic waves. Although the linear model results seems to be the very promising, the effectiveness of current linear model approach is limited to a relative simple idealized flow. Broad application of this linear model remains to be investigated.

REFERENCES

Alexander, M. J., J. R. Holton, and D. R. Durran, 1995: The gravity wave response above deep convection in a squall line simulation. *J. Atmos. Sci.*, **52**, 2212–2226.

American Meteorological Society, 1999: *Glossary of Meteorology.* 2nd edition, World Meteorological, 855 pp, also available at http://amsglossary.allenpress.com/glossary

Andrews, D.G., J. R. Holton, and C. B. Leovy, 1987: *Middle atmosphere dynamics*, Academic Press, San Diego, 489 pp.

Bosart, L., W. Bracken, and A. Seimon, 1998: A study of cyclone mesoscale structure with emphasis on a large-amplitude inertia-gravity waves. *Mon. Wea. Rev.*, **126**, 1497–1527.

Bühler, O., M. E. McIntyre, and J. F. Scinocca, 1999: On shear generated gravity waves that reach the mesosphere, part I, Wave generation. *J. Atmos. Sci.*, **56**, 3749–3763.

Bühler, O., and M. E. McIntyre, 2005: Wave capture and wave-vortex duality. *J. Fluid Mech.*, **534**, 67-95.

Blumen, W., 1972: Geostrophic adjustment. *Rev. Geophys.*, **10**, 485–528.

Cahn, A., 1945: An investigation of the free oscillations of a simple current system. *Monthly Weather Review*, **119**, 1929–1952.

Charney, J. G., 1952: The use of primitive equations of motion in numerical prediction. *Tellus*, **7**, 22–26.

Chen, Q.-S., and Y.-H. Kuo, 1992: A harmonic-sine series expansion and its application to the partitioning and reconstruction problem in a limited area. *Mon. Wea. Rev.,* **120,** 91–112.

Davis, C. A., and K. A. Emanuel, 1991: Potential vorticity diagnosis of cyclogenesis. *Mon. Wea. Rev.*, **119**, 1929–1952.

Doyle, J., M. A. Shapiro, Q. Jiang and D. Bartells, 2005: Large-amplitude mountain wave breaking over Greenland. *J. Atmos. Sci*., **62**, 3106-3126.

Dudhia, J., 1993: A nonhydrostatic version of the Penn State−NCAR mesoscale models: validation tests and simulation of an Atlantic cyclone and cold front. *Mon. Wea. Rev.*, **121**, 1493-1513.

Dunkerton, T. J., and N. Butchart, 1984: Propagation and selective transmission of inertial gravity waves in sudden warming. *J. Atmos. Sci.*, **41**, 1443-1460

Durran, D. R., 1999: *Numerical Methods for Wave Equations in Geophysical Fluid Dynamics*. Springer-Verlag, New York, 465 pp.

Eckermann, S. D., and C. J. Marks, 1997: GROGRAT: a new model of the global propagation and dissipation of atmospheric gravity waves. *Adv. Space Res.,* **20**, 1253–1256.

Epifanio, C. C.**,** and R. Rotunno, 2005: The dynamics of orographic wake formation in flows with upstream blocking. *J. Atmos. Sci.*, **62**, 3127--3150.

Ford, R., 1994: Gravity wave radiation from vortex trains in rotating shallow water. *J. Fluid Mech.,* **281**: 81-118

Ford, R., M. E. McIntyre, and W. A. Norton, 2000: Balance and the slow quasimanifold: some explicit results. *J. Atmos. Sci*., **57**, 1236–1254.

Fovell, R., D. Durran, and J. R. Holton, 1992, Numerical simulations of convectively generated stratospheric gravity waves. *J. Atmos. Sci.*, **49**, 1427–1442.

Fritts, D. C., 1984, Gravity wave saturation in the middle atmosphere: a review of theory and observations. *Rev. Geophys.*, **22**, 275–308.

Fritts, D. C., and M. J. Alexander, 2003: Gravity wave dynamics and effects in the middle atmosphere. *Rev. Geophys.*, **41**, 1003-1063.

Fritts, D. C., and Z. Luo, 1992: Gravity wave excitation by geostrophic adjustment of the jet stream. Part I: Two-dimensional forcing. *J. Atmos. Sci.*, **49**, 681-697.

Gill, A. E., 1982: *Atmosphere–Ocean Dynamics*. Academic Press, New York, 662 pp.

Gossard, E. E., and W. H. Hooke, 1974: *Waves in the Atmosphere*. Elsevier, Amsterdam, 456 pp.

Griffiths, M., and R. J. Reeder, 1996: Stratospheric inertia-gravity waves generated in a numerical model of frontogenesis. Part I: Model solutions. *Quart. J. Roy. Meteor. Soc.*, **122**, 1153-1174.

Guest, F. M., M. J. Reeder, C. J. Marks, and D. J. Karoly, 2000: Inertia gravity waves observed in the lower stratosphere over Macquarie Island. *J. Atmos. Sci.*, **57**, 737–752.

Grell, G. A., J. Dudhia, and D. R. Stauffer, 1995: A description of the fifth-generation Penn State/NCAR Mesoscale Model (MM5). *NCAR Technical Note*, NCAR/TN-398+STR, 117 pp.

Hines, C. O., 1960: Internal atmospheric gravity waves at ionospheric heights. *Can. J. Phys.*, **38**, 1441–1481.

Holton, J., 2004: *An Introduction to Dynamic Meteorology.* Academics Press, 4th edition, San Diego, 535 pp.

Holton, J. R., P. H. Haynes, M. E. McIntyre, A. R. Douglass, R. B. Road, and L. Pfister, 1995: Stratosphere–troposphere exchange. *Rev. Geophys.,* **33**, 403–439.

Inverarity, G. W., and G. J. Shutts, 2000: A general, linearized vertical structure equation for the vertical velocity: Properties, scalings and special cases. *Quart. J. Roy. Meteor. Soc.* **126**: 2709-2724

Jones, W. L., 1967: Propagation of internal gravity waves in fluids with shear flow and rotation. *J. Fluid Mech.,* **30,** 439-448.

Kaplan, M. L., and D. A. Paine, 1977: The observed divergence of the horizontal velocity field and pressure gradient force at the mesoscale. Its implications for the parameterization of three-dimensional momentum transport in synoptic-scale numerical models. *Beitr. Phys. Atmos.,* **50,** 321–330.

Kim Y.-J., S. D. Eckermann, and H.-Y. Chun, 2003: An overview of the past, present and future of gravity-wave drag parameterization for numerical climate and weather prediction models. *Atmos.– Ocean*, **41**, 65–98.

Klemp, J. B., and R. B. Wilhelmson, 1978: The simulation of three-dimensional convective storm dynamics. *J. Atmos. Sci.*, **35**, 1070-1096.

Koch, S. E., and P. B. Dorian, 1988: A mesoscale gravity wave event observed over CCOPE. Part 3: Wave environment and probable source mechanisms. *Mon. Wea. Rev.*, **116**, 2570–2592.

Koch, S. E., B. D. Jamison, C. Lu, T. L. Smith, E. I. Tollerud, C. Girz, N. Wang, T. P. Lane, M. A. Shapiro, D. D. Parrish, and O. R. Cooper, 2005: Turbulence and gravity waves within an upper-level front. *J. Atmos. Sci.*, **62**, 3885–3908.

Koch, S. E., and C. O'Handley, 1997: Operational forecasting and detection of mesoscale gravity waves. *Wea. Forecasting,* **12,** 253–281.

Koch, S. E., F. Zhang, M. L. Kaplan, Y.-L. Lin, R. Weglarz, and M. Trexler, 2001: Numerical simulation of a gravity wave event observed during CCOPE. Part 3: Mountain-plain solenoids in the generation of the second wave episode. *Mon. Wea. Rev.*, **129**, 909-932.

Koppel, L. L, L. F. Bosart, and D. Keyser, 2000: A 25-yr climatology of large-amplitude hourly surface pressure changes over the conterminous United States. *Mon. Wea. Rev.*: **128**, 51–68.

Kunze, E., 1985: Near-inertial wave propagation in geostrophic shear. *J. Phys. Oceanogr.*, **15**, 544–565.

Lane, T. P., J. D. Doyle, R. Plougonven, M. A. Shapiro, and R. D. Sharman, 2004: Observations and numerical simulations of inertia gravity waves and shearing instabilities in the vicinity of a jet stream. *J. Atmos. Sci.,* **61**, 2692-2706.

Lane, T.P., and T.L. Clark, 2002: Gravity waves generated by the dry convective boundary layer: two-dimensional scale selection and boundary layer feedback. *Quart. J. Roy. Meteor. Soc.*, **128**, 1543-1570.

Leblond, P.H., and L. A. Mysak, 1978: *Waves in the Ocean*. Elsevier, New York, 602 pp.

Lighthill, M. J., 1952: On sound generated aerodynamically. I. General theory. *Proc. Roy. Soc. London,* **211A,** 564–587.

Lighthill, M. J., 1978: *Waves in Fluids*. Cambridge University Press, Cambridge, 496 pp.

Lin, Y., and F. Zhang, 2008: Tracing mesoscale gravity waves in baroclinic jet-front systems. *J. Atmos. Sci.*, **65**, 2402-2415.

Lin, Y.-L., 1994: Airflow over mesoscale heat source. Part I: Responses in a uniform flow. *Taiwan Proc. Natl. Sci. Counc. ROC(A),* **18**, 1-32.

Lindzen, R. S., 1981: Turbulence and stress owing to gravity wave and tidal breakdown. *J. Geophys. Res.*, **86**, 9707–9714.

Luo, Z., and D. C. Fritts, 1993: Gravity-wave excitation by geostrophic adjustment of the jet stream. Part II: three-dimensional forcing. *J. Atmos. Sci.,* **50**, 104–115

Lynch, P., 1989: Partitioning the wind in a limited domain. *Mon. Wea. Rev.*, **117**, 1492–1500.

Lynch, P., 2008: The ENIAC forecasts: a re-creation. *Bull. Amer. Meteor. Soc.*, **89**, 45–55.

Marks, C. J., and S. D. Eckermann, 1995: A three-dimensional nonhydrostatic ray-tracing model for gravity waves: Formulation and preliminary results for the middle atmosphere. *J. Atmos. Sci.,* **52,** 1959–1984.

McIntyre, M. E., and W. A. Norton, 1990: Dissipative wave-mean interactions and the transport of vorticity or potential vorticity. *J. Fluid Mech.,* **212,** 403–435.

McIntyre, M. E., and W.A. Norton, 2000: Potential vorticity inversion on a hemisphere. *J. Atmos. Sci.*, **57**, 1214–1235.

Nappo, C. J., 2002: *An Introduction to Atmospheric Gravity Waves.* Academic Press, Boston, 279 pp.

Ollers, M. C., L. P. Kamp, F. Lott, P. Van Velthoven, H.M. Kelder, and F.W. Sluijter, 2003: Propagation properties of inertia gravity waves through a barotropic shear layer and application to the Antarctic polar vortex. *Quart. J. Roy. Meteor. Soc.***, 129**, 2495-2511.

O'Sullivan, D., and T. J. Dunkerton, 1995: Generation of inertia-gravity waves in a simulated life cycle of baroclinic instability. *J. Atmos. Sci.*, **52**, 3695–3716.

Pallàs-Sanz, E., and A. Viúdez, 2008: Spontaneous generation of inertia-gravity waves during the merging of two baroclinic anticyclones. *J. Phys. Oceanogr.*, **38**, 213-234.

Pandya, R. E., and M. J. Alexander, 1999: Linear stratospheric gravity waves above convective thermal forcing. *J. Atmos. Sci.*, **56**, 2434-2446.

Pfister, L., K. R. Chan, T. P. Bui, S. Bowen, M. Legg, B. Gary, K. Kelly, M. Proffitt, and W. Starr, 1993: Gravity waves generated by a tropical cyclone during the STEP tropical field program: a case study. *J. Geophys. Res.*, **98**, 8611–8638.

Plougonven, R., D. J. Muraki, and C. Snyder, 2005: A baroclinic instability that couples balanced motions and gravity waves. *J. Atmos. Sci.*, **62**, 1545–1559.

Plougonven, R., and C. Snyder, 2005: Gravity waves excited by jets: propagation versus generation. *Geophys. Res. Lett.*, **32**, L18802.

Plougonven, R., and C. Snyder, 2007: Inertia-gravity waves spontaneously generated by jets and fronts. Part I: Different baroclinic life cycles. *J. Atmos. Sci.* **64**, 2502-2520.

Plougonven, R., and F. Zhang, 2007: On the forcing of inertia-gravity waves by synoptic-scale flows. *J. Atmos. Sci.*, **64**, 1737-1742.

Plougonven, R., and H. Teitelbaum, 2003: Comparison of a large-scale inertia-gravity wave as seen in the ECMWF analyses and from radiosondes. *Geophys. Res. Lett.*, **30**, 1954-1957.

Powers, J., and R. Reed, 1993: Numerical model simulations of the large-amplitude mesoscale gravity-wave event of 15 December 1987 in the central unite states. *Mon. Wea. Rev.*, **121**, 2285–2308.

Ramamurthy, M. K., R. M. Rauber, B. P. Collins, and N. K. Malhotra, 1993**:** A comparative study of large-amplitude gravity-wave events. *Mon. Wea. Rev.,* **121**, 2951–2974.

Raymond, D. J., 1992: Nonlinear balance and potential-vorticity thinking at large Rossby number. *Quart. J. Roy. Meteor. Soc.*, **118**, 987–1015.

Reeder, M. J., and M. Griffiths, 1996: Stratospheric inertia-gravity waves generated in a numerical model of frontogenesis. II: Wave sources, generation mechanisms and momentum fluxes. *Quart. J. Roy. Meteor. Soc.*, **122**, 1175–1195.

Richardson, L. F., 1922: *Weather Prediction by Numerical Process*. Cambridge University Press, Cambridge, 236 pp. Reprinted by Dover Publications, New York, 1965.

Rossby, C., 1937: On the mutual adjustment of pressure and velocity distributions in certain simple current systems. *Journal of Marine Research*, **1**, 15–28.

Rotunno, R., D. J. Muraki, and C. Snyder, 2000: Unstable baroclinic waves beyond quasigeostrophic theory. *J. Atmos. Sci.*, **57**, 3285–3295

Sato, K., 1994: A statistical study of the structure, saturation and sources of inertio-gravity waves in the lower stratosphere observed with the MU radar. *J. Atmos. Terr. Phys.,* **56**, 755–774.

Schneider, R. S., 1990: Large-amplitude mesoscale wave disturbances within the intense midwest extratropical cyclone of 15 December 1987. *Wea. Forecasting,* **5**, 533–558.

Shapiro, M. A., and D. Keyser, 1990: Fronts, jet streams, and the tropopause. *Extratropical Cyclones: The Erik Palmen Memorial Volume,* C. W. Newton and E. O. Holopainen, Eds., Amer. Meteor. Soc., 167–191.

Simmons, A. J., and B. J. Hoskins, 1978: The life cycles of some nonlinear baroclinic waves. *J. Atmos. Sci.*, **35**, 414–432.

Skamarock, W. C., and J. B. Klemp, 1992: The stability of time-split numerical methods for the hydrostatic and the nonhydrostatic elastic equations. *Mon. Wea. Rev*., **120**, 2109-2127.

Smith, R. B., 2004, Mountain meteorology and regional climates. Chapter 9 in *Atmospheric Turbulence and Mesoscale Meteorology*, Ed. E. Fedorovich, R. Rotunno, B. Stevens, Cambridge University Press, Cambridge, 193-222.

Snyder, C., D. J. Muraki, R. Plougonven, and F. Zhang, 2007: Inertia-gravity waves generated within a dipole vortex. *J. Atmos. Sci.*, **64**, 4417-4431.

Snyder, C., W. Skamarock, and R. Rotunno, 1993: Frontal dynamics near and following frontal collapse. *J. Atmos. Sci.*, **50**, 3194-3211.

Staquet, C. and J. Sommeria, 2002: Internal gravity waves: From Instabilities to Turbulence, *Annual Review of Fluid Mechanics*, **34**, 559-593.

Smith, R.B., 2004, Mountain meteorology and regional climates. Chapter 9 in *Atmospheric Turbulence and Mesoscale Meteorology*, Ed. E. Fedorovich, R. Rotunno, B. Stevens, Cambridge University Press, 193-222.

Yamanaka, M. D., and H. Tanaka, 1984: Propagation and breakdown of internal inertia-gravity waves near critical levels in the middle atmosphere. *J. Meteor. Soc. Japan,* **62,** 1-16.

Thorncroft, C. D., B. J. Hoskins, and M. E. McIntyre, 1993: Two paradigms of baroclinic-wave life-cycle behavior. *Quart. J. Roy. Meteor. Soc.,* **119,** 17–55.

Uccellini, L. W., and S. E. Koch, 1987: The synoptic setting and possible source mechanisms for mesoscale gravity wave events. *Mon. Wea. Rev.*, **115**, 721–729.

van Tuyl, A. H., and J. A. Young, 1982: Numerical simulation of nonlinear jet streak adjustment. *Mon. Wea. Rev.,* **110,** 2038–2054.

Vanneste, J., 1995: The instability of internal gravity waves to localized disturbances. *Ann. Geophys.*, **13**, 196–210.

Vanneste, J., and I. Yavneh, 2004: Exponentially small inertia–gravity waves and the breakdown of quasigeostrophic balance. *J. Atmos. Sci.*, **61**, 211–223.

Viúdez, A., 2007: The origin of the stationary frontal wave packet spontaneously generated in rotating stratified vortex dipoles. *J. Fluid Mech.*, **593**, 359-383.

Viúdez, A., 2008: The stationary frontal wave packet spontaneously generated in mesoscale dipoles. *J. Phys. Oceanogr*., **38**, 243-256.

Wang, S. and F. Zhang, 2007: Sensitivity of mesoscale gravity waves to the baroclinicity of jet-front systems. *Mon. Wea. Rev.*, **135**, 670-688.

Wicker, L. J., and W. C. Skamarock, 1998: A time-splitting scheme for the elastic equations incorporating second-order Runge-Kutta time differencing. *Mon. Wea. Rev.*, **126**, 1992-1999.

Wicker, L. J., and W. C. Skamarock, 2002: Time-splitting methods for elastic models using forward time schemes. *Mon. Wea. Rev.,* **130**, 2088-2097.

Wu, D. L., and F. Zhang, 2004: A study of mesoscale gravity waves over North Atlantic with satellite observations and a mesoscale model. *J. Geophys. Res*., **109**, D22104., doi: 10.1029/2004JD005090.

Zhang, F., 2004: Generation of mesoscale gravity waves in the upper-tropospheric jet front systems. *J. Atmos. Sci.*, **61**, 440–457.

Zhang, F., and S. E. Koch, 2000: Numerical simulation of a gravity wave event observed during CCOPE. Part 2: Wave generation by an orographic density current. *Mon. Wea. Rev.*, **128**, 2777-2796.

Zhang, F., S. E. Koch, C. A. Davis, and M. L. Kaplan, 2000: A survey of unbalanced flow diagnostics and their application. *Adv. Atmos. Sci.*, **17**, 165-183.

Zhang, F., S. E. Koch, C. A. Davis, and M. L. Kaplan, 2001: Wavelet analysis and the governing dynamics of a large-amplitude gravity wave event along the east coast of the United States. *Quart. J. Roy. Meteor. Soc.*, **127**, 2209-2245.

Zhang, F., S. E. Koch, and M. L. Kaplan, 2003: Numerical simulations of a large-amplitude gravity wave event. *Meteorology and Atmospheric Physics*, **84**, 199-216.

Zhang, F., S. Wang, and R. Plougonven, 2004: Uncertainties in using the hodograph method to retrieve gravity wave characteristics from individual soundings. *Geophys. Res. Lett.*, **31**, L11110, doi:10.1029/2004GL019841.

Zülicke, C., and D. Peters, 2006: Simulation of inertia-gravity waves in a poleward breaking Rossby wave. *J. Atmos. Sci.* **63,** 3253 – 3276.

APPENDIX

(I) The reference state

Assuming the basic state is horizontally homogeneous with uniform stratification $N^2 = \frac{g}{\theta}\frac{\partial \theta}{\partial z} = 2\times 10^{-4} s^{-2}$, we obtain the vertical distribution of potential temperature as function of height, $\theta = \theta_o \exp(N^2 z/g)$, and pressure by applying hydrostatic balance, $\left(\frac{p}{p_0}\right)^{\kappa} = \frac{g^2 \kappa}{R\theta_0 N^2}\left[\exp\left(-\frac{N^2}{g}z\right) - 1\right] + 1$. At the surface, we apply the boundary condition with pressure $p_0 = 1000 hPa$ and $\theta_0 = 300K$ when z = 0. The reference EPV in a resting atmosphere takes the form as a function of z only: $Q(z) = -gf\frac{\partial \theta}{\partial p} = -\frac{fN^2}{g}\cdot\frac{\theta}{\rho}$, where ρ is density obtained from the equation of state $\rho = \frac{p}{RT} = \frac{p^{1-\kappa}p_0^{\kappa}}{R\theta}$, p, θ, and f, the Coriolis parameter ($1\times 10^{-4} s^{-1}$).

(II) EPV perturbation for the mid-level and surface vortex dipoles

Perturbation EPV introduced in the middle of the coarse domain is defined as the truncated cosine squared function with certain radius of influence R_0:

$$Q' = 0.75 \times Q(z_0) \cdot \left[\cos^2(r_{10} \cdot \pi / 2) - \cos^2(r_{20} \cdot \pi / 2) \right],$$

where $r_{10} = \begin{cases} r_1, & if \quad r_1 \le 1 \\ 0 \end{cases}$, $r_1 = \sqrt{(x - x_1)^2 + (y - y_1)^2 + \gamma \cdot \left((z - z_0) \cdot \frac{\Delta x}{\Delta z} \right)^2} \Big/ R_0$,

$$r_{20} = \begin{cases} r_2, & if \quad r_2 \le 1 \\ 0 \end{cases}, \quad r_2 = \sqrt{(x - x_2)^2 + (y - y_2)^2 + \gamma \cdot \left((z - z_0) \cdot \frac{\Delta x}{\Delta z} \right)^2} \Big/ R_0,$$

where the positive [negative] EPV anomaly is centered at (x_1, y_1, z_0) [(x_2, y_2, z_0)],

$x_1 = 60 \cdot \Delta x$, $y_1 = 90 \cdot \Delta y$, $x_2 = 60 \cdot \Delta x$, $y_2 = 70 \cdot \Delta y$, $z_0 = 58 \cdot \Delta z = 11.6 km$. These compact PV anomalies continuously drop to zero at the circle of radius $R_0 = 20 \cdot \Delta x = 1800 km$ at the level of z_0. The vertical penetration of EPV anomalies is controlled by the parameter $\gamma = 0.64$ such that they achieve a maximum depth of 10 km at the center (x_1, y_1) or (x_2, y_2). Perturbed potential temperature is introduced in a similar way with the same cosine squared function:

$$\theta(z = 0) = 25 \cdot \left[\cos^2(r_{10} \cdot \pi / 2) - \cos^2(r_{20} \cdot \pi / 2) \right].$$

(III) Scaling of Ertel potential vorticity

Ignoring the horizontal wind shear, Ertel PV can be written as

$$Q = \frac{g}{\rho\theta_0}\left(f \cdot N^2 + \zeta \cdot N^2 + f \cdot \frac{\partial b}{\partial z} + \zeta \cdot \frac{\partial b}{\partial z} + \zeta_x \cdot \frac{\partial b}{\partial x} + \zeta_y \cdot \frac{\partial b}{\partial y} \right).$$

Introducing horizontal and vertical scales L and H, and wind scale U, relatively vorticity ζ and buoyancy $b = \frac{g}{\theta_0}\frac{\partial \theta'}{\partial z}$ are scaled as $\zeta \sim \frac{U}{L}$, $b \sim \frac{UFL}{H}$. It can be shown that the ratios of last 5 terms to the first term (background PV) are

$$\frac{\zeta \cdot N^2}{f \cdot N^2} \sim Ro\ ,\ \frac{f \cdot \frac{\partial b}{\partial z}}{f \cdot N^2} \sim \frac{Ro}{Bu}\text{, and } \frac{(\zeta \cdot \frac{\partial b}{\partial z}, \zeta_x \cdot \frac{\partial b}{\partial x}, \zeta_y \cdot \frac{\partial b}{\partial y})}{f \cdot N^2} \sim \frac{Ro^2}{Bu}.$$

The linear terms (term 2 and 3) are both scaled as Ro assuming the Burger number $Bu \sim O(1)$. The Rossby number is of the small order $Ro : O(1)$. The last three terms are the next order of corrections Ro^2.

VITA

Name: Shuguang Wang

Address: Department of Atmospheric Sciences, Texas A&M University, College Station, TX 77843-3150

Email Address: wangs@tamu.edu

Education: B.S., Atmospheric Sciences, Nanjing University, 2000
M.S., Atmospheric Sciences, Nanjing University, 2003
M.S., Atmospheric Sciences, Texas A&M University, 2005
Ph.D., Atmospheric Sciences, Texas A&M University, 2008